FRONT END X-RAY BEAM POSITION MONITORS AT THE CANADIAN LIGHT SOURCE

A Thesis Submitted to the College of
Graduate Studies and Research
In Partial Fulfillment of the Requirements
For the Degree of Master of Science
In the Department of Physics and Engineering Physics
University of Saskatchewan
Saskatoon

By

SHELDON SMITH

Keywords: front end, x-ray beam position monitor, synchrotron radiation

PERMISSION TO USE

In presenting this thesis in partial fulfillment of the requirements for a Postgraduate degree from the University of Saskatchewan, I agree that the Libraries of this University may make it freely available for inspection. I further agree that permission for copying of this thesis in any manner, in whole or in part, for scholarly purposes may be granted by the professor or professors who supervised my thesis work or, in their absence, by the Head of the Department or the Dean of the College in which my thesis work was done. It is understood that any copying or publication or use of this thesis or parts thereof for financial gain shall not be allowed without my written permission. It is also understood that due recognition shall be given to me and to the University of Saskatchewan in any scholarly use which may be made of any material in my thesis.

Requests for permission to copy or to make other use of material in this thesis in whole or part should be addressed to:

Head of the Department of Physics and Engineering Physics

116 Science Place

University of Saskatchewan

Saskatoon, Saskatchewan (S7N 5E2)

ABSTRACT

The development of X-ray Beam Position Monitors (XBPM) used on the Canadian Light Source front ends is described in this thesis, from the design concepts to the practical implementation and commissioning. Surveyed into position to provide a fiducialized point of origin for incoming synchrotron radiation, the primary purpose of the XBPM is to provide a measure of synchrotron beam motion. Currently XBPMs have been installed on three beamlines at the Canadian Light Source, a 2.9 GeV third generation synchrotron radiation source. Two of the XBPMs are comprised of chemical vapour deposition synthetic diamond blades coated with gold and installed on insertion device beamlines, while the third makes use of molybdenum blades for a dipole beamline. By incrementally scanning the blades of the XBPM through the synchrotron beam it is possible to determine the monitors' spatial resolution to beam motion. For the commissioned XBPM a typical spatial resolution of +/- 1 micron of beam motion was achieved; and the thermal power loading capacity has been tested to the 2/5 of maximum value. An independent white beam profiler, comprised of a converter crystal and image acquisition software, was constructed to corroborate the functionality of the XBPM.

ACKNOWLEDGMENTS

I would like to thank my supervisor, De-Tong Jiang, and my co-supervisor, Jack Bergstrom, for all the time, effort and help they have provided me in the course of this project.

To all the guys in the Engineering group who provided a host of invaluable services, without which this project could not have been accomplished, I offer a very heartfelt thank you.

A special thanks to Elder Matias, Tony Wilson, Mike McKibben and Dr. Johannes Vogt for their expertise in controls and electronics and their seemingly endless supply of patience.

I would also like to thank Lavina Carter and Jordan Hamel for helping me navigate through the sometimes confusing and frustrating options of MS Word. I could not have written this thesis without their help.

And finally, I would like to thank Mark de Jong and Jeffery Cutler for extending an invitation into the exciting world of synchrotron research. Thank you!

Dedicated to my family and friends who have encouraged
and supported me throughout the years.
Mom, Dad, Molly, Dave, Jaime and Nicole--Thank you.

Table of Contents

List of Tables

List of figures

List of Abbreviations

ADC	Analog to Digital Converter
ALS	Advanced Light Source
APS	Advanced Photon Source
BM	Bending Magnet
BPM	Beam Position Monitor
CCD	Charge-Coupled Device
CHESS	Cornell High Energy Synchrotron Source
CLS	Canadian Light Source
CMCF	Canadian Macromolecular Crystallography Facility
CVD	Chemical Vapour Deposition
FE	Front End
FM	Fixed Mask
FOV	Field of View
FWHM	Full Width Half Maximum
HXMA	Hard X-ray Micro-Analysis
ID	Insertion Device
NPLC	Number of Power Line Cycles
NSLS	National Synchrotron Light Source
OFHC	Oxygen Free High Conductivity
PMAG	Primary Magnification
SR	Synchrotron Radiation
TEY	Total Electron Yield
TRM	Transition Radiation Monitor
VUV	Vacuum Ultra-Violet
XBPM	X-ray Beam Position Monitor
XSR	X-ray Synchrotron Radiation
YAG	Yttrium Aluminium Garnet

1 X-RAY BEAM POSITION MONITORING

Much of modern physical science is based on the understanding of matter at the atomic or molecular level of detail. Many forms of light (i.e. electromagnetic waves) have been developed as probes for acquiring the atomic and electronic structural information. Synchrotron radiation is an example of such a structural tool. Synchrotron radiation (SR) is produced by accelerating charged particles (e.g. electron or proton) in particle accelerators and the SR facilities are capable of generating radiation from the infrared, through the visible and into the X-ray portions of the spectrum. Compared to conventional light sources, SR is characterized by the properties of extremely high intensity and a high level of collimation at the sample target (i.e. high brilliance) which enables many experimental applications of light-matter interactions that would otherwise not be feasible. Once generated the light is conditioned by a beamline's particular optics to the desired characteristics necessary for experiments involving the interaction of radiation with matter. But prior to any experimental procedure it is imperative to know the position and direction of the incoming light beam. Without the knowledge of where the beam is positioned it becomes difficult to provide a consistent set of operating conditions for any experimental endeavour. Therefore facilities throughout the world employ a variety of beam position monitors, for either the electron or synchrotron radiation beams, to dynamically measure the beam position and direction.

In this thesis three X-ray Beam Position Monitors (XBPM) situated on three different beamlines at the Canadian Light Source (CLS) are studied. Each of the XBPMs will be used to determine the synchrotron beam position on X-ray beamlines (c.a. hundreds of eV to tens of keV). Of principle importance is the spatial resolution of the XBPM, i.e. what minimum change in beam motion is the monitor able to detect? Secondary to sensitivity is the conveyance of useful beam position information to the experimental end user.

The following sections will outline the basic types of monitors used to determine synchrotron beam position. A history of XBPMs will be presented outlining the challenges of beam position detection at synchrotron facilities and the ways researchers have tried to overcome the obstacles. Finally the XBPMs used at the CLS and the environment the monitors will encounter are described.

1.1 Introduction to Beam Position Monitors

X-ray beam position monitors (XBPM) are used to measure the centroid of the synchrotron radiation (SR) beam that is of interest to beamline users, i.e. the 1st moment of the Gaussian that approximates the central cone of the beamline source, with high precision. Ref. (1) provides an excellent introduction to the many types of beam position monitors (BPM) found within synchrotron facilities and discusses the advantages, disadvantages, and physical considerations undertaking in choosing a monitoring system. Briefly, the types of BPMs are: fluorescent screens, transition radiation monitors (TRM), button or strip-line monitors, flying wire, split plate ionization chambers, filter/window combinations, and blade type monitors. In principle the SR beam position could be deduced from the knowledge of the position and direction of the moving electron beam. Therefore we start our discussion from the usual storage ring e-beam position monitors.

Fluorescent screens or transition radiation monitors (TRM) can be used within the linear accelerator to determine the position of the electron beam as it is initially created and accelerated. A TRM makes use of Cerenkov radiation as the relativistic electrons pass through a material so that the emitted light can be used to determine the electron beam position.

Within the booster and synchrotron rings can be found button monitors or strip-line monitors. These two devices work from the same principle: image currents formed on the vacuum chamber walls as the electron beam passes are measured by either the button or strip-line monitor and used to infer the beam position.

Flying wire devices, in which a wire is scanned through the electron beam, have also been used to determine the electron beam position or even the SR beam position. In either case a wire is scanned through the beam and either the current or visible fluorescence is measured and used to determine the beam center.

As mentioned above, the other means to determine the centroid of the SR beam are: wire scanner [2-5], split ionization chamber [6, 7], and a filter/window BPM combination [8-11]. In the following paragraphs each of the possible detection means will be discussed.

In the wire scanner, as shown in figure 1.1, a metal wire, usually tungsten, is scanned through the beam so that a photocurrent is generated. Unfortunately the intensity distribution of the photon beam is disturbed during the scan and would have to be coordinated to times when the user controlled photon shutter is closed; otherwise some part of the radiation fan will experience attenuation in intensity [1] which is propagated down the remainder of the beamline. Another situation is when the wires are held stationary and is limited to portions of the beam not used by the experimental end station. However, any wire type monitors will experience difficulty in a high SR heat load environment, such as that generated by an insertion device (ID) beamline front end, due to the total power and power density intercepted, which will be discussed below.

Split ionization chambers, shown in figure 1.2, are primarily used in a gas filled environment. Synchrotron light passes through the center of the chamber and partially ionizes the gas. With a potential difference across the plates the ions and electrons travel in opposite directions to be collected so that the difference between the measured current of the two plates can be used to infer the beam position. A number of factors must be considered when using this type of detector: what type of gas to use, when does saturation occur, what is the transit time of the particles, should a solid or split plate be used, what is the probability of recombination. Some of the factors if not considered carefully will lead to position measurements that are sensitive to beam intensity [1]. But this type of detector is not acceptable in the CLS Front End (FE) near the storage ring which is an ultrahigh vacuum environment.

The filter/window combination, figure 1.3, while accurately determining the centroid and passing only those photons for which the filter/window is transparent, does so at the expense of intercepting the full SR beam. When the SR beam passes through the filter/window material, usually diamond, free carriers are generated within the

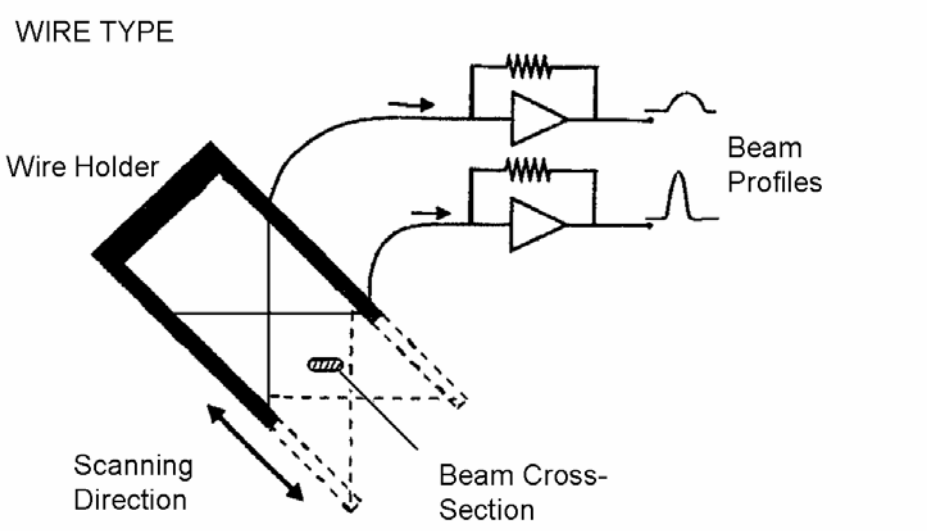

Figure 1.1 Representation of a wire type beam position monitor. The Image depicts a schematic of a wire scanner used by Fajardo and Ferrer, redrawn from Ref. 2.

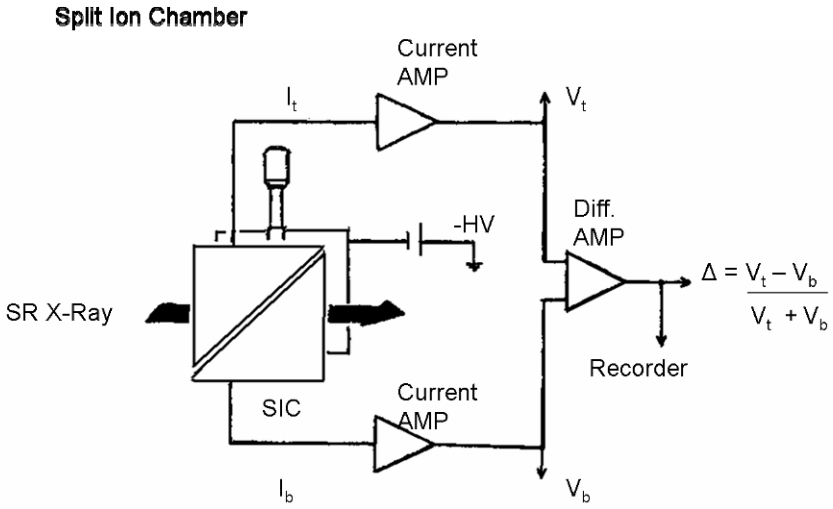

Figure 1.2 Schematic of a split anode ion chamber. Shown above is the ion chamber used by Koyama et al., redrawn from Ref. 6. The difference over sum ratio is proportional to the beam displacement from the center of the chamber.

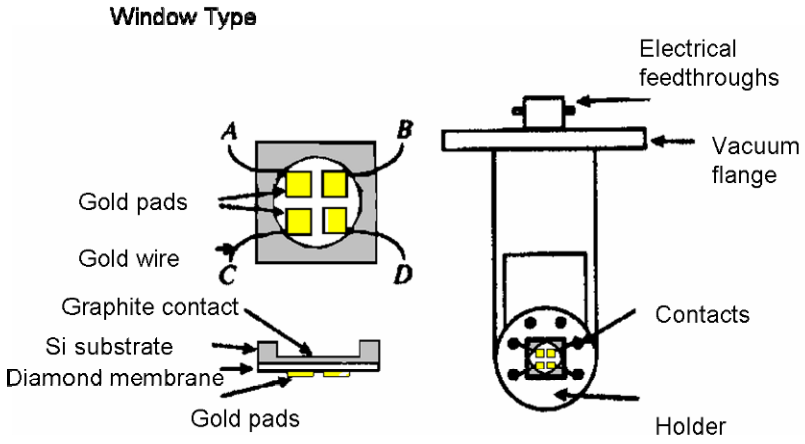

Figure 1.3 Example of a filter/window BPM. Above is a schematic of filter/ window BPM used by Bergonzo et al., redrawn from Ref. 8. SR passes through the center of the BPM which generates free electron-hole pairs within the diamond. The photoconductive current is then detected by the gold pads.

material. An external electric field causes the free carriers to drift resulting in an induced current which is measured to determine position [8-12]. In addition, when the beam size is larger than the electrode separation a weaker signal difference would be acquired resulting in a position resolution that is beam size dependent [8]. Generally this type of monitor is not used within the FE.

Generally what is needed is a XBPM that causes little intensity perturbation downstream of its position [8], is non-destructive to the SR beam and is suitable for continuous use [13], and must withstand high thermal loads and achieve submicron level spatial resolution while maintaining stability [14]. It is worth noting that the above requirements parallel the advent of IDs and the move towards 3rd generation facilities.

By far the best possible means to accurately and precisely measure the SR beam centroid is to terminate the beam. This can be accomplished either by terminating the SR beam on a Cu or Ta block [15, 16], figure 1.4, or by intercepting the beam with a fluorescent screen [17, 18]. For either the block or the screen the visible fluorescence is imaged by photodiodes or a camera which records the changing intensity due to

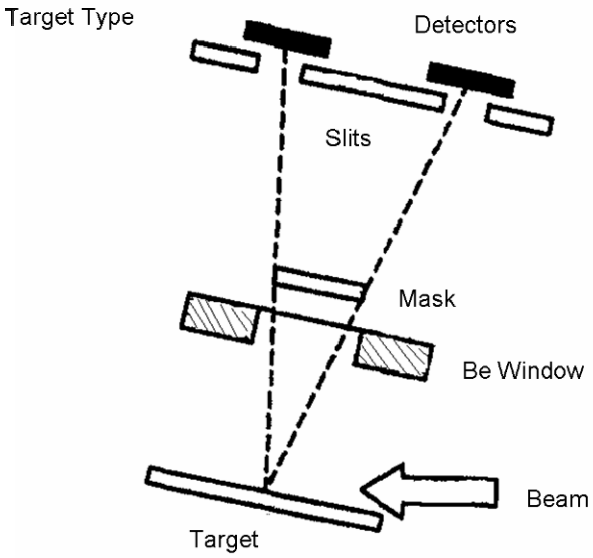

Figure 1.4 Example of a target type beam position monitor. Position monitor schematic showing the copper target used by Cerino et al. for beam monitoring, redrawn from Ref. 15.

motions of the SR beam on the block or screen [1]. While this would provide accurate determination of the 1st moment, the SR beam is temporarily or completely unusable which is generally difficult to implement if the same SR solid angle is to be accessible by the users.

To minimize impact to the experimental community, while meeting the requirements outlined above, "blade type" monitors were developed. The need for this type of monitor is best summarized by Galimberti [19]:

> The latest generation SR sources have severe constraints for the stability of the delivered radiation. The high brightness beamlines using undulator radiation are most sensitive to electron beam oscillations. Therefore, photon beam position monitors for undulator radiation are being built as detectors of beam movements and as references for feedback systems.

Blade type monitors are found not only on undulator beamlines but also on wiggler and Bending Magnet (BM) lines and is the type of monitor that will initially be used on three FEs at the CLS.

1.2 Blade Type X-Ray Beam Position Monitors

In 1986 Mortazavi et al. [20] reported the first instance of a blade type monitor being used on an ID FE. Mortazavi et al. noted that on an undulator line, where the useable SR dimension may only be a few millimetres, a small angular deviation at the source can produce a large movement at the experimental location. The team developed a monitor that could be used to determine the photon beam path and if needed be used as a feedback to steering magnets to correct any beam error.

Monitors were designed for vertical and horizontal motion (figure 1.5) comprised of thin tungsten blades, heat pipes and condensers for cooling, and linear actuators for positioning. According to Mortazavi et al., each blade would project into the fringes of the SR beam (VUV and soft x-ray portion) receiving 3-4% of the peak intensity, and due to photoemission a signal generated on the tungsten blades would determine the beam position, figure 1.6. The team noted that due to low signal levels each blade had to be biased, and that the noise levels were less than 10^{-12} A with a similar signal magnitude for the blade not in the beam [20]. From figure 1.6 it can be seen that the signal is fairly linear over a range of 0.5 mm with a signal current in the sub-nano amperage range. Blade dimensions were chosen so that in a worst case scenario, direct contact with beam core (760 W) intercepting 70 W, the energy could be removed without damage to the blades and still maintain functionality.

In 1989 significant improvements were reported by Johnson and Oversluizen [21]. Instead of heat pipes and individual control for the horizontal and vertical blades a compact copper monolith was developed, figure 1.7. The water cooled copper monolith forms a simple cooling circuit, as opposed to the heat pipes of Mortazavi et al., with the tungsten blades mounted 90^0 apart on the monolith. The blades are electrically isolated from the copper block and each component, blades and monolith could be biased at different voltages or grounded. Johnson and Oversluizen reported currents measured at the blades on the order of 1 μA per 100 mA of stored beam. They performed many experiments to determine which biasing scheme worked best eventually deciding that the monolith biased positive with blades near ground had the most reproducible results. In addition they performed many measurements of the sensitivity of the monitor inferring that the sensitivity is well below 0.1 μm with linearity over 1.7 mm.

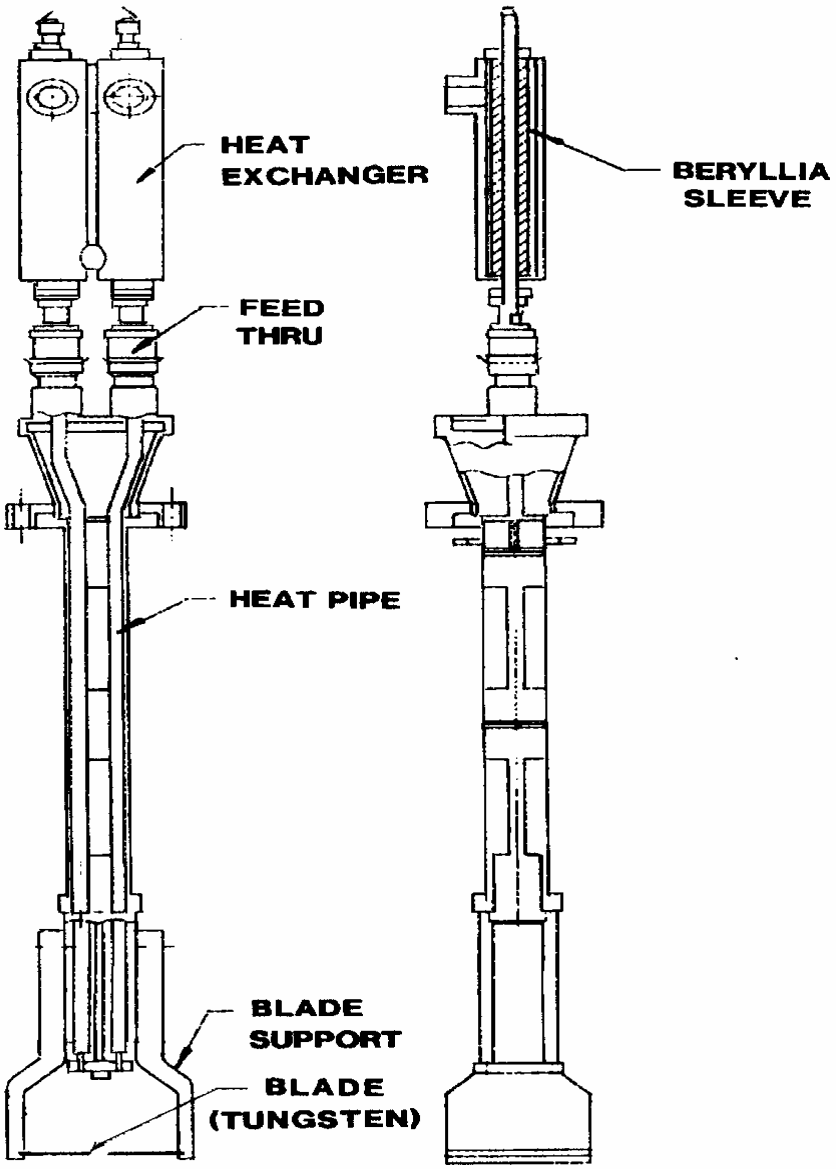

Figure 1.5 General assembly of XBPM monitors developed by Mortazavi et al., Ref 20.

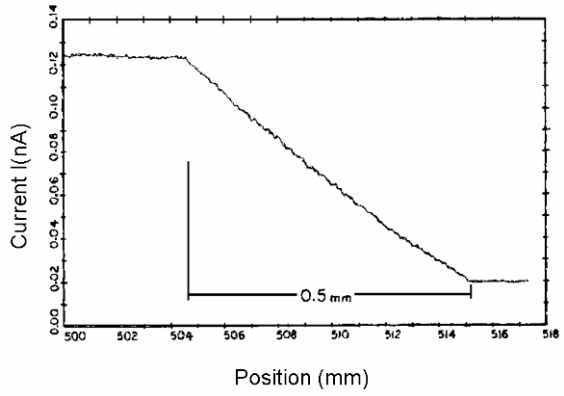

Figure 1.6 Output current for Mortazavi et al., XBPM stepping through the beam, Ref. 20.

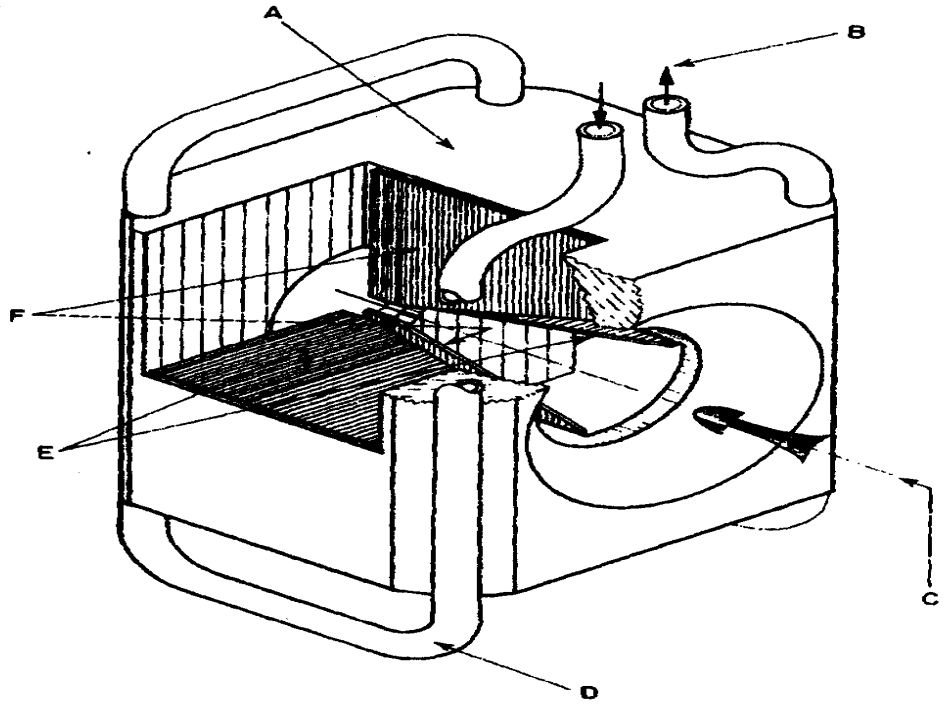

Figure 1.7 Schematic view of Johnson and Oversluizen XBPM showing blades and cooling tubes, Ref. 21. A – copper monolith, B – cooling water flow, C – direction of photon beam, D – cooling water tubes, E – horizontal blades, and F – vertical blades. Ref. 21.

Johnson and Oversluizen identified three variables relevant to BPMs: sensitivity, response transfer function, and long term stability [21]. Sensitivity was easily characterized by stepping the monitor through the beam at pre-determined step sizes and monitoring the signal strength difference between the blade pairs. By repeating this measurement multiple times the monitor sensitivity, 0.1 μm, was determined. The response transfer function (range between max and min current), determined to be 1.7 mm, should be a linear function between the blade current ratio and the monitor position as the monitor is stepped through the beam. To determine the blade current ratio the signal on each blade was amplified so that the ratio of the difference in observed current to the sum of the currents could be recorded which will be addressed further in section 2.4. The last variable to quantify, (dynamic) stability, addresses the dependence of the recorded beam position on machine current [21]. Here the difficulty, identified in Ref. 21, is in separating real beam motion with time from detector drift. Some experiments were suggested to differentiate these effects and it was reported that the beam maximum could be determined within 10 μm when the effect of these uncertainties included [21].

It is from the work of Johnson and Oversluizen that all current blade type monitors are derived. From this work three main branches of blade type monitor can be categorized. The work of Warwick et al. [22, 23] in which the blades are positioned at different angles to avoid the problem of shadowing between different monitors and different biasing schemes to inhibit emission of low energy electrons to increase sensitivity to high energy photons constitutes one branch. Another branch follows the work done by Galimberti et al. [13, 19] where electrostatic lenses and electron energy analyzers are mounted behind the blades so as to increase the sensitivity to the position of the desired photon energy harmonic needed at the experimental location. The last branch follows the work of Shu, currently of the Advanced Photon Source (APS), whose latest incarnation of XBPM will be used at the CLS.

1.2.1 Warwick X-Ray Beam Position Monitor

In 1991 Warwick et al. presented an XBPM for undulators at the ALS that overcame limitations of low K values, where K is a measure of electron beam deflection within the

ID and is proportional to the period and magnetic field strength of an undulator or wiggler. The problem, as presented in Ref. 22, is that as K increases the horizontal width of the photon power distribution increases proportional to K while the total power increases as K^2. Thus the horizontal blades must protrude far enough towards the axis to intercept the beam at low K while withstanding overheating due to large K (Ref. 22). The solution proposed was to place the blades at a 45^0 angle, figure 1.8. The one downside to this arrangement, noted by Warwick et al., is that purely horizontal or vertical motion will appear to have components of the other orthogonal necessitating the compensation of sensitivities in each blade, be it geometric or electronic.

In 1995 Warwick et al. presented the on going tests of position sensitivity of the XBPM as well as presenting the results of an electronic prototype compensation circuit which aids in the position determination as the undulator gap is opened or closed. Using the blade current ratio outlined previously, and noting that the zero of the beam position is arbitrary in that it depends on the detector position [23], Warwick et al. reported a vertical position resolution of 2 μm.

1.2.2 Galimberti X-ray Beam Position Monitor

In 2001 and 2002 Galimberti et al. proposed a novel BPM which is based on energy discrimination in the whole radiation spectrum to preferentially pick up the ID contributions and hence inferring the ID beam position [13]. The BPM is composed of blades from which the photoelectrons are emitted and an electron energy analyzer which is comprised of electrostatic input lenses and hemispherical dispersing elements. With this arrangement the analyzers perform band pass filtering on the electron energies in order to maintain only those electrons with a narrow energy bandwidth centered on the desired undulator harmonic [19]. Beam position sensitivity was reported on the micron level with a reduction in the level of BM contamination to a level of around 0.1%.

While this system of BPM and analyzers provide greater position sensitivity to the desired energy required by the experimental user, with a corresponding reduction in BM contamination, there are a couple of obvious disadvantages. Firstly there is the mechanical system needed to support the electron analyzers and provide motion between the sets of analyzers to maintain symmetry, and secondly there is greater electrical

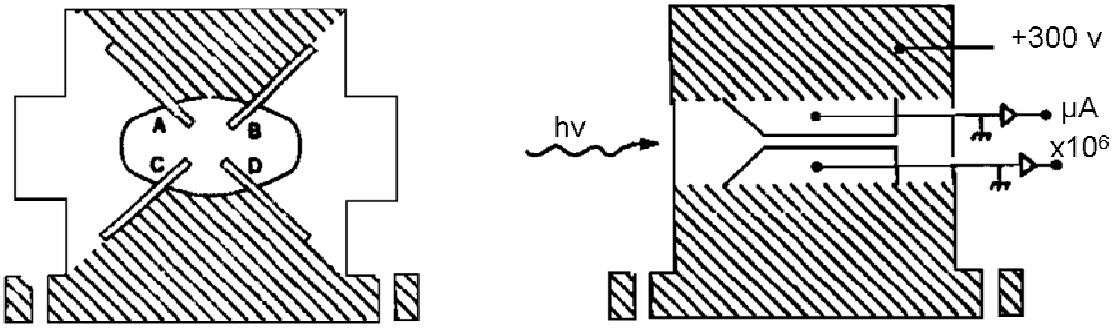

Figure 1.8 Schematic of XBPM designed by Warwick et al showing blades at 45^0, Ref. 22.

infrastructure required to operate this type of XBPM. Lastly, the electron energy analyzers occupy real estate within the FE that at the CLS is not available.

1.2.3 APS X-Ray Beam Position Monitor

In 1992 Shu et al. [14] noted that the previous designs for a blade type monitor would not meet the high power density requirements or spatial constraints that would be encountered at the Advanced Photon Source (APS). In addition to the "standard" requirements of using the VUV and soft X-ray fringes for position determination coupled with a desired sensitivity on the order of 0.5 – 1 μm, the team identified a series of technical conditions to be met. Among the conditions were: 1) choice of photoemission type monitor due to proven performance, 2) Chemical Vapour Deposition (CVD) diamond as blade material owing to superior thermo-physical properties, and 3) use of metal coatings for good photoemission yield [14]. A prototype, figure 1.9, was built to: 1) experimentally prove beam fringes can determine beam center position, 2) test monitor sensitivity, 3) assess BM contamination, and 4) assess if two vertical pairs of blades will provide good horizontal position information [14]. Of the three pairs of blades shown in figure 1.9, two pairs are used for detecting the undulator beam while the remaining pair is

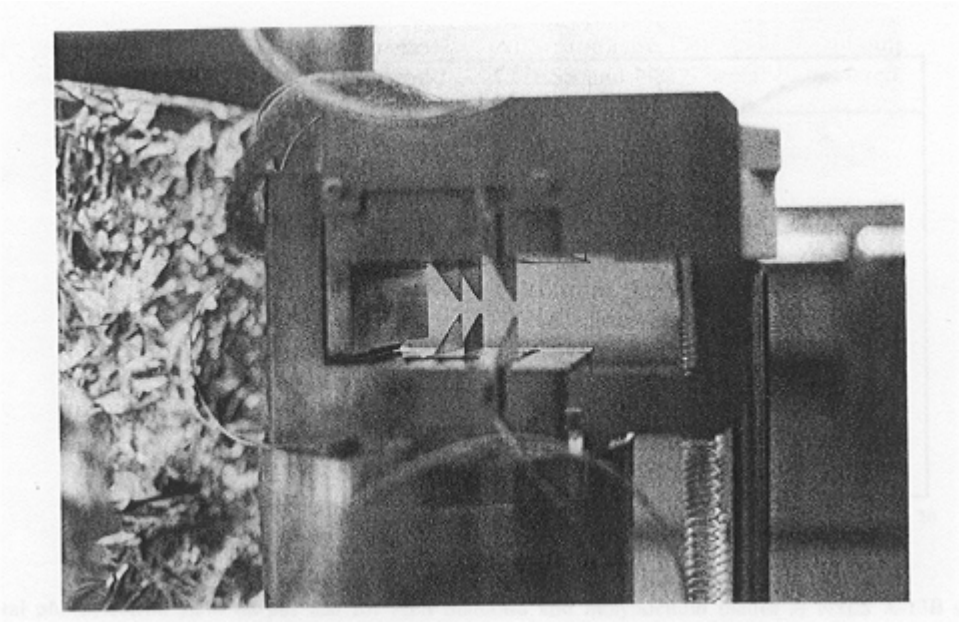

Figure 1.9 Monitor assembly built by Shu et al for diamond blade tests at CHESS, Ref. 14.

for the BM beam. In addition, a CVD diamond blade with 3 μm of tungsten coating was paired against a molybdenum blade to compare performance with tests carried out at NSLS and CHESS. The teams concluded that the CVD diamond blade provided submicron spatial resolution similar to the molybdenum blade, the blades could be kept far from high power density and still provide good spatial resolution, and that the BM contamination is not a serious problem. It was also found that the horizontal sensitivity of the vertical blades was about 3 – 4 times lower than the vertical sensitivity. After 5 weeks of continuous use at CHESS the team subjected the blades to a worst case scenario, direct contact with x-ray core, in which the CVD blade suffered no damage while the molybdenum blade had visible searing on it [14].

In 1994 Shu et al. [24] proposed a new design in which the blades were mounted with blade surface perpendicular to the beam. The blades and coating thickness would be designed so that most of the x-ray beam would be transmitted through. A low Z electrically conductive material would partially or fully coat the CVD diamond. Once again the team tested two samples at NSLS where one blade was fully coated and the other blade was partially coated both with aluminium 0.75 μm thick. The team noted that

depending on the thickness of the base material and of the coating the blades could be made mostly "transmitting" or mostly "transparent" [24]. This work would lead to the development of the filter/window combination that is used at the APS and other facilities.

In 1998 Shu et al. [12], returning to the 'standard' blade type monitor, examined the challenges of XBPMs to contamination from BM sources and sensitivity to ID gap variations. The group developed a smart XBPM system relying on a high-speed digital signal processor and custom made software. The program would iteratively go through a series of steps while searching a database of calibration values and local offsets to determine and correct the beam position. By using the system the team was, in some instances, able to improve the sensitivity of the XBPM from several hundred microns down to several microns. This work was followed up in 1999 and 2002 [25, 26] to further reduce the contamination by BM sources by introduction of a physical chicane within the accelerator lattice, i.e. physically moving the lattice, so that the BM radiation no longer had a direct line of sight with the ID beamlines.

In continuing with improvements to blade type monitors, Shu's current generation of XBPM is a compact design capable of being attached to a Fixed Mask (FM) instead of occupying a separate position in the FE. This current design which will be used at the CLS is described below.

1.3 X-Ray Beam Position Monitors at the Canadian Light Source

Two different styles of XBPM will initially be used at the CLS, figure 1.10. A two vertical blade system will be used in the FE of the X-ray Synchrotron Radiation (XSR), figure 1.11 and the Hard X-ray Micro-Analysis (HXMA) beamlines, figure 1.12. Four vertical blades will be used in the FE of the Canadian Macromolecular Crystallography Facility (CMCF) beamline, figure 1.13. The XBPM units for the XAFS and CMCF lines are attached to fixed masks (FM) while the monitor in the XSR line is housed within its own vacuum chamber.

The blades are mounted parallel to the beam with the curved edge facing the SR beam, i.e. towards the storage ring. The tapered design is used to reduce the heat load (power density) on the blades [20, 23, 24, 26-28]. Power density loads will be discussed below.

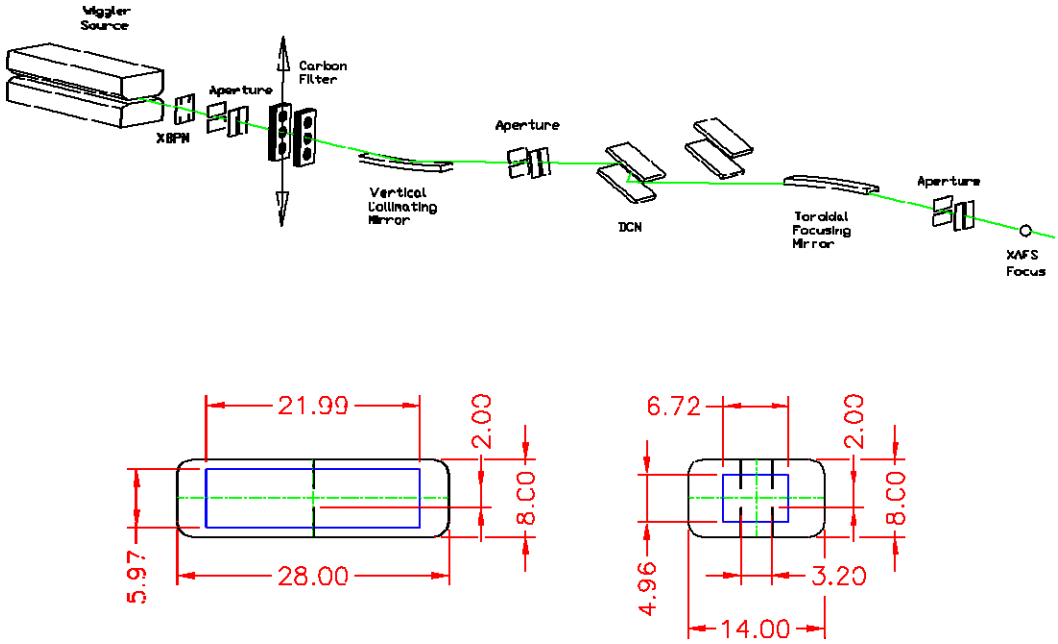

Figure 1.10 Top image indicates placement of XBPM within the beamline (06ID), after the ID or bend magnet and before the adjustable aperture. Bottom image schematic of the XBPM types used at the CLS. The two blade systems are used on the HXMA (left) and XSR (not shown) beamlines while the four blade unit is installed in the CMCF beamline (right). The XBPM aperture, black, is larger than the mask aperture, blue, to avoid interception by synchrotron radiation. Dimensions are in mm.

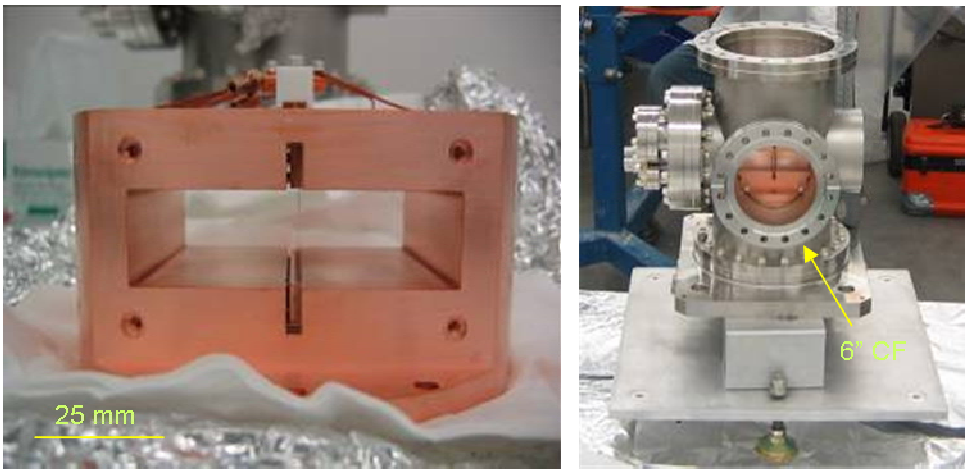

Figure 1.11 The bending magnet XBPM, left, installed in the XSR front end. Vacuum chamber, right, housing the XBPM which is mounted on water filled copper reservoir.

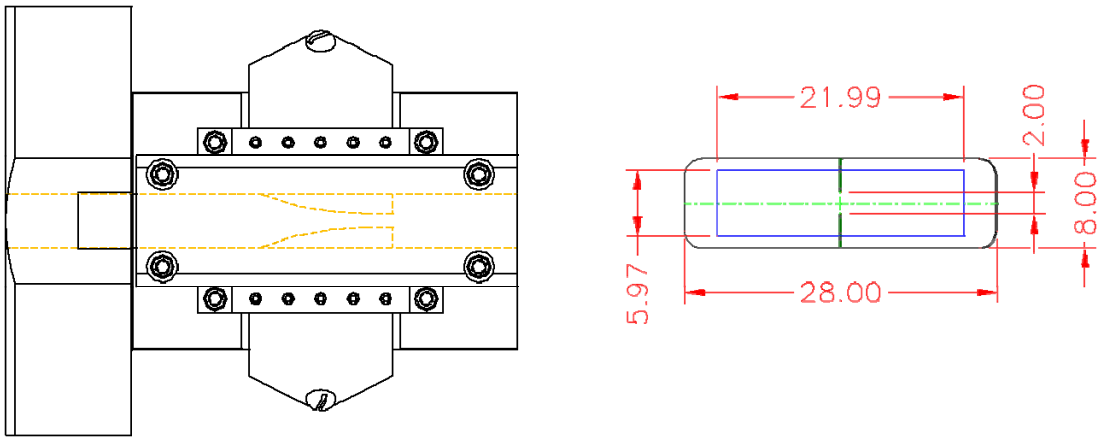

Figure 1.12 XBPM module (side view), left, used on the HXMA beamline with schematic, right, of the mask aperture, blue (inner rectangle), and XBPM aperture, black (rounded outer rectangle). Dimensions are in mm.

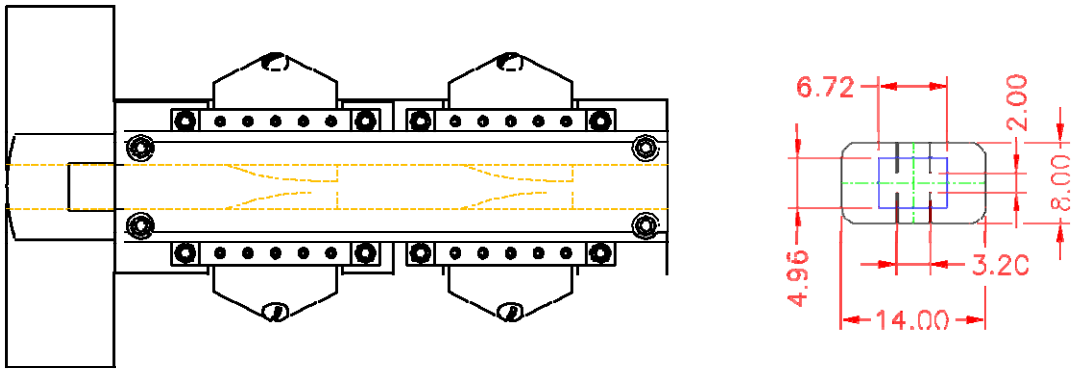

Figure 1.13 Above left is the XBPM module (side view) used on the CMCF beamline with a schematic of the aperture and blades on the right. The XBPM aperture, black (rounded outer rectangle), is larger than the mask aperture, blue (inner rectangle), to minimize interception of synchrotron radiation on the XBPM module. Dimensions are in mm.

Ideally the SR beam will travel along the central axis of each component in the FE so that each blade is placed accordingly around this axis. The blades for the two blade systems, XSR and HXMA, are positioned symmetrically above and below the axis. With the four blade monitor, CMCF, the blades are positioned symmetrically around the vertical and horizontal axis. Symmetric placement of the blades is necessary to calculate

the position of the beam centroid thus minimizing horizontal movement when measuring vertical position and vice versa. If the beam is centered in the chamber equal signals will be measured at the blades resulting in a zero or null signal; as the beam moves the signal will increase in that particular blade [22]. The change in signal strength is used to infer the position of the 1st moment, which will be discussed further in section 2.4.

Immediately the question arises of why only two blades on the XSR and HXMA beamlines while the CMCF line uses four. Essentially the horizontal field of view is completely filled with SR in the XSR and HXMA lines, from a BM and wiggler source, respectively, making it very difficult to distinguish motion in the horizontal plane and on the other hand because of the homogeneous horizontal nature of the beam, motion in the horizontal plane is less of a concern to the user. For this reason only the vertical motion of the centroid is detected. For the CMCF beamline, which employs an undulator as a source, the SR occupies only a small portion of the field of view in either vertical or horizontal directions allowing for the measurement of the centroid in both horizontal and vertical directions.

Exact blade spacing in the vertical and horizontal directions is determined, in part, by the user requirements for that particular beamline. Each beamline has specified a vertical and horizontal cone of SR that cannot be intercepted by the blades, see table 1.1. The other factor involves the power densities at the locations of the XBPM blades dictated by the vertical and horizontal SR cone. Positions of the XBPM assemblies are given in table 1.2. The position of the XBPM is measured from the source point of the beamline to the midpoint of the XBPM blade, mainly for convenient use as a reference point. In actuality the SR strikes the blade a few millimetres closer (towards) the source point than the midpoint but this adds no significant change to the calculated results.

The design parameters of the source magnets are listed in table 1.3. A complete accounting of the magnet sources used in the above mentioned beamlines can be found in the following references: 29, 30, 31, 32, 33, and 34.

Using the software modules SRCalc and SRW for the program Igor Pro v. 4.0.8 [35], the power densities and FWHMs of the SR can be simulated. With the parameters listed in tables 1.1, 1.2, and 1.3 SRCalc is able to determine the power density at a specified position and projected onto a specific beam intercepting surface contour, such

Table 1.1 Vertical and Horizontal SR cone specifications

Beamline	X-ray cone (mrad)	
	Horizontal	Vertical
CMCF	0.26	0.047
HXMA	1.50	0.168
XSR	0.289	0.289

Table 1.2 Locations of XBPMs

Beamline	Position (mm)	Placement in FE
XSR	3127.37	Cross-section after FM1
HXMA	8598.78	Attached to FM1
CMCF	8708.15	Attached to FM2

Table 1.3 Design Parameters of Magnets

Beamline:	XSR	CMCF	XAFS
Type:	Dipole (BM)	Hybrid Undulator	Superconducting Wiggler
Radius of Curvature:	7.1429 m	--	--
Period Length:	--	20 mm	33 mm
Length of Magnet Assemblies:	--	1607 mm	1023 mm
Number of Periods:	--	~ 80	31
Effective K:	--	1.83	5.91
Field Strength:	1.3543 T	(0.981 T)	(1.917 T)

as a mirror or filter. Likewise, SRW determines the spatial and power distribution of a SR beam at a given location from which the FWHM can be measured. Results of the simulations are presented in figures 1.14 to 1.19. For comparison, undulator A at the APS generates 6 kW total power with a power density of 1250 W/mm^2 at 16.2 m from the source which corresponds to the 1st XBPM position at the APS [14, 36].

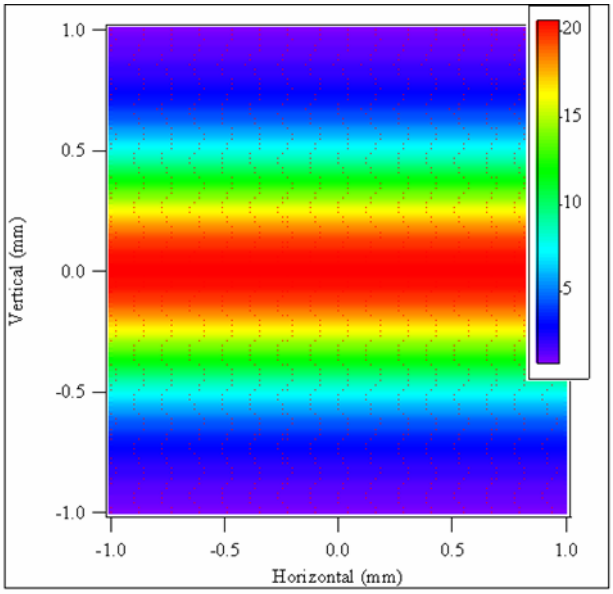

Figure 1.14 Sample of SRCalc results on incoming SR beam power density for XSR. The plot displays the absorbed power distribution of a 1 cm thick (i.e. mimicking total power absorption) diamond filter located at the XBPM position. Units of the colour bar are in W/mm^2.

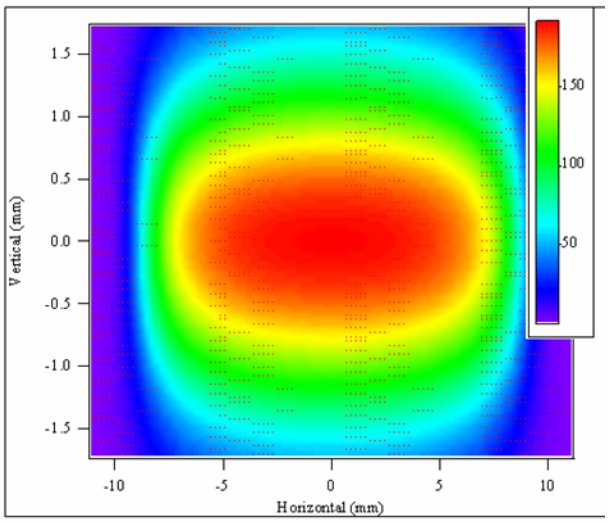

Figure 1.15 Sample of SRCalc results on incoming SR beam power density for HXMA. The plot displays the absorbed power distribution for a 1 cm thick (i.e. mimicking total power absorption) diamond filter located at the XBPM position. Units of the colour bar are in W/mm^2.

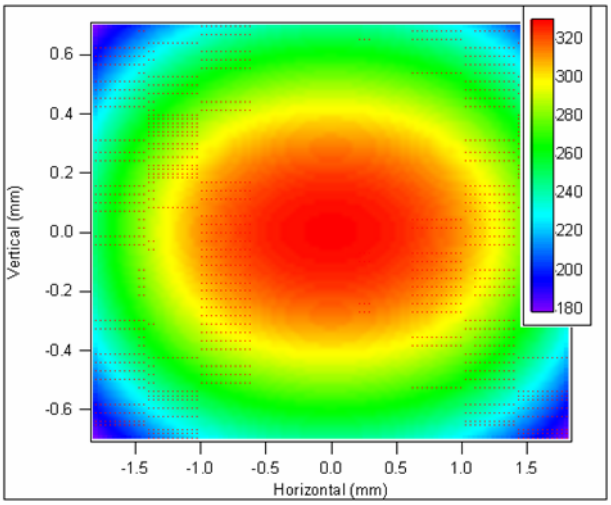

Figure 1.16 Sample of SRCalc results on incoming SR beam power density for CMCF. The plot displays the absorbed power distribution for a 1 cm thick (i.e. mimicking total power absorption) diamond filter located at the XBPM position. Units of the colour bar are in W/mm^2.

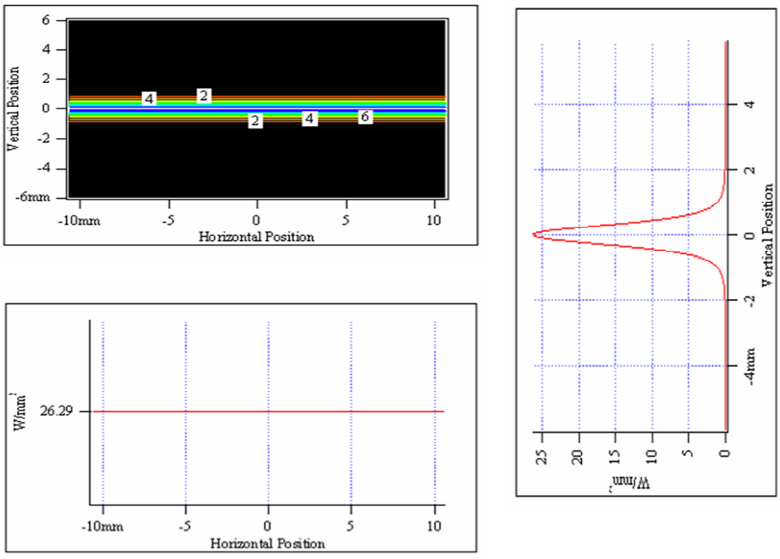

Figure 1.17 Sample of SRW results for XSR. Top left graph indicates the spatial extent of the BM beam and the power density (colour contours in W/mm^2). The bottom graph displays the horizontal line profile (constant) through the beam vertical center while the top right graph shows the vertical line profile through the beam horizontal center.

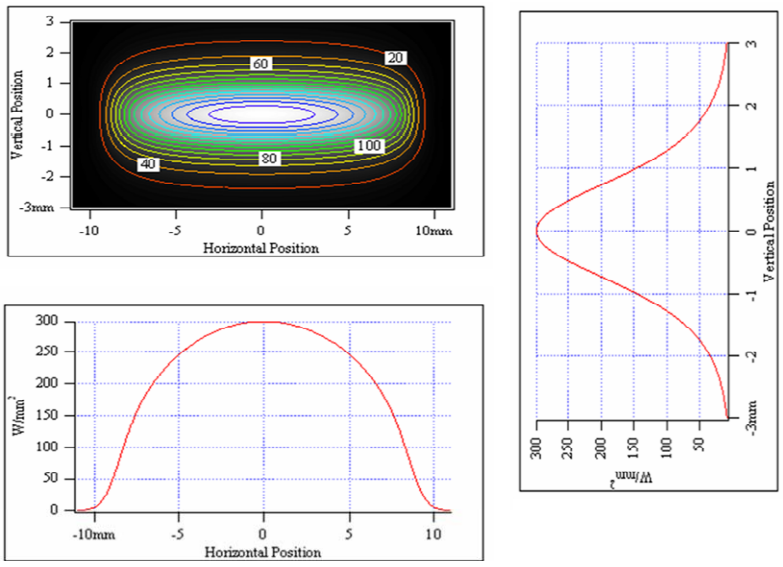

Figure 1.18 Sample of SRW results for HXMA. Top left graph indicates the spatial extent of the wiggler beam and the power density (colour contours in W/mm^2). The bottom graph displays the horizontal line profile through the beam vertical center while the top right graph shows the vertical line profile through the beam horizontal center.

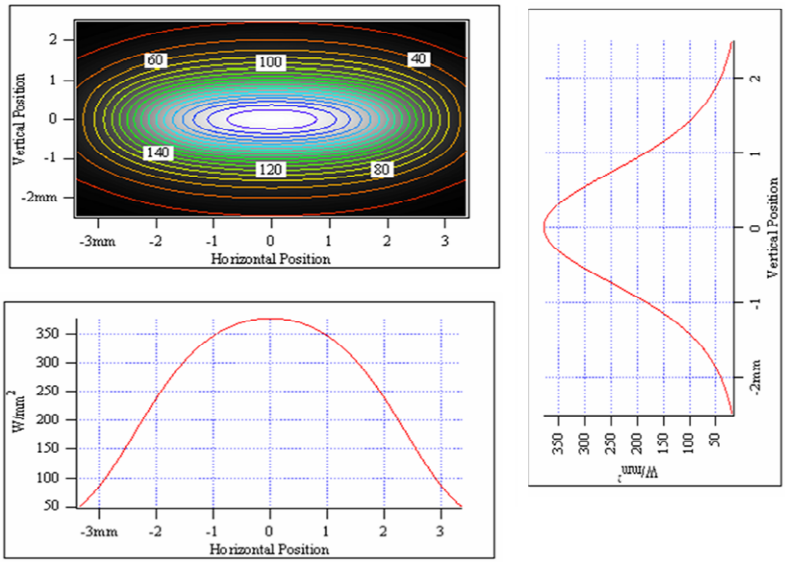

Figure 1.19 Sample of SRW results for CMCF. Top left graph indicates the spatial extent of the undulator beam and the power density (colour contours in W/mm^2). The bottom graph displays the horizontal line profile through the beam vertical center while the top right graph shows the vertical line profile through the beam horizontal center for maximum k (= 1.83).

The exact blade spacing now becomes a compromise between all of the information presented above. The FWHM curves generated by SRW are used to delineate the spatial extents requested by the beamlines. For example, for the CMCF line at 8.708 meters (position of XBPM) and 0.26 mrad horizontal SR fan, determined by experimental requirements corresponds to a 2.264 mm zone centered on zero of the FWHM curve that cannot be blocked by the XBPM blades; similarly for the vertical direction, XSR and HXMA lines.

Maps of the power density generated by SRCalc are used to indicate how much power will be loaded on to the blade at that location. Too far from the central hot spot means less power loaded onto the blades, resulting in less thermal stress, but a reduction in signal intensity; too close means the signal strength becomes stronger but the blades may suffer an appreciable amount of thermal stress. Ideally the blades are placed within the soft x-ray and VUV portion of the SR beam [14, 20, 23, 24] and do not block the hard x-ray core. Consultation with the engineers at APS, which is building the initial XBPM units, suggest that a vertical blade spacing of 2 mm for the HXMA and CMCF units, 4 mm for XSR, and a 3.2 mm horizontal spacing for the CMCF blades presents the best compromise.

But why use CVD diamond? What advantages are gained by using diamond over the materials that were or are being used? Tungsten, Mo and Al are materials that have been, and are currently in use as material for the XBPM blades [14, 21, 22, 24, 27, 37, 38]. Table 1.4 lists the properties of diamond as well as tungsten, molybdenum and aluminium. It is immediately apparent that diamond offers excellent thermal, mechanical and electrical properties [39-44]. Another consideration is the power loads that the blade material will experience. The power densities calculated by SRCalc demonstrate the type of loads that the blade material must withstand while still maintaining functionality. While all of the materials listed above are capable of withstanding the power densities calculated by SRCalc substantial cooling is required, with the exception of diamond. The other blade materials either have to be housed in blocks that are cooled or be directly cooled which adds expense and size to the XBPM assembly. Diamond significantly simplifies the cooling arrangement, due to the large thermal conductivity, allowing for a much more compact design that can be attached to existing structures as is the case for

Table 1.4 Physical Properties of Diamond, Au, W, Mo and Al

Material:	Diamond	Gold (Au)	Tungsten (W)	Molybdenum (Mo)	Aluminium (Al)
Density ($g^* m^{-3}$):	3.5	19.3	19.25	10.22	2.7
Band Gap (eV) :	5.5	--	--	--	--
Resistivity (Ω*cm):	$> 10^{12}$	$\sim 10^{-6}$	$\sim 10^{-6}$	$\sim 10^{-6}$	$\sim 10^{-6}$
Thermal Conductivity (W/m*K):	1900--2200	320	170	139	235
Thermal Expansion Coefficient ($*10^6$/K):	$(1.0 * 10^{-6})$	14.2	4.5	4.8	23.1
Atomic Number:	6	79	74	42	13

the APS and now for the CLS. As stated by Schulze-Briese [39]: "… a CVD diamond based XBPM can stay permanently in the beam."

Briefly, an explanation of why a gold coating is used instead of other materials is presented. Ideally the metal coated onto the CVD diamond blade must have a good bond with the diamond surface for good photoemission yield [14]. To this end the materials W [14] and Al [24] were initially used. However, it was discovered that within the FE environment the W chemically reacted with the diamond to form a toxic compound [45]. For that reason a new material with good photoemission yields was needed and Au was chosen. Table 1.5 lists the work functions of metals commonly used as coatings.

Table 1.5 Work Functions of Metals

Metal:	Au	W	Mo	Al
Work Function (eV):	4.8	4.55	4.6	4.28

1.4 Objectives of the Project

The objectives of this project are two-fold: primarily, implementation of the XBPM apparatus in the previously mentioned FEs and determination of the spatial resolution of the XBPM and establishing a reference point for incoming SR within the FE. This will be accomplished through calibration of the translational stages on which the fixed masks rest and incrementally stepping the XBPM through the beam to simulate actual beam position changes. Once the resolution of the translational stage is determined, be it 10 or 1 or 0.1 microns it will be possible to correlate the change in XBPM signal to beam position displacement. Specifics for each of the above are described in sections 4.1 and 4.3.

Secondly, the design and construction of a YAG (Yttrium Aluminium Garnet) imaging system has been undertaken. The system will be used to image the broad band white beam to 1) qualitatively determine the performance of the XBPM, i.e. if the XBPM registers a low position beam does the imaging system capture a corroborating image, and 2) to image the amount of background SR contamination in ID beamlines. Specifics will be discussed in section 4.4.

2 THEORETICAL BACKGROUND

The process by which current is generated on the XBPM is through the photoelectric effect and the Auger effect. In the following sections the basics of the photoelectric effect as applied to the XBPM blades are presented, as well as an estimation of the secondary electron current generated by the Auger effect. Equations used to estimate the centroid position of the SR beam will be presented as will a temperature estimation for the YAG converter crystal.

2.1 Photoelectric Effect

The physical process through which a CVD diamond Au coated XBPM operates is the photoelectric effect. An introduction to the photoelectric effect can be found in many textbooks but a succinct definition by Hecht [46] describes the effect as the "process whereby electrons are liberated from materials under the action of radiant energy." The process can be further broken down into the following steps: 1) optical excitation of the material, 2) transport of electrons within the material, and 3) electron escape into vacuum [47, 48].

The above three step model, as explained in Ref. 48, firstly has core level and valence band electrons excited into higher-energy states in the conduction band by the incident photons. Once excited, the electrons move through the solid with some fraction arriving at the surface while the remaining electrons are scattered within the material due to, principally, electron-electron scattering, and eventually are absorbed with their energy dissipated as heat. Finally, the electrons that do reach the surface must escape the potential barrier at the surface with the probability of escape dependent upon (energy) height of the barrier, electron energy greater than the barrier energy, and some non-zero velocity component with regards to surface normal – otherwise, the electrons will not have enough energy to overcome the potential barrier.

2.2 Photoelectric Effect on Au coated CVD Diamond Blades

In the majority of undergraduate texts the photoelectric effect is treated as a bulk phenomenon: photons of energy hν strike the material, e.g. a metal such as gold, at some incident angle from the surface normal with electrons emitted from the (assumed) bulk volume of the solid. However, the photoelectric effect can occur through one of three ways either alone or in conjunction:

Referring to reference 49, the three processes are:

1. Surface photoeffect, when the photocurrent depends on the electric field component of the light $|E_{\perp}|$, which is perpendicular to the surface.
2. Volume photoeffect, when the electrons come from the bulk of the metal and the photocurrent depends on the absorbed light, which is proportional to $|E|^2$, where $|E|$ is the value of the total light electric field strength.
3. Thermionic (Richardson) electron emission due to the heating of the metal by the absorbed light energy, a process proportional to $|E|$.

Reference 49 further explains that by increasing the reflectivity of the surface, achieved by using grazing incident angles, the absorption coefficient of the material decreases and suppresses the volume and thermionic emissions thus favouring the surface effect. It is then the surface, not the bulk, photocurrent that is measured.

Is the above situation applicable to the gold coated diamond blade? Consider the following: the opening angle of SR is approximately $1/\gamma$, where γ is the quotient of storage ring electron energy over electron rest mass energy. For the CLS, which has a storage ring energy of 2.9 GeV, and electron rest mass of 0.511 MeV, γ has the value

$$\gamma = \frac{2.9\,GeV}{0.511\,MeV} = 5675 \quad , \tag{2.1}$$

resulting in an opening angle of

$$\frac{1}{\gamma} \approx \frac{1}{5675} = 0.1762 \text{ mrad} \quad , \tag{2.2}$$

or roughly 0.01^0 grazing incidence everywhere on the blades except the narrow surface as measured along the blade thickness. When considering the VUV energy range of the SR

that is expected to play a major role during the normal operation of the XBPMs (blades far away from the SR central cone), the asymptotic behaviour of the SR opening angle as a function of the photon energy will increase the grazing incidence angle to approximately 0.1^0 (when $\nu << \nu_c$ the SR cone angle scales approximately as $(\nu/\nu_c)^{-1/3}/\gamma$). Since the blades are surveyed with their side surfaces parallel to the nominal direction of SR beam propagation, therefore on the side surfaces of the blade the SR photons are at a grazing incidence of no more than a few milliradians (for the ID beamline cases). With such a small angle of incidence and given the information presented above, that the type of photoelectric effect occurring on the XBPM blades is indeed a surface effect. However, volume photoeffect is likely to play a major role for the signal from the XBPM blade surface along its thickness dimension.

For the Au coated blades the photoelectric effect will not be observed until photons of energy 4.8 eV are incident on the blade. This corresponds to a wavelength of 258.48 nm which falls within the ultraviolet portion of the spectrum.

2.2.1 Photoelectric Effect on Molybdenum Blades

The photoelectric process outlined above also applies to the molybdenum blades used within the XSR XBPM unit. In the case of molybdenum blades the photoelectric effect is not observed until photons of energy 4.6 eV are incident. This corresponds to a wavelength of 269.72 nm which falls in the ultraviolet portion of the spectrum.

2.3 Secondary Electron Current due to Auger Electrons

As discussed above the primary contribution to the XBPM current is due to the photoelectric effect. But a smaller secondary electron signal due to the Auger process contributes to the total observed blade current.

Essentially the Auger process is two-step: an inner shell vacancy is formed by the excitation (SR in our case) the vacancy is then filled by a non-radiative process as illustrated in figure 2.1. The parallel inner shell vacancy relaxation process via fluorescence yield is also shown in figure 2.1. For transition energies predominately

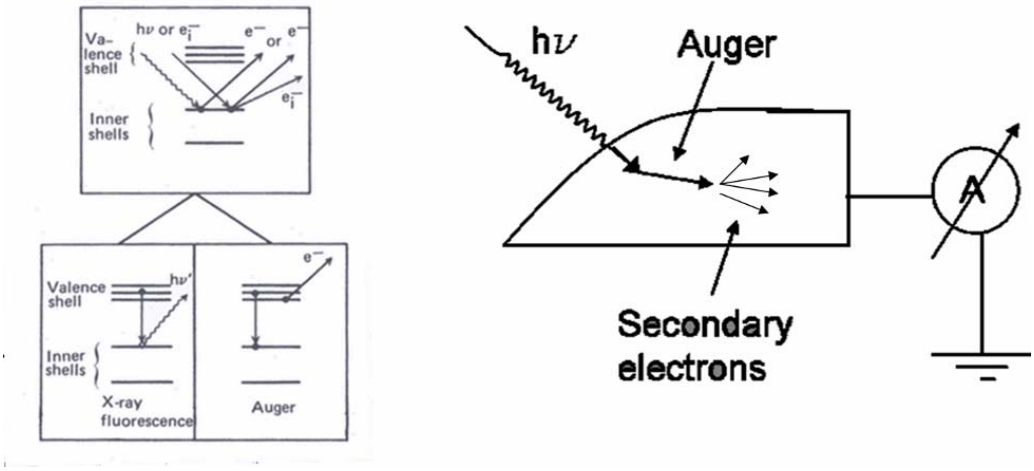

Figure 2.1 Left panel illustrates the process of photoionization after initial excitation; radiative (x-ray fluorescence) or nonradiative (Auger) process when a shell electron is ejected. Ref. 50. Right schematic illustrates electronic set up used for experiment.

below 10 keV non-radiative relaxation processes such as Auger are more favoured [50]. Following the work of Erbil et al. [51], it is possible to estimate the secondary electron current per Auger electron created within the specimen's surface.

Assuming the Auger electrons excite N secondary electrons uniformly throughout a sphere of radius R, escape length α^{-1}, at a distance x_0 away from the surface, see figure 2.2, the contribution to current is determined by the flux:

$$i(x_o) = \frac{3}{8}\frac{N}{\alpha R}\left[1 - \left[\frac{x_0}{R}\right]^2 + 2\frac{x_0}{R}\frac{1}{\alpha R} - \frac{2}{(\alpha R)^2}\right], \quad x_0 < R \tag{2.3}$$

For complete derivation, definitions and list of assumptions, refer to appendix A. This equation makes it possible to explore the detector blade response when the different core levels of gold are being excited, i.e. as the blade approaches the central cone.

Using equation 2.3 for the simple case of a 2 keV Auger electron (corresponding to the MNN Auger lines), refer to appendix A for calculation, the secondary current yield is calculated to be about 1 μA. For reference, values measured from the XBPMs currently on HXMA recorded a 173 μA blade signal at a storage ring current of 200 mA. Therefore under normal operation condition the Auger effect is not likely the major

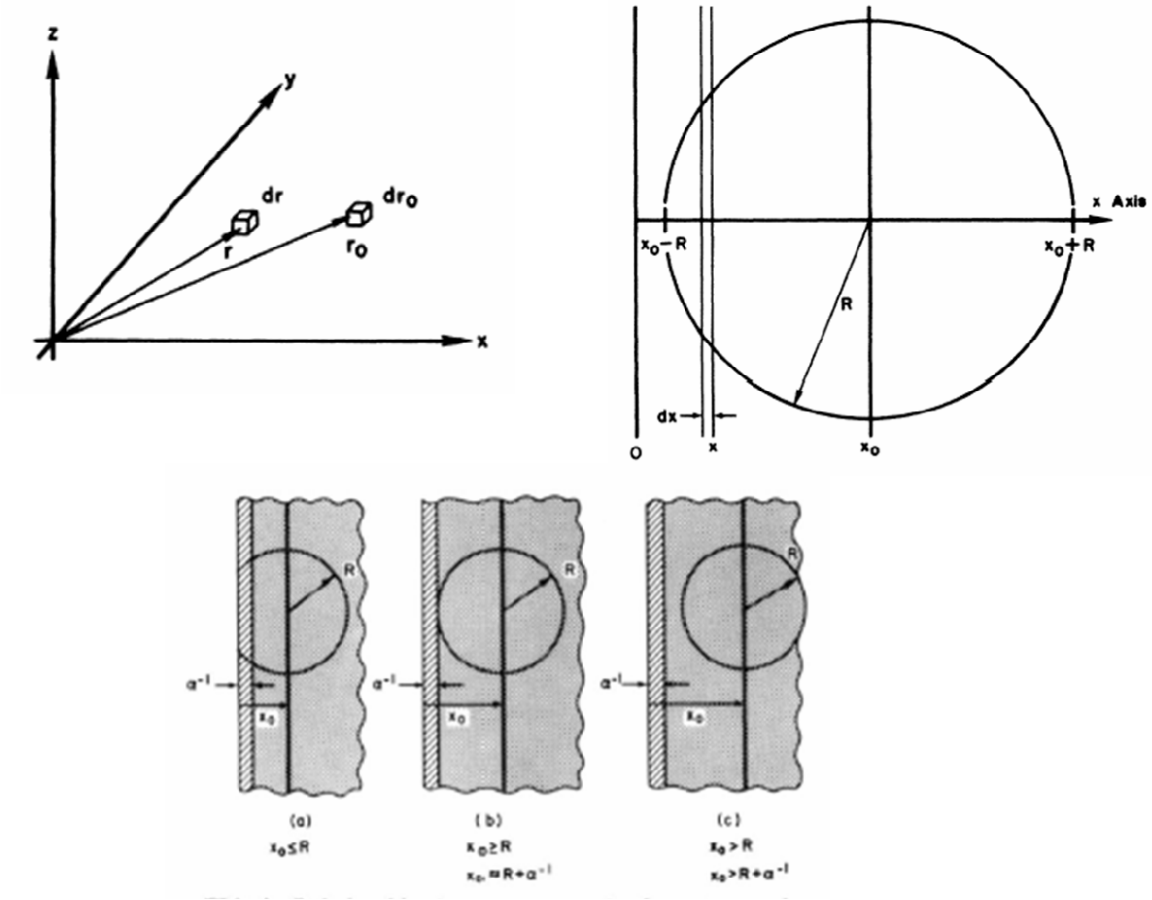

Figure 2.2 Upper left image indicates the plane of the surface sample given by (0, y, z). An Auger electron is created at position r_0 with secondary electrons produced at location r due to inelastic scattering of the Auger electron. Upper right image indicates the assumed volume in which secondary electrons are produced. Relationships between depth x, range R, and escape length α^{-1} indicated in the lower image. Ref. 51.

source of the XBPM signal. A number of caveats need to be addressed in relation to the calculated current. Contained within appendix A is a list of assumptions that went into the derivation of equation 2.3 which necessarily simplify the system being studied. In addition the efficiency of the XBPM is simply approximated by the ratio of the blade cross-sectional area facing the beam over that of the total field of view permitted by the adjacent upstream photon mask aperture. The two transverse side surfaces of the blade (SR could have grazing incidence on these) and the curved portion of the surface along blade thickness have not considered in this simple calculation, as their effect is deemed minor by simple geometrical considerations. Finally, a complete derivation would

necessarily encompass an investigation of the spectral interactions with the XBPM blades which have been crudely estimated in our calculation (Appendix A). A general conclusion which could be drawn from these estimations is that under normal operation conditions (blade not too close to the SR central cone), the Auger channel is not a dominant source for the XBPM signal, rather its the direct photoelectric effect at lower energies that plays the major role.

2.4 Determination of Centroid Position

Once the photoelectrons are ejected from the material the photocurrent of the Au coating is measured. The photocurrent is used to determine the 1st moment of the SR beam.

Generally, the centroid is determined by a simple difference over sum ratio. A schematic of the XBPM is presented in figure 2.3. Since only vertical motions are detected on the XSR and HXMA beamlines the position is simply given by

$$y = \frac{I(A) - I(B)}{I(A) + I(B)}, \tag{2.4}$$

where I (A) and I (B) are the currents measured from blades A and B, respectively. For the CMCF line the horizontal and vertical positions are given by

$$x = \frac{I(A) - I(C) + I(B) - I(D)}{I(A) + I(B) + I(C) + I(D)}, \tag{2.5}$$

and

$$y = \frac{I(A) + I(C) - I(B) - I(D)}{I(A) + I(B) + I(C) + I(D)}, \tag{2.6}$$

where I (A), I (B), I(C), I (D) are the respective currents.

As the equations currently stand calibration factors with units of length need to be applied. Without these factors the equations only provide normalized current measurements in arbitrary units and no positional value. The factors are determined experimentally when the XBPM is calibrated.

It will also be mentioned that calibration factors may need to account for any non-linear response of the detecting blades. Ideally if the synchrotron radiation is perfectly stable and the XBPM unit centered on the beam any change in signal strength should only result from diminished storage ring current – since the ring current determines the

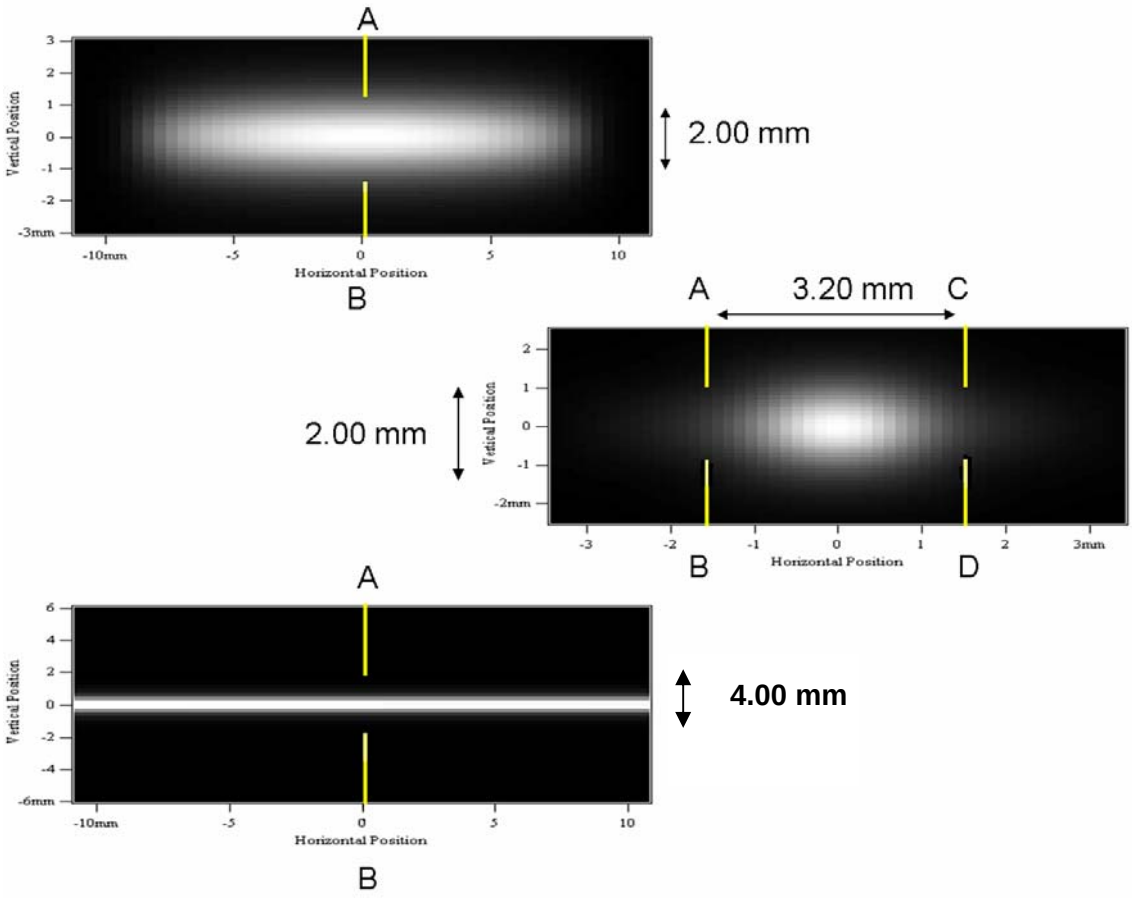

Figure 2.3 Naming convention used for each of the XBPM blades. View along the beam using simulations from SRW with schematic representation of blades and the blade separations are marked outside the images. Top image is for HXMA, middle for CMCF, and bottom image for XSR. (Note: size scales are different for each image).

number of photons produced which in turn affects the detected signal strength. If the decrease in signal strength linearly matches the natural decay of the storage ring current then calibration factors may not be needed; otherwise, a function will need to be determined to account for the non-linear response.

Also worth mentioning is the signal response of the blades as the XBPM unit is scanned through the synchrotron radiation beam. If the blade initially possesses a minimum in signal upon being scanned through the beam the distribution of the signal will follow that of a Gaussian since it is assumed that the radiation profile can be approximated by a Gaussian. This response has been used to provide 3-D maps of the synchrotron radiation spatial distribution [19] at other facilities.

So far only changes in linear position have been examined with the slope or angular position of the SR beam left unknown. Like the linear positions calculated above the angular position also provides information on where the 1st moment is located, and more importantly, both measurements are used to determine where the central x-ray cone is propagating. Ideally a second XBPM unit placed downstream of the first unit, towards the end station, would be used to determine the slope of the photon beam. However, to have a meaningful angular sensitivity the two XBPM units should have an adequate longitudinal separation distance. This separation is limited to about 1.4 m given the available FE space and the design criterion intended to not intertwine the FE control system with the user controlled beamline thus limiting the determination of angular sensitivity. These considerations plus some cost concerns lead to, at this time, only one XBPM unit to be implemented for each of the beam lines (XSR, HXMA and CMCF). To obtain the angular position the data collected by the XBPM units will be combined with the rf-BPM units in the storage ring. A four button rf-BPM assembly is located at the entrance and exit of all BMs and IDs. As the electron beam passes between the buttons an image current is generated which is used to determine the electron beam position. With the positions measured from the rf-BPMs and the XBPM the slope of the SR beam can be defined. Thus the XBPM provides the position of the SR beam while the slope indicates where the beam is propagating.

Before concluding this section the issue of cross-talk among the XBPM blades will be noted. Cross-talk between the blades, caused by the emitted electrons from one blade being collected by an adjacent blade, introduces noise into the system which effects the determination of the 1st moment. It is possible to reduce the amount of cross-talk by shielding the blades from each other but this adds size and expense to the XBPM [45].

2.5 YAG Crystal Temperature Determination

For the YAG (Yttrium Aluminium Garnet) crystal imaging system it is imperative that the crystal not suffer critical structural failure to avoid possible contamination of other beamline and storage ring components. Thus knowing the maximum amount of power that can be loaded on to the crystal, i.e. power density indicates the upper bound of power from the ID onto the crystal. Unfortunately, the available literature does not provide adequate information as to how much power loading a YAG crystal can withstand. It was then decided that the imaging system would only be used for extremely low storage ring currents, < 10 mA, on the assumption that the power density on the crystal would be much less than critical, and that the temperature of the YAG would not exceed the melting point. Determination of the YAG maximum temperature follows the work outlined in references [52 and 53], see also appendix A.

The heat conduction equation for a thin disk with an axisymmetrical Gaussian heat flux is given by

$$\frac{1}{r}\frac{\partial}{\partial r}\left(r\frac{\partial T}{\partial r}\right)+\frac{q_0}{kt}\exp\left(-\frac{r^2}{2\sigma_0^2}\right)=0 \quad , \tag{2.7}$$

with the boundary conditions that T = 0 when r = a (for convenience), and T = finite when r = 0. Integrating equation 2.7, applying boundary conditions and locating the maximum temperature at the center of the YAG disk, r = 0, results in

$$T_{\max}=\frac{q_0\sigma_0^2}{2kt}\left[E_1\left(\frac{a^2}{2\sigma_0^2}\right)+\ln\left(\frac{a^2}{2\sigma_0^2}\right)+\gamma\right] \quad , \tag{2.8}$$

where

Tmax = maximum temperature increase relative to that at the disk edge,

q_0 = maximum heat flux [W/m^2],

σ_0 = Gaussian standard deviation (for distributed heat flux) [m],

k = thermal conductivity [W/ (m·K)],

t = disk thickness [m],

a = radius of the thin disk [m],

E_1 = exponential function the first kind,

γ = Euler's constant = 0.57721….

Refer to appendix A for complete derivation.

Using a thermal conductivity of 14 W/ (m·K), a disk thickness of 200 microns and a radius of 25.4 mm, and heat flux and total power values calculated using SRCalc, equation 2.8 results in a temperature increase of

Tmax = 4519 K @ 10 mA,

for HXMA, using 4 graphite filters, and

Tmax = 442 K @ 10 mA,

for CMCF. Four graphite filters were used in the HXMA SRCalc simulation to reduce the power loaded onto the YAG crystal; without the filters the power density would be much higher.

The above temperature under-estimate is due to the boundary condition being set at T = 0 at the disk edge. A slightly different set of boundary conditions, which account for convective cooling around the edge, would provide a better temperature estimate. Referring to figure 3.6 of section 3.4.1 quickly indicates why the above estimation is used. Regardless, the maximum temperature for HXMA imposes a very low storage ring current in order for the YAG imaging system to be successfully operated. Refer to appendix A for complete calculation.

3 EQUIPMENT

The following chapter details the equipment used throughout this project. Discussed are the electronics and software controls for the XBPMs. This is succeeded by an explanation of the converting YAG crystal imaging system and components to convert the x-rays into visible fluorescence for the purpose of optical imaging.

3.1 X-Ray Beam Position Monitor

CVD diamond blades 127 +/- 50 microns thick with an approximately 1 micron gold coating are the detecting elements of the XBPM, with the exception of the monitor used on XSR. The blades used on XSR are molybdenum, 127 +/- 50 microns thick, with no gold coating. Referring to figures 1.12 – 1.14, the blades are then housed within Cu cooling modules which are either attached to FMs or placed in a vacuum cross. The two pairs of vertical blades for CMCF are longitudinally offset by 48 mm to minimize cross talk between the sets of blades. There is no offset for the blades of XSR and HXMA.

In addition to the CVD diamond blade, see figure 3.1, a Cu electrical connector and alumina insulators are clamped into the XBPM module. The electrical connector conveys the photocurrent measured by the blade to single strand in-vacuum insulated wire, similarly for XSR. The wire is silver plated copper with a Kapton insulation capable of a current of 1.5 A, and a voltage of 600 RMS (2kV DC). Attached to the other end of the wire is a push-on connector which is then connected, on the in-vacuum side, to a grounded shield 2 or 4 pin BNC coaxial electrical feedthrough. The 2 pin feedthroughs are located on the HXMA and XSR beamlines with the 4 pin located on CMCF. On the atmosphere side twisted paired cable, Belden 1883 A, is connected to the BNC feedthrough and attached to Keithley picoammeters, model 6485, located on the top of the storage ring tunnel. As mentioned previously, the HXMA and CMCF XBPMs are attached to FM which is then mounted on linear translational stages, vertical and transverse to beam direction, designed at the CLS. Similarly the XSR XBPM housed

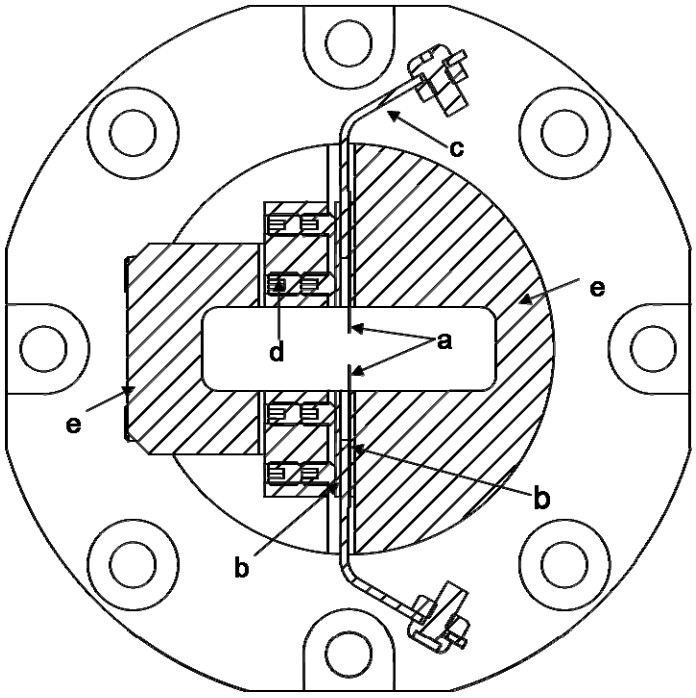

Figure 3.1 XBPM module highlighting the CVD diamond blades (a), insulators (b), electrical connectors (c), positioning screws (d), and OFHC Cu housing (e). SR is directed out of the page.

within its own vacuum cross is mounted on a linear stage. Further details of the linear stages will be given in section 3.3.2.

3.2 Keithley Picoammeter

Electrical current originating on the XBPM blades is detected by Keithley picoammeters model 6485. Capable of many tasks the meters are used primarily (for this project) for integrated current measurements and digital filtering of the input signal, i.e. the XBPM blade current.

Complying with IEEE-488.2 which defines standard commands for programmable instrumentation (SCPI) it is possible to write scripts which take advantage of the picoammeters many functions. Since the picoammeters are used widely throughout the CLS a standard control screen interface has been developed by the Control and Instrumentation division. A screen shot of the interface is provided in figure

3.2. Contained at the top of the interface is the process variable name for the meter, in this case A1408-01, the XBPM location and blade from which the current is measured, CMCF blade D, and the measured current in units of A. Immediately to the right of the display of the measured current are two fields: "read duration" and "timing." Read duration compares time stamps to indicate the amount of time actually used for the network to acquire the measurement. For example, from figure 3.2, the read (sampling) rate is 1 Hz with NPLC set to 1 results in 17 msec ((1 / 60 sec) * 1 = 0.0167 sec). The other 23 msec are comprised of internal line processing within the meter and calls from the network requesting the latest measurement for a total of 40 msec. The "timing" field provides a visual indicator of whether a measurement was successful or not. If measurement A is completed before the request for measurement B is received then "OK" is displayed. If the request for measurement B is received before A is finished then "ERROR" is displayed and the value "N/A" is recorded in the CLS archive. The timing feature was installed after the experiments described in chapter 4 took place. The other features in this control interface were not commissioned at the time of this project.

3.3 YAG Imaging System

As a secondary part of this thesis project a YAG imaging system was constructed to capture visible fluorescence images of wiggler, undulator and bending magnet synchrotron radiation. The system, to be described in the paragraphs and sections below, was designed to be general enough to accept the different synchrotron beam sizes, wiggler and undulator (refer to the top graphs of figures 1.19 and 1.20, respectively, for example), with the constraints that it not adversely effect other beamline instrumentation nor regular beamline operation, see figures 3.3 and 3.4.

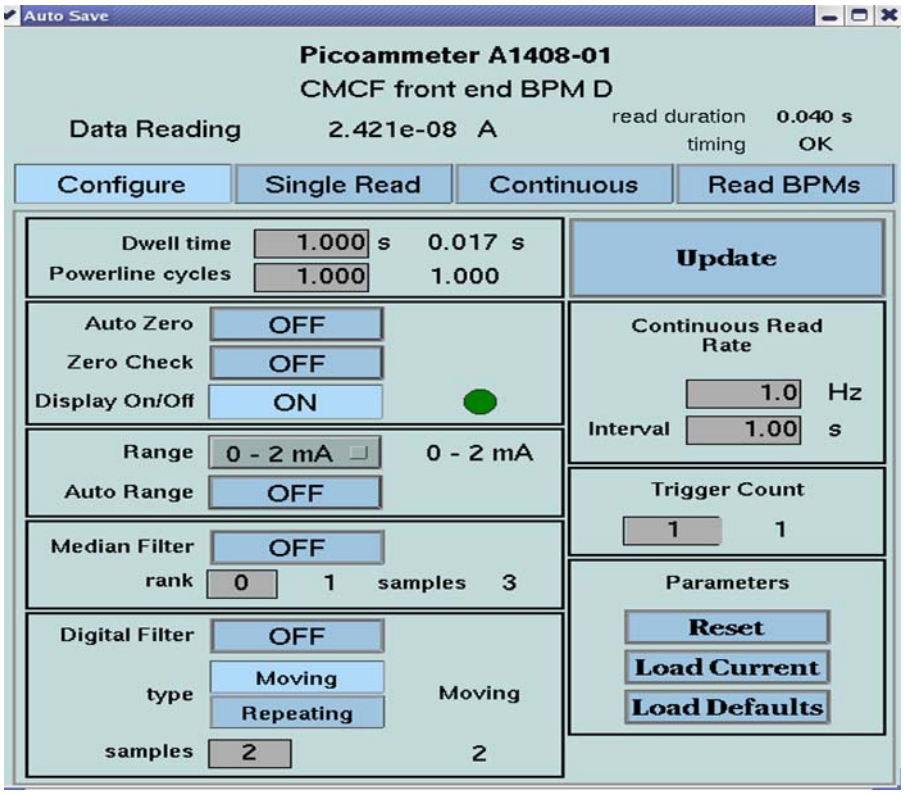

Figure 3.2 Screen shot of the picoammeter interface developed by the CLS Controls and Instrumentation division.

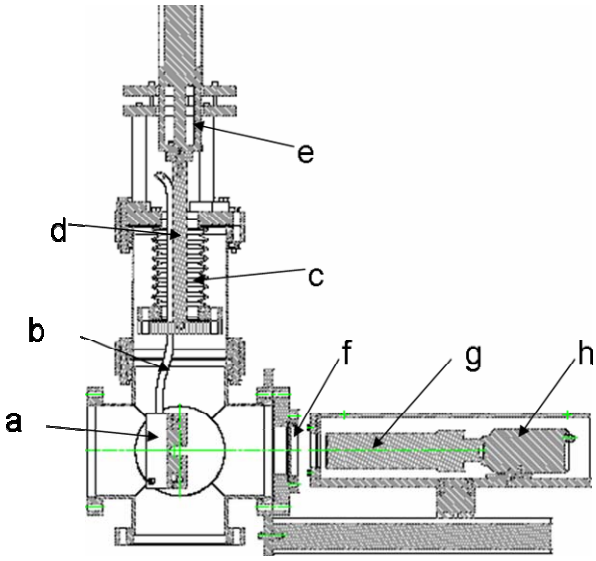

Figure 3.3 YAG Crystal Actuator assembly used for imaging synchrotron radiation. CLS drawing number 06ID-1/ME/OPT/0119100. The assembly is comprised of an OFHC copper crystal holder (a), copper cooling tube (b), bellows (c), support rod (d), pneumatic actuator (e), glass view port (f), lens (g), and CCD camera (h). SR beam is directed out of the page.

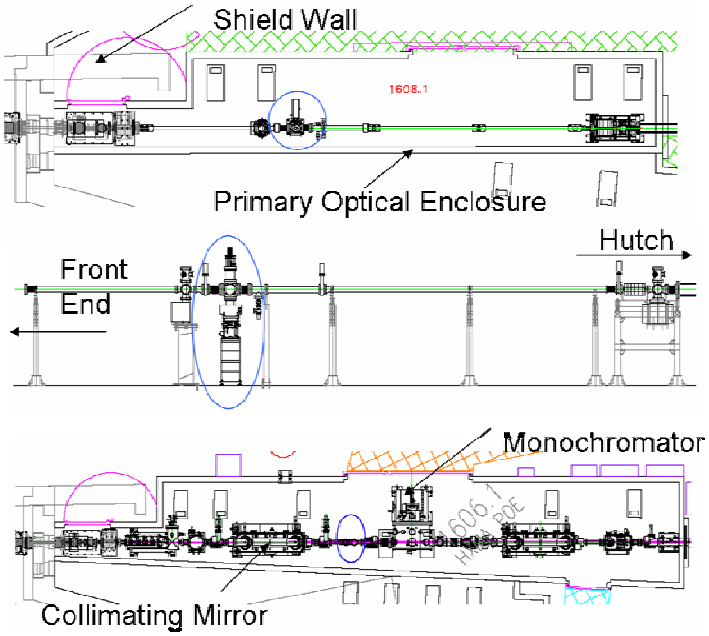

Figure 3.4 Top and middle images show placement of the YAG imaging system within the first optical hutch of CMCF (blue oval). The bottom image indicates the intended placement within the HXMA first optical hutch (blue oval).

It should be noted that initially the imaging system was to be an independent beam position monitor. To accomplish this would require the addition of encoder or potentiometer onto the YAG crystal assembly to ensure correct placement within the vacuum chamber each time the crystal was placed within the SR beam. And should the need arise to replace the crystal a method would need to be developed to accurately position the crystal assembly at 45^0 to the SR beam to properly direct the visible light out of an aperture attached to the vacuum chamber. Finally, everything would have to rigorously be surveyed into the nominal position within the optical hutch. While none of the above would add any expense to the cost of the system, the development time would have increased by several months. It was therefore decided to simply make a platform from which visible fluorescence images of the SR could be obtained.

As can be seen from figure 3.4 the placement of the YAG imaging system within the CMCF beamline does not impinge upon any other optical components. Placement within the HXMA beamline would have required that the system be situated between the first collimating mirror and the double crystal monochromator. Since the wiggler for the HXMA beamline delivers a significant amount of power even for low storage ring currents the concern raised was of possible ablation of the YAG crystal resulting in coating valuable x-ray optics. Upon consultation with the beamline scientists for HXMA and CMCF, Dr. Jiang and Dr. Grochulski, respectively, it was decided that the synchrotron imaging should only take place on CMCF thus minimizing the risk to any x-ray optics.

3.3.1 YAG Crystal Holder

The YAG crystal holder is comprised of the following components: YAG crystal, two oxygen free high conductivity (OFHC) Cu blocks, Cu tubing, bellows, stiffing rod and pneumatic actuator; see figure 3.3 and 3.5.

In order to successfully image both the wiggler and undulator radiation the YAG crystal had to be large enough to accommodate the varying SR spatial distributions. Since HXMA provides the largest spatial extents of SR beam indicating a minimum lower limit to the crystal size a YAG scintillation crystal diameter of 50.8 mm x 0.2 mm thick, both sides polished, was ordered from Crytur Ltd of the Czech Republic. The crystal is then

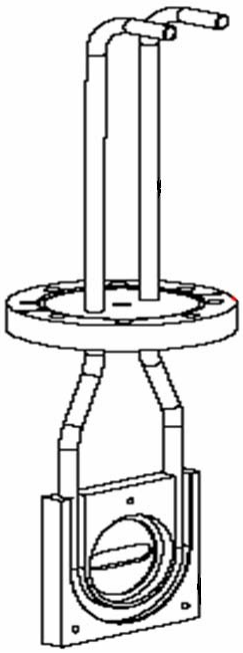

Figure 3.5 Front half of the YAG crystal cooling assembly.

housed between two OFHC copper blocks 100 mm x 100 mm x 12.7 mm with cooling applied to the block incident to the SR, figure 3.5. An aperture of 25.4 mm (H) x 12 mm (V) passes through both blocks to allow the passage of SR. A small annulus of Indium foil is pressed around the inner well of the block shown in figure 3.5 before the YAG crystal is put in place. The foil is used to increase the heat transfer between the crystal and the copper block. The second half of the copper block, not shown, has a cylindrical plug of diameter 58 mm which fits within the inner well of the first half, diameter 60 mm. A 1 mm gap between the well and the plug allows for easy escape of any trapped gases. Further, the second block is machined down to a thickness of 5 mm except at three contact points with the first half, kept at the original thickness where silver plated screws are used for attachment, thus creating another gap for gas to exit.

As seen in figure 3.5 a standard 3/8's inch copper tube is bonded to the front half of the copper block assembly to provide cooling to the YAG crystal. Water for cooling is provide by the CLS facility and is maintained at 27^0C with a flow of ~1 - 1.5 gpm for the YAG cooling. The cooling tube is also bonded to a 4-1/2 inch flange which is then attached to a bellows for vacuum-atmosphere separation. The bellows, manufactured by Standard Bellows, has an extended length of 161.36 mm, a compression of 75 mm and a

stroke of 86.36 mm which is attached to a 6-3/4 inch non-rotatable and 4-1/2 inch rotatable flanges. The cooling tubes run through the internal diameter of the bellows, which is in atmosphere thus preventing any water connections within the vacuum environment. The bellows is then enclosed within a section of beam pipe, fabricated at the CLS, which rests atop a spherical vacuum chamber, to be discussed below.

A support rod attaches to the flange pictured in figure 3.5 with the other end secured to a Bimba pneumatic actuator. The actuator has a stroke length of 75 mm and a maximum operation pressure of 140 psi. Facility supplied air, set at 100 psi, is used to raise and lower the entire YAG crystal assembly into and out the SR. A large air pressure is needed to overcome the vacuum pressure within the vacuum chamber and the spring coefficient of the bellows.

When the crystal assembly is not in use the actuator raises the blocks and crystal allowing the SR to proceed un-impeded down the beamline. A clearance of 25 mm separates the bottom of the block and the beam center when in the raised position.

Unfortunately the bonding process did not result in a uniform bond of the cooling tube with the copper block, figure 3.6. Even with the non-uniform contact, and the storage ring current limited to less then 10 mA, there is enough contact to provide adequate cooling of the YAG crystal.

3.3.2 Vacuum System and Components

Figure 3.7 displays the Vacuum chamber and components used for the YAG imaging portion of this project. Also displayed is the support column which is a copy of the type found within the FE and a spare linear stage. Descriptions will follow in the paragraphs below.

Originally intended for use on both the HXMA and CMCF beamlines (refer to section 3.3 for discussion on finalized location) the vacuum chamber size was dictated by the space limitations present within the first optical enclosure of HXMA. A six-way cross with 6 inch flanges would easily fit within the space limitations but would not provide adequate clearance for the YAG cooling block to be raised and lowered into position. An 8 inch flange six-way cross would provide more than adequate clearance for

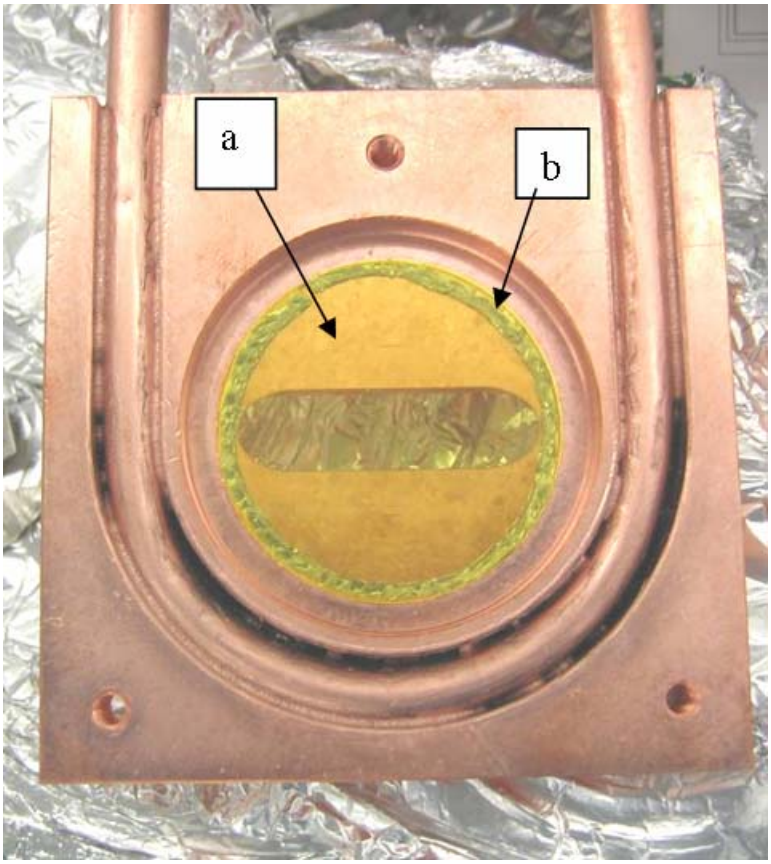

Figure 3.6 Cooling tube bonded to OFHC copper block. Many gaps are evident where the bonding agent failed to adhere to both the cooling tube and block. Also included in the picture are the YAG crystal (a) and an annulus of Indium foil (b).

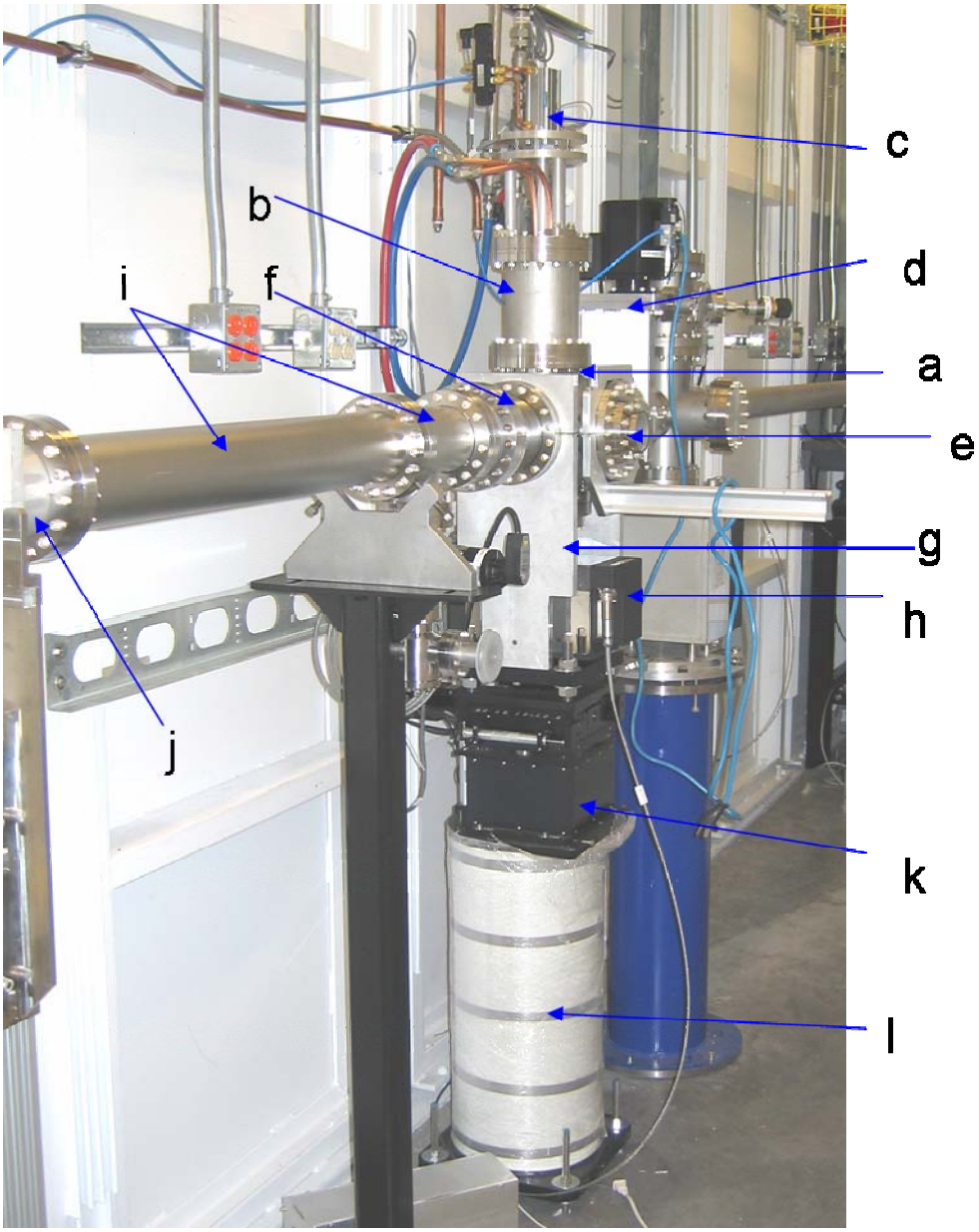

Figure 3.7 YAG crystal imaging system. The system is comprised of a vacuum chamber (a), bellows enclosure (b), pneumatic actuator (c), valve (d), aperture (e), bellows (f), stiffening supports (g), ion pump (h), beam pipe(s) (i), reducer (j), linear stage (k), and support column (l).

the YAG cooling block but would not be able to fit into the available space. Fortunately MDC, from which many vacuum components were ordered, manufactures a spherical six-way cross, 6 ¾ inch flange, that is acceptable for both space and clearance concerns.

The vacuum chamber rests atop a VacIon Plus 75 StarCell ion pump (Varion Inc.) Secured to either side of the vacuum chamber, up- and downstream, are stiffening supports. Both the supports and the ion pump are attached to a support/levelling plate that is bolted to the top portion of the linear stage.

Upstream of the vacuum chamber is a 6 ¾ inch to 6 inch reducer and a 169 mm x 6 inch O.D. bellows, not visible in figure 3.7. Connected to the bellows is a 6 inch vacuum valve used to isolate the YAG imaging system should any items need to be replaced, installed or removed. The valve is then attached to the existing beamline.

Downstream of the vacuum chamber is another bellows, 187 mm x 6 ¾ inch O.D., which is then attached to a reducer and beam pipe. For any maintenance of the YAG system the pre-existing beamline valve and the installed valve upstream of the YAG system are closed.

Before the final reducer connects the YAG system to the existing beamline a 4-way cross is attached to a small section of beam pipe. Connected to the 4-way cross is a manual angle valve, 1 ½ inch port, to allow Turbo Pump cart attachment, and a Thermal Couple and Cold Cathode gauge. The two gauges are used to measure the vacuum pressure within that particular section of beamline and are connected to the CMCF controls for active monitoring.

The support column is a ¾ version of the columns found within the FEs of the CLS. Consisting of a steel pipe 618 mm x 10.75 inch O.D., with a steel base and top plate the hollow interior is filled with silica sand to reduce mechanical vibrations being transmitted to equipment placed on top of the column. The entire support column is then wrapped in a woven ceramic cloth to reduce thermal variations thus minimizing vibrations caused by thermal expansion or contraction.

The linear translational stages, used within the FE and for the YAG imaging system, provide motion in the vertical and transverse planes, see figure 3.8. Motion in the transverse direction is generated by NEMA (size 23) stepper motor. Vertical motion also originates from a NEMA (size 23) stepper motor which is connected to an upright

machine screw jack that is capable of raising or lowering the top portion of the stage to which the transverse micro-step motor is attached. Electronic limit switches are employed to prevent the motors from moving the stage vertically or transversely beyond the desired range of motion. In addition, should the limit switches fail, physical hard-stops are attached to the stage to prevent damage to any equipment or the translational stage itself. Range of motion, including scanning ranges for the XBPMs, can be found in table 3.1. Resolution of the translational stage will be discussed in section 4.1.

Equipment is connected to the translational stage by means of a supporting plate, not shown in figure 3.8, with clearances for the four threaded bolts. Once the equipment is secured to the supporting plate, the plate can be adjusted to the required height and degree of level needed and then held fast by eight large nuts (above and below the plate).

To aid in the positioning of equipment, be it XBPM or YAG imaging system, two linear potentiometers are included to provide a reference of linear vertical and transverse position. The current measured by the potentiometers is then passed to an ADC whose value is displayed on the motor control screen under the "ADC" field. The ADC value provides a unique reference for the position of the translational stage. Resolution of the ADC value is discussed in section 4.1.

Some structural stability issues with the translational stages will be discussed in section 4.1 and in Appendix B.

Table 3.1 Scan/Motion Ranges for the Translational Stages.

Hard-stops	Vertical	+/- 3 mm
	Horizontal	+/- 3 mm
Actual Motion	Vertical	+/- 1.6 mm
(defined by Limit Switches)	Horizontal	+/- 1.6 mm

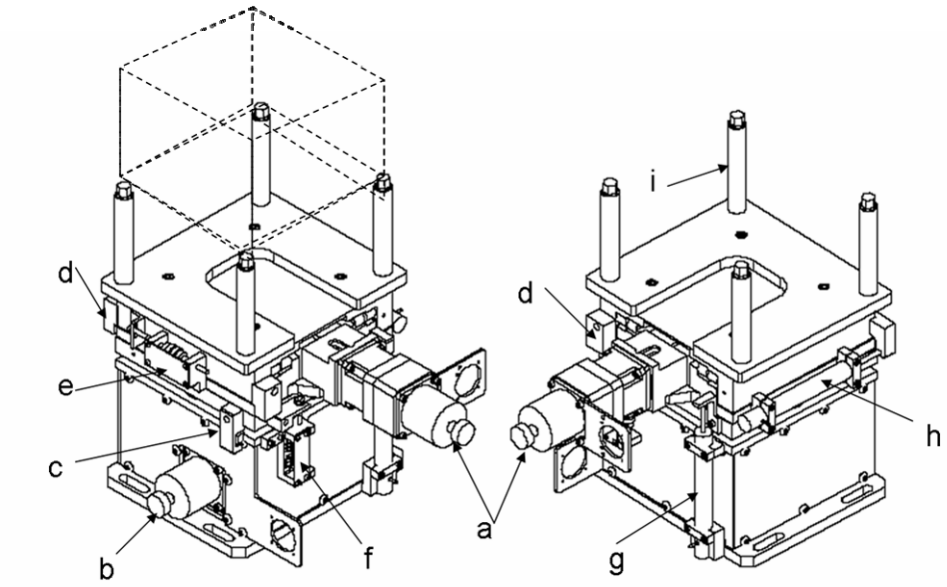

Figure 3.8 Linear translational stage used within CLS FE and for the YAG imaging system. The stage is comprised of a linear micro-step motor for horizontal motion (a), a linear micro-step motor connected to a vertical jack for vertical motion (b), vertical hard-stops (c), horizontal hard-stops (d), horizontal limit switches (e), vertical limit switches (f), vertical (g) and horizontal (h) potentiometers, and threaded support bolts (i).

3.3.3 Camera and Lenses

A Phillips LTC 0335/60 monochrome CCD camera was used for the converted x-ray imaging. The imager consists of a 1/3 inch interline CCD with an active pixel area of 768 pixels (H) x 494 pixels (V) and a resolution of 570 television lines [54]. Attached to the camera are InfiniMini^{TM} video lenses ordered from Edmund Industrial Optics which were selected using the equations listed in the Edmund catalogue and on the website to estimate the system magnification and the total system resolution.

The primary magnification (PMAG), which is the work done by the lens, is the ratio between the sensor size and the FOV

$$PMAG = \frac{Sensor\ size\,(H)}{FOV\,(HOR.)} = \frac{4.8\,mm}{30\,mm} = 0.16\,\mathrm{X}\,, \tag{3.1}$$

where the sensor size is given by the horizontal dimension of the CCD, and the FOV is the area of the object to be viewed on the monitor.

The total magnification from the object to the image on the monitor, i.e. the work done by the whole system, is determined by

$$System\ Magnification = PMAG\ x\ \frac{Monitor\ Size\,(diag.)}{Sensor\ Size\ (diag.)} = 0.16\,x\,\frac{406.4\,\text{mm}}{6\,\text{mm}} = 10.84\,\text{X}\,, \tag{3.2}$$

In order to determine the system resolution the camera resolution must first be calculated (where lp = line pairs),

$$\begin{aligned} Camera\ resolution\,(\text{lp/mm}) &= TVL\,(horz.)\,x\,\frac{1.33}{2\,x\,Sensor\ size\ (H)} \\ &= 570\ x\ \frac{1.33}{2\,x\,4.8\,\text{mm}} = 79\,\text{lp/mm or } 12.7\,\mu\text{m} \end{aligned}\,, \tag{3.3},$$

which is substituted into the following equation that provides a measurement of an imaging systems ability to reproduce object detail,

$$System\ resolution\ (\mu\text{m}) = \frac{Camera\ resolution\,(\mu\text{m})}{PMAG} = \frac{12.7\,\mu\text{m}}{0.16} = 79.4\,\mu\text{m}\,. \tag{3.4}$$

The video lenses, consisting of the InfiniMini™ Main body and an IF backend converter, provides the necessary magnification and covers the required FOV as can be seen from the general specifications [55]:

- Lens magnification: 0.4 X to 0.12 X
- System magnification: 16.4 X to 5 X
- Field of View (FOV): 16 mm to 52 mm
- Working distance: 314 mm to infinity

As can be seen from figure 3.3 the camera and lens are housed within an aluminium box which is secured to an optical rail by a positioning mount. A holder is clamped around the flange containing the viewport to which the optical rail is attached. An aperture of radius 26 mm allows the light to pass into the aluminium housing. The front part of the housing is constructed so a filter can be slid into position in front of the aperture. Neutral density filters, 50 mm x 50 mm, of an optical density 0.15 and a 70% transmission where used.

3.3.4 Image Acquisition Software

The commercially available frame grabber and software package Spiricon, distributed by Optikon Canada, which can gate, digitize and control image integration time is used for image acquisition. Designed for beam profile analysis of laser beams the software package is finding use at several synchrotron facilities for analysis of visible and converted x-ray light [56]. In addition to image capturing the software package is able to perform a number of statistical analysis' to quantitatively describe the beam profile all of which can be logged for further study.

Primarily used for image capture in this project the following statistical options were logged [57]:

- 4-Sigma beam width which is defined as 4 times the standard deviation of the energy distribution evaluated separately in the X and Y transverse directions over the beam intensity profile
- Centroid location found by calculating the center of mass of all the pixels
- Elliptical beam which computes and displays the orientation of an elliptical beam and a coefficient of roundness
- Whole Beam fit which performs a least squares bivariate normal equation fit.

During the post processing the above information, as well as the images can be retrieved for further analysis

4 EXPERIMENTAL PROCEDURES AND RESULTS

This chapter will cover the experimental procedures and techniques used to determine the spatial resolution of the XBPMs used at the CLS. Before the spatial resolution of the XBPMs can be determined the resolution of the translational stages upon which the XBPMs are attached must be acquired. Then the "best" sample reading rate, which depends on the number of power line cycles (NPLC) and dwell time, must be acquired. Once the resolution of the stage and reading rate are settled it is then possible to start scanning the XBPM in order to determine its spatial resolution.

And finally, the procedure used for the acquisition of SR images obtained by the YAG crystal will be detailed.

4.1 Translational Stage Calibration

The calibration tests made use of the stepper motor control developed by the Controls and Instrumentation group within the CLS. This is the standard motor control used throughout the facility. Also used were two Heidenhain encoders (Spectro 3078, length gauges) which are able to resolve linear motion on the micron scale (0.5 μm), and voltage supply rack, to determine the resolution of the translational stages. The encoders were positioned orthogonally to each other and as close to perpendicular on the translational stage top as possible. This allowed the simultaneous recording of vertical motion with any possible horizontal motion and vice versa.

Before any tests were undertaken, the motor current and micro step size on all the CLS microstep motor drivers were set to the same values. The motor current was set to a value of 7 which corresponds to 1.4 Amps being applied to each motor winding for each phase of the stepping. The micro step size was set to a value of 'A' which corresponds to 10 microsteps per motor step.

The calibration procedure, refer to appendix D, was used between the months of May and July 2005, during the shut down periods of the CLS and when the encoders

where not being used by other scientists for beamline commissioning or by the Magnet Mapping facility. Results for each of the beamlines follow.

Figures 4.1 to 4.3 display the results of scanning tests done on the HXMA beamline. Figures 4.1 and 4.2 display the linear relations between the encoder and ADC and the ADC and number of steps; as mentioned above, a non-linear relation would be indicative of a faulty component. Figure 4.3 plots the encoder value versus step from which is determined the resolution of the translational stage. For this initial scan a step size of 100 was used to move the motor from limit to limit. Also displayed on the plot is a fit calculated by Excel where the slope of the fit indicates the calibration of the translational stage.

During the scan over the smaller range a step size of 10 was used. Only two scans were able to be accomplished over a total encoder range of 200 microns (figures C.1 to C.3 in appendix C) before the equipment was needed elsewhere in the facility. Also worth noting from figure C.1, the resolution of the ADC is ~5 microns—for micro-stepping movement below 5 microns the number of steps must be counted in order to ensure the stage has moved the requisite number of microns.

From figures 4.3 and C.3, the slopes of the fits are both approximately 0.25 μm/step. Refer to table 4.1 for all results of the minimum resolved stage motion.

The above procedure was used as well for the CMCF and XSR beamlines but a step size of 100 was also used for the smaller scans to decrease the amount of time per scan due to the high demand of the encoders. Results for CMCF are presented in figures C.4 to C.9 with results for XSR presented in figures C.10 to C.12 in Appendix C.

From figures C.4 to C.6 it is very clear that there is a problem with the CMCF translational stages over the limit-to-limit scan range, evidenced by the non-linear relation between the various values, i.e. the encoder, ADC and step size. Even over the smaller range scans, figures C.7 to C.9, there are visible ‘undulations’ of data points among the various relations, encoder vs. ADC etc. The cause for the non-linear performance of the CMCF XBPM translational stages was determined during the October 2005 shutdown with the fault originating from the downstream photon shutter (a mechanical problem that the flexible linkage between the XBPM and the shutter assembly needs to be modified, see Appendix B).

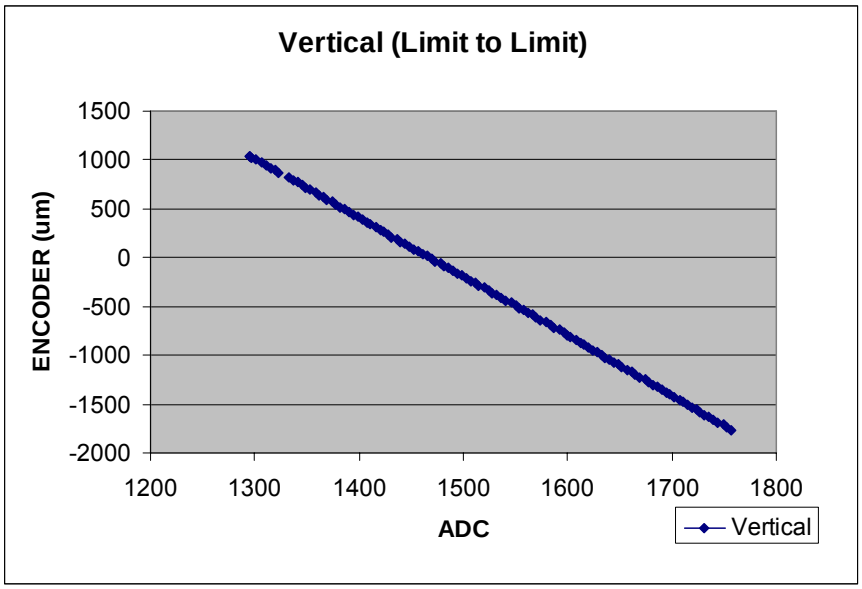

Figure 4.1 Vertical translation stage for the HXMA XBPM moved from limit to limit. Displayed are the changing encoder values versus the changing ADC values.

Table 4.1 Vertical Resolution of the Translational XBPM Stages

HXMA	CMCF	XSR
0.25 μm/step	0.30 μm/step	0.26 μm/step
0.25 μm/step	0.25 μm/step	
Average: 0.25 μm/step *		

* Values from CMCF not included in average. Refer to text of section 4.1 and Appendix B for explanation

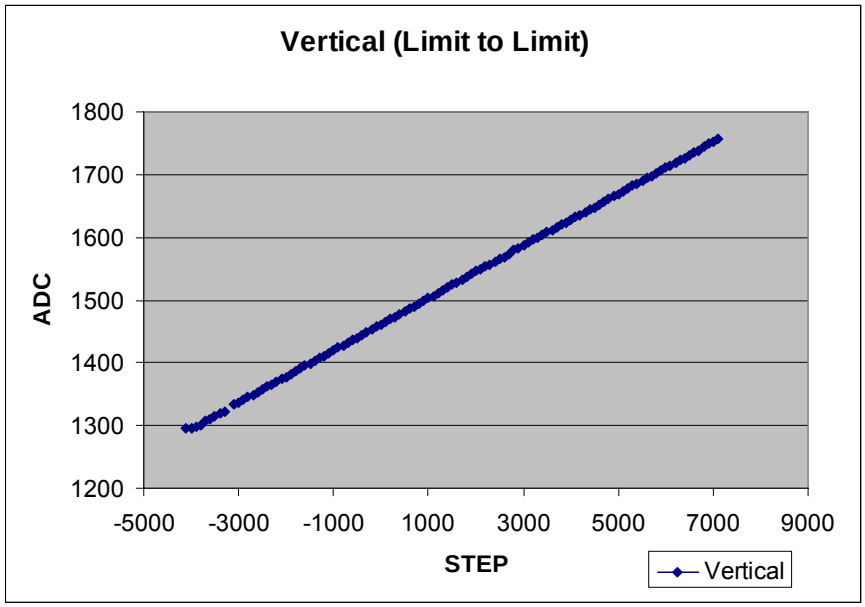

Figure 4.2 ADC value for the HXMA XBPM increases linearly as the translational stage is moved from one limit to the opposite limit. A small amount of backlash is present at the beginning of the scan.

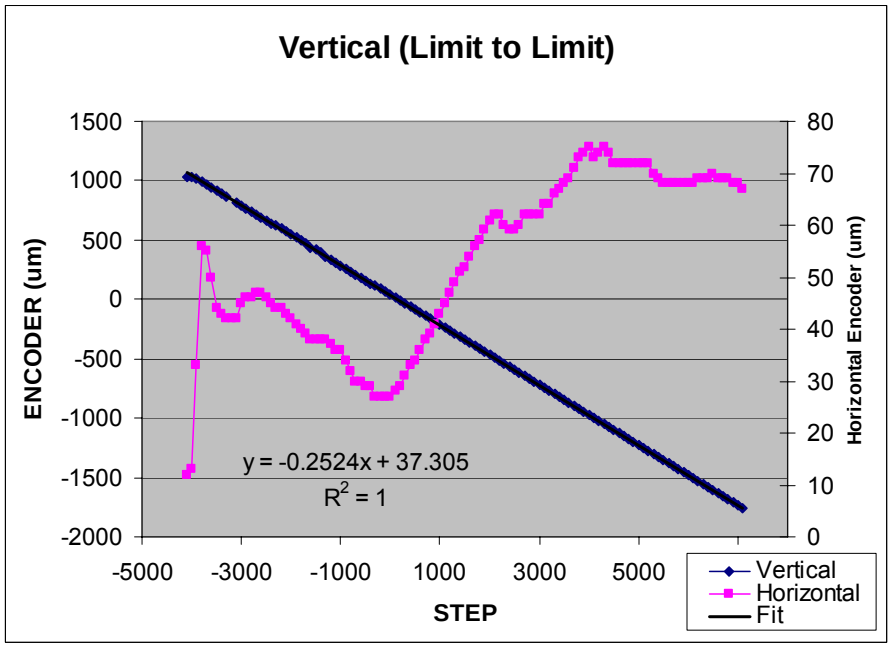

Figure 4.3 Encoder versus step size for the vertical translational XBPM stage used on HXMA over a range of 3 mm. Also displayed is the amount of coupled horizontal motion during the vertical scan. The slope of the fit indicates the calibration of the stage.

Within the CMCF front end the fixed mask to which the XBPM is attached is immediately succeeded by a connecting bellows to a "block" type photon shutter.

Unlike the other photon shutters currently used throughout the facility which are a "cantilever" type that raises or lowers only one end of the shutter, the "block" type is entirely raised or lowered with any translational forces supposedly damped by the bellows. Unfortunately the connecting bellows was under too much tension so that when the CMCF shutter was opened a translational force was transmitted through the bellows to the fixed mask resulting in a torque being applied to the motor stages. Subsequent opening and closing of the shutter during the CMCF commissioning phase have resulted in the translational stage becoming structurally loose so that pushing on the stage with a person's hand will move the stage by several millimetres. Engineers at the CLS are currently working on ways to rectify the problems.

As a consequence no experiments were performed using the XBPM on the CMCF beamline. Also, due to un-expected control issues on the HXMA beamline a limited set of experiments were performed using that beamlines XBPM. The following sections deal (almost) exclusively with the XBPM on the XSR beamline, except for sections 4.3.2 and 4.4.

Before concluding this section it will be mentioned that final surveys of the FMs and vacuum chamber used to house the XBPMs took place during July 2005. The surveys, conducted by the technicians within the Engineering and Technical Services group of the CLS, ensured that the masks and vacuum chamber where in the proper design locations for optimum beamline performance. In conjunction with moving the translational stages the technicians also employed the use of a theodolite and reflectors to accurately position the equipment. The reflectors are placed within standard reference points (fiducials) to aid in the accurate placement of all equipment to within +/- 200 mm of the theoretical design position. Once the FMs and vacuum chamber have been surveyed into position, thus defining a zero or "origin" position, the horizontal and vertical ADC values for the translational stages are recorded. ADC values for each beamline that has an XBPM are listed in table 4.2.

Table 4.2 ADC values (arb. units) denoting the zero position for the XBPMS

	HXMA	XSR	CMCF
Horizontal	1898 +/- 1	2759 +/- 1	2267 +/- 1
Vertical	1521 +/- 1	1708 +/- 1	2077 +/- 1

4.2 Keithley Picoammeter Reading Rate

As mentioned in section 3.2 the Keithley picoammeters are connected to the CLS data archive via RS-232 cables with the archive being updated every second. As can be seen from the inset in figure 4.4 the time stamp, which should update every second has multiple entries per second with the XBPM current measurements being duplicated.

A MatLab script was developed, Appendix D, to determine the rate at which data could be polled over the CLS network with the maximum rate being observed before duplication of values occurs – duplication occurs when the network doesn't have a new value ready. Each of the update scan times on the Keithley meters were set with identical reading rates while the variable polling rate from 0.1 – 1 second was set within the MatLab script. Figure 4.5 provides an example of two of the tests with the left plot displaying a polling rate of 0.1 seconds and the right at 0.2 seconds. From the left plot it can be seen that data points are duplicated producing flat tops or bottoms to the peaks of the graph. This duplication of points is not evident in the right plot or for polling rates from 0.2 – 1 second thus setting a range for any subsequent scans.

The above was done prior to the software upgrades for the Keithley pico-ammeters, see figure 3.2. Once the software was upgraded, and the archive channel re-booted, the archive data for the XBPMs updates according to the sampling rate and power line cycles set on the Keithley meter. Previous to the upgrade the sampling rate of the meter was set at 1 Hz with the power line cycles limited to the interval 1 – 6. After the upgrade the sampling rate could be chosen from 0.2, 0.5, 1, 2, 5 or 10 Hz with the number of power line cycles (NPLC) set in the range 1 – 60. However, this does not affect the rate at which data can be polled by MatLab over the CLS network.

```
# GNUPlot Exporter V 1.9.1
#
# A1406-01:uA:fbk [uA]
11/30/2005 12:20:00.000000000   147.19
11/30/2005 12:20:00.000000000   147.19
11/30/2005 12:20:00.000000000   148.208
11/30/2005 12:20:03.000000000   148.694
11/30/2005 12:20:03.000000000   148.603
11/30/2005 12:20:03.000000000   149.059
11/30/2005 12:20:06.000000000   148.775
11/30/2005 12:20:06.000000000   148.775
11/30/2005 12:20:06.000000000   149.413
11/30/2005 12:20:06.000000000   149.251
11/30/2005 12:20:09.000000000   149.671
11/30/2005 12:20:09.000000000   149.671
11/30/2005 12:20:09.000000000   150.02
11/30/2005 12:20:12.000000000   150.052
11/30/2005 12:20:12.000000000   150.052
11/30/2005 12:20:12.000000000   150.983
11/30/2005 12:20:15.000000000   151.028
```

Figure 4.4 Screen shot of the CLS data archive for the HXMA XBPM. Updates to the archive should occur every second but is not evident.

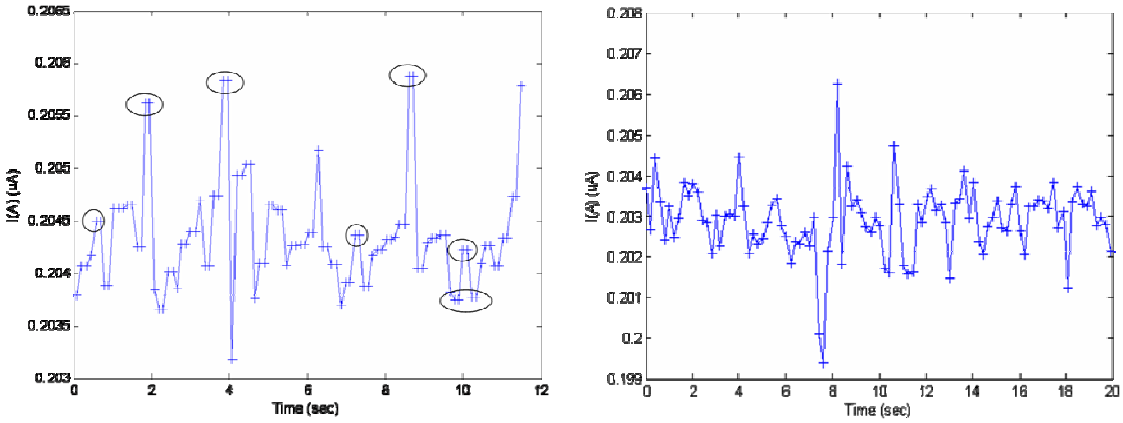

Figure 4.5 Examples of the MatLab sampling rate from the XSR XBPM. Both tests occurred within minutes of each other with the left sampled at 0.1 sec and the right at 0.2 sec. Notice in the left figure there is duplication of values.

Once the optimum polling rate was determined the NPLC on the meter had to be established. The NPLC sets the integration time of the Keithley meter which affects the

amount of reading noise and the ultimate reading rate of the multi-meter before the measurement is sent to a computer or other data acquisition device (section 3.2). For illustrative purposes suppose that an ultra-fast diffraction experiment is taking place on the CMCF beamline the duration of which lasts only 0.5 seconds (2 Hz). To ensure that the SR beam has remained relatively stationary during the duration of the experiment the Keithley picoammeter connected to the XBPM needs to sample twice as fast, or 0.25 seconds (4 Hz). Of the sampling rates available, 5 or 10 Hz presents the only two options. For each of the sampling rates the NPLC was systematically advanced from 1 to 6, with the advice that higher values for the NPLC would not result in a ready measurement for the archive. To determine which value was "best" two different methods were used.

The first method was simply to visually inspect the archive record to verify that a measurement had indeed taking place. If the integration time set by the sampling rate and NPLC is such that a measurement has been completed then a numerical value will appear within the archive, otherwise the value "N/A" is displayed. Refer to figure 4.6 for examples. Note: with the upgrade to the Keithley meter software and control panel, the "timing" field, which displays "OK" or "ERROR", it is no longer necessary to check the CLS archive for recorded values – though a quick visual inspection is prudent.

The second method involved calculating the variance of the measured XBPM current under the condition that the calculation treats the network error (#N/A in Fig. 4.6) as a zero input, therefore a smaller variance for a given frequency and NPLC indicates a reading closer to the actual rms value for the current. For each frequency (5 or 10 Hz) and NPLC (1 – 6) three samples were recorded. Each sample was 60 seconds in duration and each was spaced 30 seconds apart, with the data stored on the CLS archive and later moved to an Excel spreadsheet. Spacing is achieved simply by selecting the "configure" button on the picoammeter control panel, figure 3.2. Doing so automatically stops the meter from taking any further readings and freezes the value at the last recorded measurement.

Once the samples were acquired the ratio of the XSR XBPM currents were calculated. By comparing the currents measured from the XBPM blades any anti-

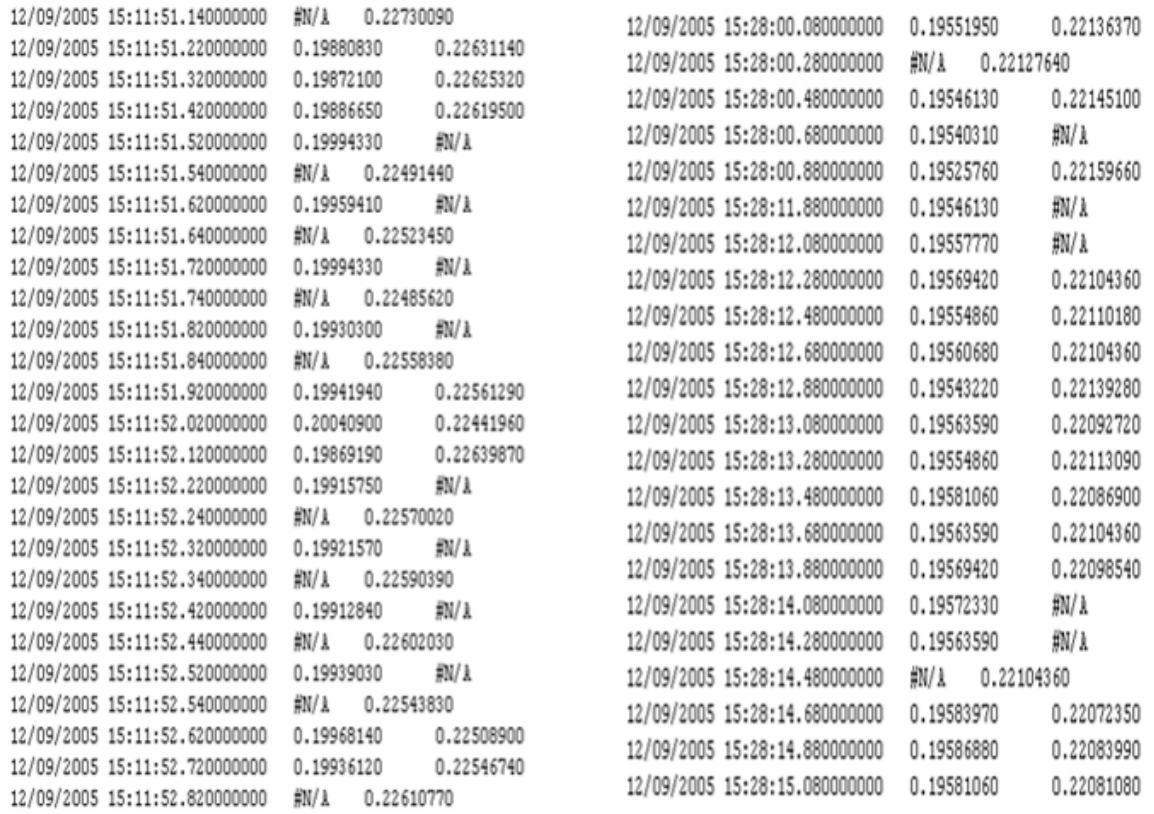

12/09/2005 15:11:51.140000000	#N/A	0.22730090
12/09/2005 15:11:51.220000000	0.19880830	0.22631140
12/09/2005 15:11:51.320000000	0.19872100	0.22625320
12/09/2005 15:11:51.420000000	0.19886650	0.22619500
12/09/2005 15:11:51.520000000	0.19994330	#N/A
12/09/2005 15:11:51.540000000	#N/A	0.22491440
12/09/2005 15:11:51.620000000	0.19959410	#N/A
12/09/2005 15:11:51.640000000	#N/A	0.22523450
12/09/2005 15:11:51.720000000	0.19994330	#N/A
12/09/2005 15:11:51.740000000	#N/A	0.22485620
12/09/2005 15:11:51.820000000	0.19930300	#N/A
12/09/2005 15:11:51.840000000	#N/A	0.22558380
12/09/2005 15:11:51.920000000	0.19941940	0.22561290
12/09/2005 15:11:52.020000000	0.20040900	0.22441960
12/09/2005 15:11:52.120000000	0.19869190	0.22639870
12/09/2005 15:11:52.220000000	0.19915750	#N/A
12/09/2005 15:11:52.240000000	#N/A	0.22570020
12/09/2005 15:11:52.320000000	0.19921570	#N/A
12/09/2005 15:11:52.340000000	#N/A	0.22590390
12/09/2005 15:11:52.420000000	0.19912840	#N/A
12/09/2005 15:11:52.440000000	#N/A	0.22602030
12/09/2005 15:11:52.520000000	0.19939030	#N/A
12/09/2005 15:11:52.540000000	#N/A	0.22543830
12/09/2005 15:11:52.620000000	0.19968140	0.22508900
12/09/2005 15:11:52.720000000	0.19936120	0.22546740
12/09/2005 15:11:52.820000000	#N/A	0.22610770

12/09/2005 15:28:00.080000000	0.19551950	0.22136370
12/09/2005 15:28:00.280000000	#N/A	0.22127640
12/09/2005 15:28:00.480000000	0.19546130	0.22145100
12/09/2005 15:28:00.680000000	0.19540310	#N/A
12/09/2005 15:28:00.880000000	0.19525760	0.22159660
12/09/2005 15:28:11.880000000	0.19546130	#N/A
12/09/2005 15:28:12.080000000	0.19557770	#N/A
12/09/2005 15:28:12.280000000	0.19569420	0.22104360
12/09/2005 15:28:12.480000000	0.19554860	0.22110180
12/09/2005 15:28:12.680000000	0.19560680	0.22104360
12/09/2005 15:28:12.880000000	0.19543220	0.22139280
12/09/2005 15:28:13.080000000	0.19563590	0.22092720
12/09/2005 15:28:13.280000000	0.19554860	0.22113090
12/09/2005 15:28:13.480000000	0.19581060	0.22086900
12/09/2005 15:28:13.680000000	0.19563590	0.22104360
12/09/2005 15:28:13.880000000	0.19569420	0.22098540
12/09/2005 15:28:14.080000000	0.19572330	#N/A
12/09/2005 15:28:14.280000000	0.19563590	#N/A
12/09/2005 15:28:14.480000000	#N/A	0.22104360
12/09/2005 15:28:14.680000000	0.19583970	0.22072350
12/09/2005 15:28:14.880000000	0.19586880	0.22083990
12/09/2005 15:28:15.080000000	0.19581060	0.22081080

Figure 4.6 Determining the number of power line cycles (NPLC) for the Keithley picoammeters. The columns on the left are a sampling of the CLS data archive XBPM current measurements for when the ammeter is set to 10 Hz and an NPLC of 1. The columns on the right demonstrate when the ammeter is set to 10 Hz and an NPLC of 5.

correlation of measured signal is an indication of beam movement. The ratio of currents then highlights possible beam motion from the random noise of the system. Prior to calculating the variance any large valued outliers are removed to minimize the effect on the variance calculation. Refer to figure 4.7 for an example and table 4.3 for results. Based on the above a frequency of 10 Hz with a NPLC of 5 was chosen.

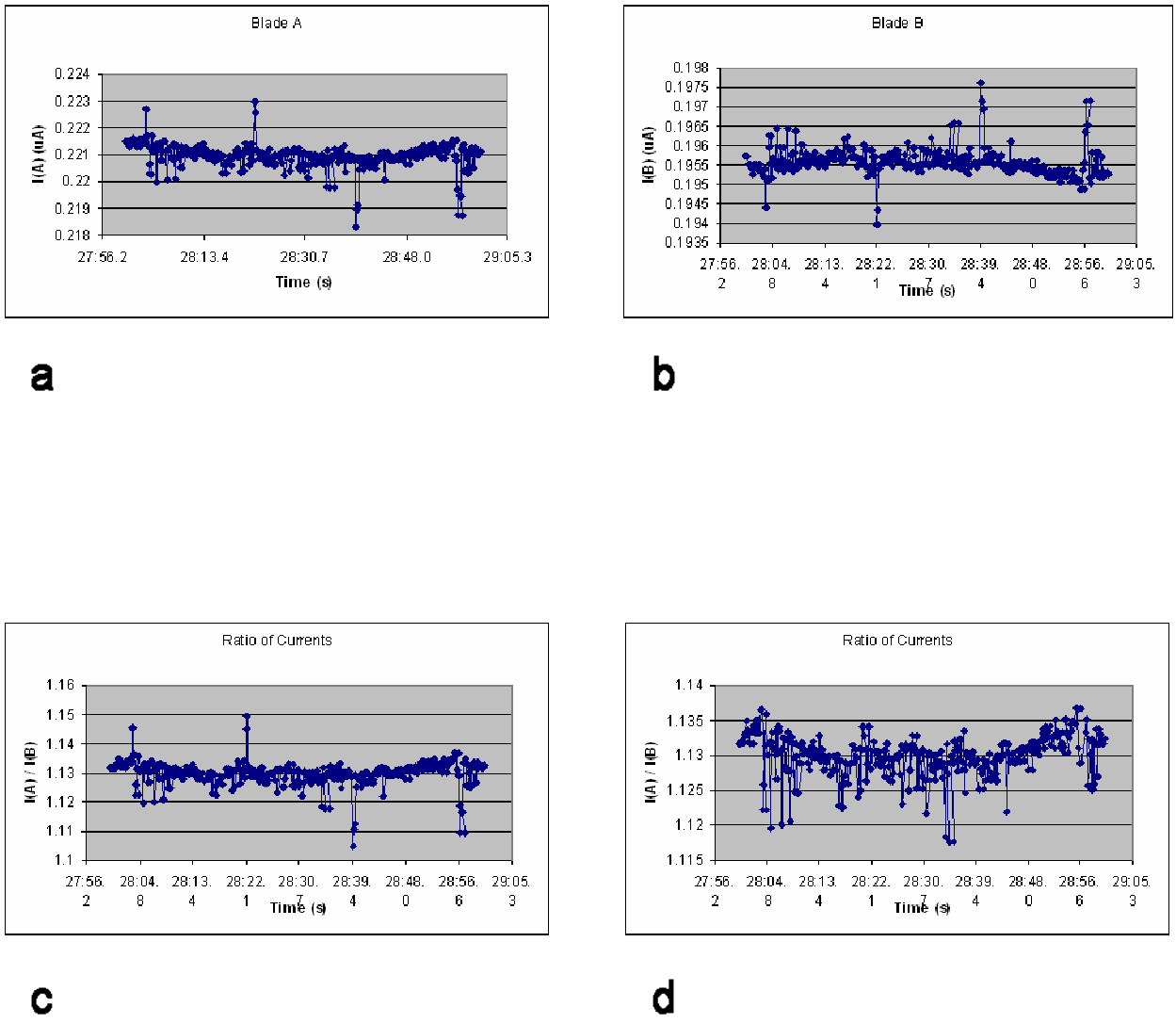

Figure 4.7 Images (a) and (b) show the currents measured from the XSR XBPM. Image (c) shows the ratio of the currents and possible beam motion. Image (d) has outliers removed to calculate the variance of the signal measured.

Table 4.3 Variance calculation results (arb. units) used to determine sampling rate and NPLC for Keithley picoammeter

Test 1: 5 Hz, NPLC 1 Var. Scan 1: 5.39414 x 10-5 Var. Scan 2: 6.27548 x 10-5 Var. Scan 3: 3.92448 x 10-5 AVG Variance: 5.19937 x 10-5	Test 7: 10 Hz, NPLC 1 4.90957 x 10-5 4.46197 x 10-5 5.28559 x 10-5 AVG Variance: 4.88571 x 10-5
Test 2: 5 Hz, NPLC 2 Var. Scan 1: 2.68509 x 10-5 Var. Scan 2: 2.65475 x 10-5 Var. Scan 3: 3.42843 x 10-5 AVG Variance: 2.92276 x 10-5	Test 8: 10 Hz, NPLC 2 3.96674 x 10-5 6.19785 x 10-5 4.76921 x 10-5 AVG Variance: 4.97793 x 10-5
Test 3: 5 Hz, NPLC 3 Var. Scan 1: 2.4905 x 10-5 Var. Scan 2: 3.24773 x 10-5 Var. Scan 3: 4.00462 x 10-5 AVG Variance: 3.24762 x 10-5	Test 9: 10 Hz, NPLC 3 3.77974 x 10-5 1.31362 x 10-5 2.67368 x 10-5 AVG Variance: 2.58901 x 10-5
Test 4: 5 Hz, NPLC 4 Var. Scan 1: 4.16767 x 10-5 Var. Scan 2: 2.20435 x 10-5 Var. Scan 3: 4.74452 x 10-5 AVG Variance: 3.70551 x 10-5	Test 10: 10 Hz, NPLC 4 2.80575 x 10-5 3.37262 x 10-5 4.17964 x 10-5 AVG Variance: 3.45267 x 10-5
Test 5: 5 Hz, NPLC 5 Var. Scan 1: 5.41498 x 10-5 Var. Scan 2: 3.46404 x 10-5 Var. Scan 3: 4.64348 x 10-5 AVG Variance: 4.50750 x 10-5	Test 11: 10 Hz, NPLC 5 8.9507 x 10-6 1.94619 x 10-5 4.12697 x 10-5 AVG Variance: 2.32274 x 10-5
Test 6: 5 Hz, NPLC 6 Var. Scan 1: 1.88573 x 10-5 Var. Scan 2: 4.69928 x 10-5 Var. Scan 3: 2.87283 x 10-5 AVG Variance: 3.15261 x 10-5	Test 12: 10 Hz, NPLC 6 2.85277 x 10-5 5.24935 x 10-5 3.40606 x 10-5 AVG Variance: 3.83606 x 10-5

4.3 XBPM Resolution

4.3.1 XSR Resolution Measurements

Spatial resolution measurements of the XBPM were performed on the XSR beamline during Dec. 10th, 2005 (storage ring current 170 mA). Using the results from section 4.2 both Keithley picoammeters used on the XSR XBPM were set to 10 Hz and 5 NPLC.

For the purpose of this experiment it was assumed that the e-beam was relatively stationary and that the SR was following the nominal design path. Moving the translational stage vertically would thus simulate SR beam motion. With the above assumption in mind the translational stage was moved vertically so that the signal on XBPM blades was nearly equal thus mimicking a centered SR beam. The stage was moved downwards from the "origin" position of 1708 (ADC value on the motor control), to the position of 1683 – a change of approximately 125 μm.

With the XBPM blades centered on the beam the step size for the stepper motor, number of times moved, and pause time were set within the MatLab script "XBPM_scan_AQ_v2", see appendix D. The script allows a Windows desktop computer to control the stepper motor for the XBPM translational stage as well as recording the storage ring current, individual current from the XBPM blades and ADC value giving an indication of the stage/XBPM position. The following MatLab input scheme was used to determine the spatial resolution of the XBPM:

- Initially set the step size at 4, i.e. 4 motor steps per movement, the number of times moved at 200 and the pause time at 1 second.
- Decrease the above parameters by a factor of 2: step size, number of moves and pause time
- Decrease the above parameters again by a factor of 2 – may have to increase number of times moved
- Hold constant the pause time and vary the step size and number of times moved.

The goal of the above procedure is to determine that, when the translational moves by micron or submicron movements, an equivalent change is recorded by the

XBPM blades. A secondary goal is to determine the calibration constant(s) needed to translate the changes in current given by equation 2.4 into a change in linear position.

For each scan, regardless of MatLab initial conditions, a common starting point of the XBPM position was used; in this case the step value that matches with the beam-centered ADC value was chosen. At the end of each scan the translational stage was moved in the opposite direction past the "origin" (ADC value 1683, Step 1500) by 1000 motor steps to overcome any problems due to backlash, i.e. gear or stage slippage. The stage was then moved incrementally in steps of 100 back to the origin.

For a step size of 4 (within the MatLab script), number of times moved 200, and a pause time of 1 second a total of 8 scans were obtained, four of which were chosen for analysis. Four scans were performed for a step size of 2, 100 movements and a pause time of 0.5 seconds. Three of the four scans were kept for analysis. Five scans were performed for a step size of 1, and a pause time of 0.25 seconds with the number of times moved increased to 200 in order to ensure a larger scan range. Four of the five scans were used for analysis. Additionally, three scans were obtained for a step size of 4, 50 movements and a pause time of 1 second. All three scans were used in the analysis. Finally, five scans were performed with a step size of 1, 200 movements and 1 second pause time. Only three of the five scans were used in the analysis. Data not used in the analysis was rejected due to synchrotron beam lose, improper starting point for scans, improper pause time for MatLab script (i.e. 0.1 sec instead of 1 sec), or a "slippage" of data points (data points at the end of the scan being placed next to the beginning data points).

Once the MatLab scans have finished the computer will have recorded the storage ring current, individual blade current(s) and step value. Consider figure 4.8 which is an average of three scans taken when the pause time was held at 1 second, a step size of 4 and the stage only moved 50 times.

To determining the spatial resolution of the XBPM a calibration coefficient is needed so that linear vertical displacements of the SR beam, given by equation 2.4, have an actual positional value. Recall that equation 2.4 is given by

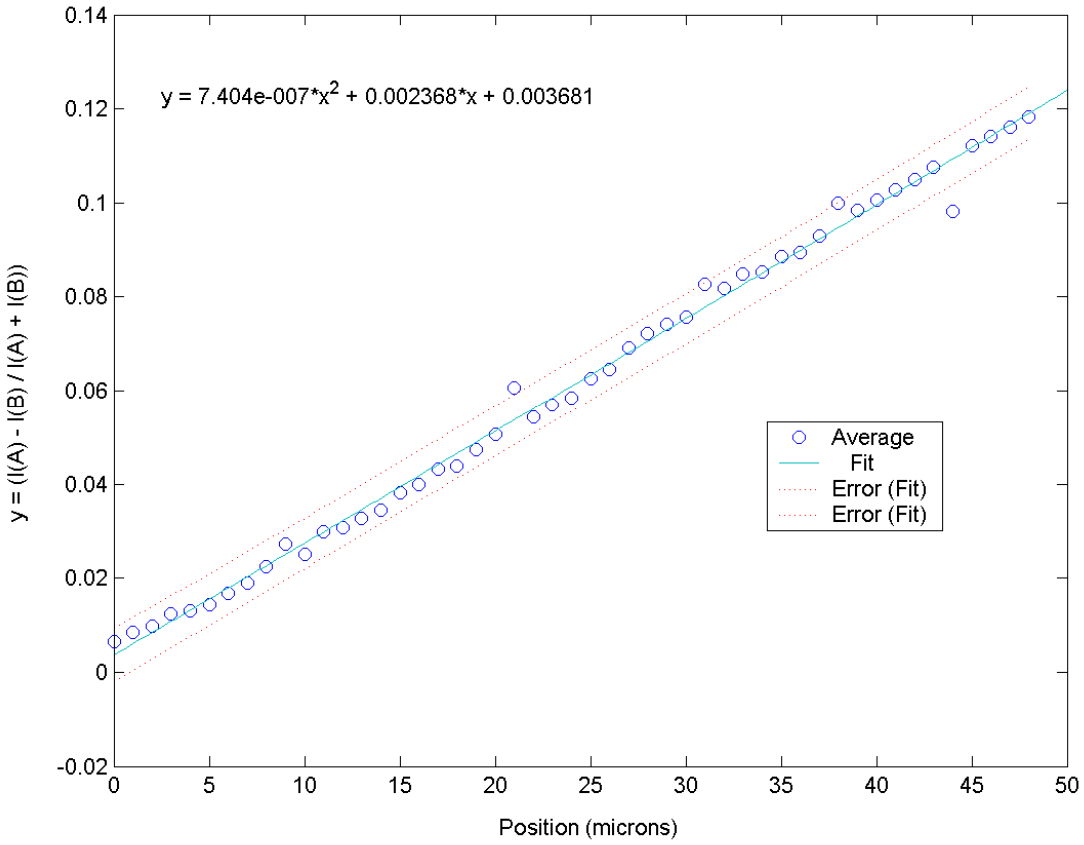

Figure 4.8 Second order polynomial fit to data from group 2. The linear term provides the calibration coefficient for the XBPM. A 2 sigma error bar is plotted for the fit.

$$y = \frac{I(A) - I(B)}{I(A) + I(B)}, \tag{4.1}$$

which, without a calibration coefficient, provides a measure of the relative change in position of the SR beam. By performing a polynomial fit to the data obtained and stored by MatLab it is possible to calculate the coefficient [3]. MatLab is capable of a number of fitting operations up to and including a 10th order polynomial. For the data measured from the XSR XBPM a 2nd order polynomial was used on all the averaged data scans. Refer to figure 4.8 for example and table 4.4 for fit results. Polynomial fits for all data groups presented in Appendix C; figures C.13, 15, 17, 19 and 20. A two sigma error bar is plotted for each fit for ease of visual reference.

Table 4.4 Calibration coefficients for the XSR XBPM

Data Group Number	Slope (1/μm)	Calibration Coefficient (μm)
1	0.002649	377.50
2	0.002368	422.28
3	0.002074	482.28
4	N/A*	N/A*
5	0.002170	460.87
Calibration Coefficient Average = 435.73 μm * MatLab unable to perform a fitting		

Once a polynomial has been fitted to the data it is only a matter of determining the reciprocal of the linear term in order to acquire the calibration coefficient, BD (= Beam Displacement) which is a conversion between equation 4.1 and the beam displacement. For the example provided in figure 4.8 the coefficient is calculated as

$$BD = \frac{1}{m} = \frac{1}{0.002368/\mu\text{m}} = 422.28\mu\text{m}, \tag{4.2}$$

Refer to table 4.4 for XSR calibration coefficient results. Notice that as the linear terms increase in value the reciprocals converge to the value calculated for group 1 (which has the beginnings of a Gaussian profile). Cross-section scans of the entire SR beam showing the Gaussian profile would increase the accuracy of the calibration coefficient BD.

Inserting the average value for the calibration coefficient into equation 2.4 (and 4.1), it is possible to determine the amount of vertical change of the SR beam. Using the values from the initial and final data points of figure 4.8, the vertical change in position is calculated to be

$$\Delta y = BD\left(y_f - y_i\right) = 435.73\,\mu\text{m}\left(0.1184 - 0.006436\right) = 48.79\mu\text{m}, \tag{4.3}$$

Recall that moving the XBPM is similar to motion of the SR beam. From figure 4.8 the translational stage moved a total distance of 49 microns which is only 0.5% different than the displacement calculated in equation 4.3. Table 4.5 lists the estimated

Table 4.5 Calculated SR beam displacement

Data Group	Estimated Displacement (+/- 0.5 μm)	Calculated Displacement (μm)
1	199	199.82
2	49	48.79
3	24	26.07
4	34	13.04
5	49	49.35

displacements, determined from translational stage calibration, and calculated displacements determined by equation 4.1 and the beam displacement coefficient BD.

The calibration coefficient BD also provides a means to confirm that the translational stage is stepping with the sizes estimated during the stage calibration; refer to table 4.1. From figure 4.8 the spacing separating each data point is an estimated 1 micron. By using equation 4.3 and points selected from figure 4.9 the separation for points A and B (estimated separation 1 micron) is calculated as

$$\Delta y = BD\left(y_b - y_a\right) = 435.73\,\mu\text{m}\left(0.10062 - 0.098354\right) = 0.98736\mu\text{m}\ , \tag{4.4}$$

and points A and C (estimated separation 4 microns) as

$$\Delta y = BD\left(y_c - y_a\right) = 435.73\,\mu\text{m}\left(0.1075 - 0.098354\right) = 3.985\mu\text{m}\ , \tag{4.5}$$

The percentage difference for points A and B and points A and C is 1.3 % and 0.4 %, respectively. Table 4.6 lists estimated and calculated separation spacing for each data group.

From table 4.6 data groups 1 and 2 indicate XBPM spatial resolution on the order of 1 micron. Following the recommendations of section 5.2 sub-micron spatial resolution should be achieved.

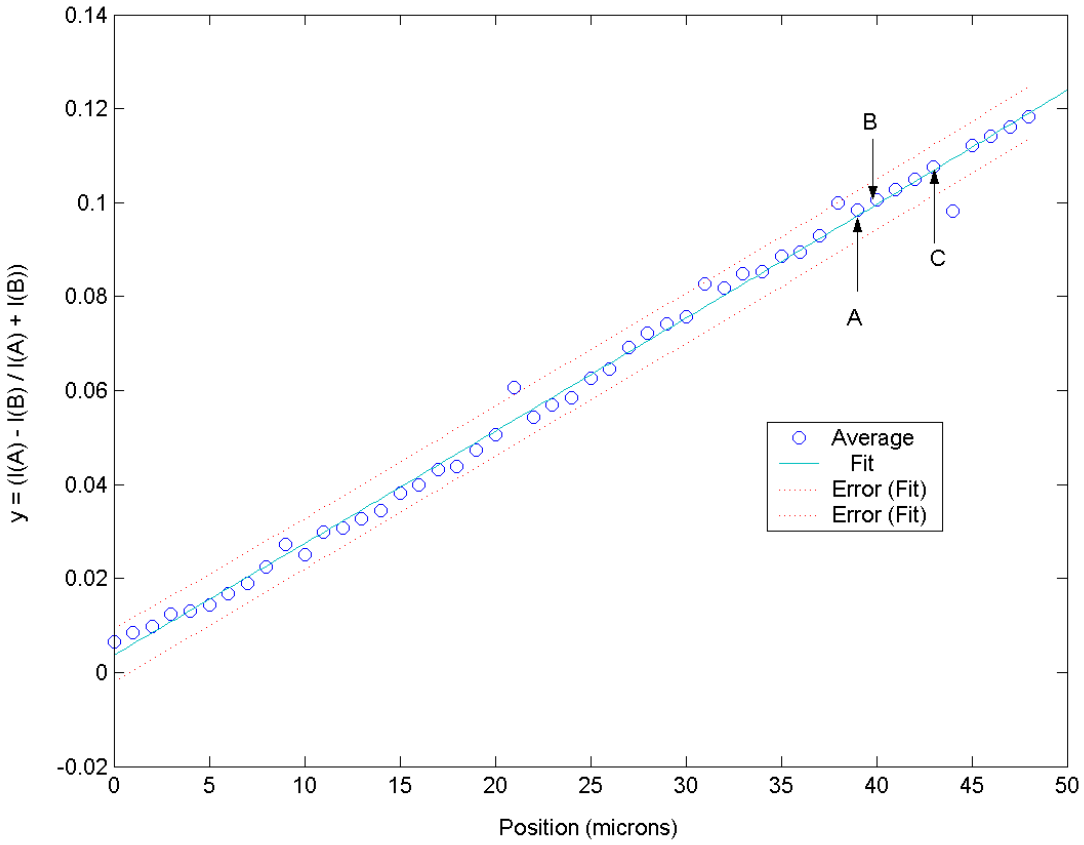

Figure 4.9 Confirmation of translational stage stepping size. The estimated separation of points A and B and points A and C is 1 and 4 microns, respectively. Calculated separation between points A and B and A and C is 0.987 and 3.98 microns, respectively.

Table 4.6 Data Point Spacing

Data Group	Estimated Spacing (μm)	Calculated Spacing (μm)
1	1	0.7364
2	1	0.9874
3	0.5	0.9978*
4	0.25	0.2214**
5	0.25	0.4562*

* Spacing between three data points. ** Not representative of entire data set

4.3.2 HXMA Resolution Measurements

On May 24th, 2006 a preliminary set of scans were obtained from the HXMA XBPM (storage ring current 154 mA). The scans were performed subsequent to the completion of the software control work briefly mentioned in section 4.1.

Two types of measurements were performed each comprised of 5 individual scans: a static measurement in which the XBPM was not moved with the signal sampled versus time, and a dynamic measurement in which the XBPM was moved via the translational stage. The static scans provide a "snap-shot" of SR beam motion while also indicating that the XBPM is sensitive to SR fluctuations without movement of the translational stages. Following section 4.3.1, the moving scans are used to determine the calibration coefficient of for the XBPM which in turn is used for calculating the change in beam position.

For each of the static and dynamic scans the Keithley picoammeters were set to 10 Hz and 2 NPLC. A lower NPLC was used due to the timing feature added to the meter interface which slightly increases the processing time of the meter.

Using a 2nd order polynomial fit to the averaged data of figure 4.10, the calibration coefficient BD is calculated as

$$BD = \frac{1}{m} = \frac{1}{0.001985/\mu\text{m}} = 503.78\mu\text{m} \quad , \tag{4.6}$$

Inserting BD into equation 2.4 or 4.1, and using the initial and final data points of figure 4.10, the calculated change in vertical position is

$$\Delta y = BD\left(y_f - y_i\right) = 503.78\,\mu\text{m}\left(0.824 - 1.01\right) = 93.70\mu\text{m} \quad , \tag{4.7}$$

The translational stage moved a total of 100 microns which is ~6% different than the displacement calculated above.

Using equation 4.7 and the points selected from figure 4.11, averaged static scan, the possible displacement of beam motion is calculated to be

$$\Delta y = BD\left(y_f - y_i\right) = 503.78\,\mu\text{m}\left(0.5285 - 0.528\right) = 0.252\mu\text{m} \quad , \tag{4.8}$$

Result 4.8 is preliminary at time of writing.

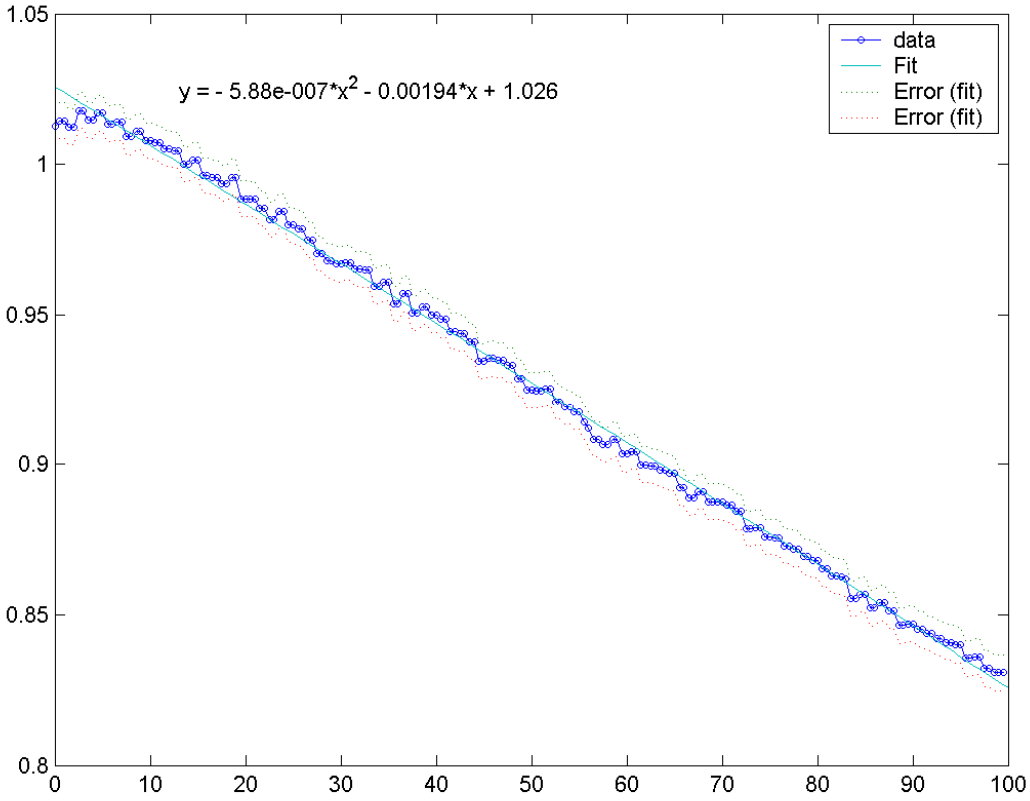

Figure 4.10 Second order polynomial fit to data from the HXMA XBPM. The linear term provides the calibration coefficient for the XBPM. A 2 sigma error bar is plotted for the fit.

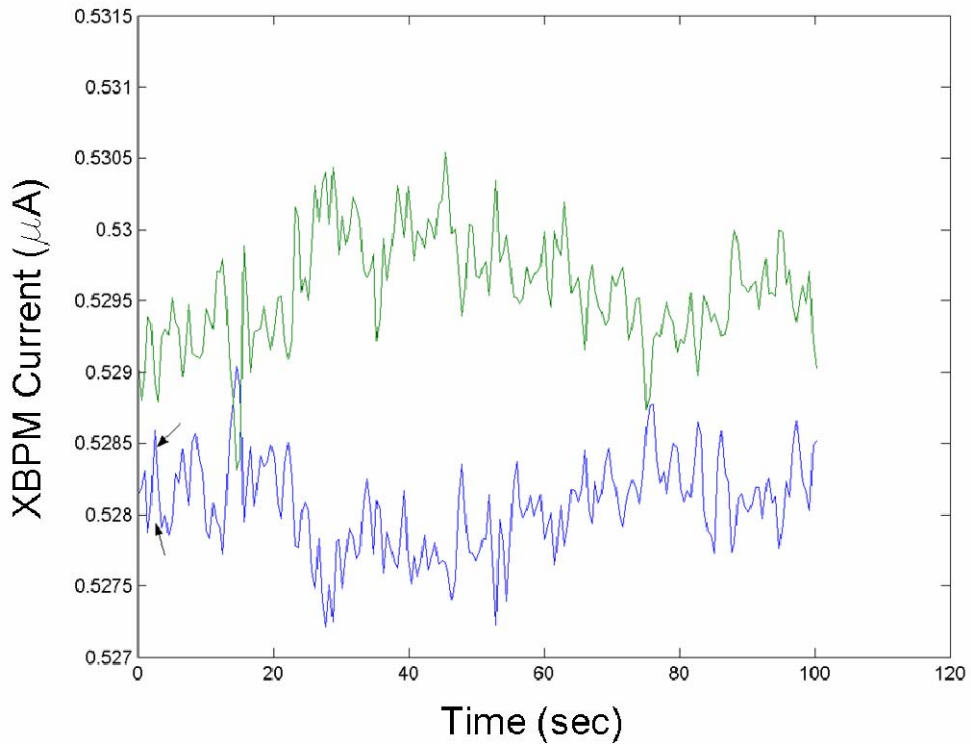

Figure 4.11 Static scan of the HXMA XBPM. Anti-correlation of the individual signals is indicative of SR beam movement. Signal measured from the top blade (blue, bottom) is used in equation 4.8 indicated by the arrows.

4.3.3 Error Estimate

Added to the spatial resolution of the XBPM are the errors due to the thermal expansion of the materials used in the XBPM and the beamline, OFHC copper and stainless steel, and the errors due to alignment of beamline components. The theodolite used for surveying all the equipment throughout the CLS facility has an accuracy of between 100 – 200 microns. To determine the error contribution from the thermal expansion of materials the standard formula is used:

$$\Delta L = \alpha L_0 \Delta T \quad , \tag{4.9}$$

where ΔL = amount of expansion,

α = coefficient of linear expansion,

L_0 = original length,

ΔT = temperature change.

For OFHC copper the linear coefficient of thermal expansion is 18.23 μm/m/^{0}C at 27^{0}C, while for stainless steel the value 17.2 μm/m/^{0}C for 0 – 100 ^{0}C is used. Typically the change in temperature of cooling water is maintained between 0.5 – 4 ^{0}C for the CLS facility. For the copper module used in the XSR XBPM, height of 42 mm (as measured from the base of the blade holder to midpoint of aperture) and water reservoir height 80 mm, the amount of expansion given by equation 4.9 is,

$$\Delta L = (18.23\mu m/m/^0C)(42mm + 80mm)(4^0 C) = 3.1\mu m + 5.8\mu m \approx 9\mu m \ .$$

Similarly for the stainless steel vacuum chamber which is joined to the copper water reservoir, height 103 mm as measured from the base of the chamber to steel-copper join, the amount of thermal expansion is calculated to be ~7 microns.

Totalling all the above results in an error of approximately +/- 16 microns should be applied to positioning accuracy over an extended time period.

Finally, from figure C.12, it can be seen that as the translational stage moves vertically up or down there is a horizontal displacement of +/- 30 microns, coupled to the 0.5 micron accuracy of the encoders, and a survey error of 200 microns resulting in a 202 micron error affecting the fiducial placement of the XBPM with respect to nominal position.

4.4 YAG Image Acquisition

As stated in section 3.3, the YAG imaging equipment was originally intended to provide an independent means of validating the readings from the XBPMs. For the reasons mentioned in section 3.3 the system was modified to that of a simple image acquisition platform to convert the x-rays into visible fluorescence. With this modification the procedure for acquiring images becomes greatly simplified.

Refer to appendix D and the Spiricon manual, Ref. 57, for the procedure used to acquire visible fluorescence of SR from the YAG crystal.

The visible fluorescence images were acquired on September 19th, 2005, during a scheduled commissioning night for the CMCF beamline. Storage ring current was

initially 7.1 mA. The undulator was moved from maximum gap, ~35 mm, to a gap of 12 mm at which point undulator radiation became visible on the YAG crystal. The undulator was held at the 12 mm gap for several minutes due to out-gassing from the crystal and to allow the ion pumps to return the vacuum to optimal conditions. (Vacuum changed from mid 10^{-8} Torr to high 10^{-8} Torr but did not trip the storage ring). The gap was then closed from 12 mm to 10 mm at which point it appeared that the SR moved out of the aperture. Orbit correction was turned off and a 100 mm offset entered into the accelerator steering controls. The undulator was then moved from 10 mm to 12 mm several times to see if any difference was observed. When no change was noted, the offset was removed and the orbit correction turned back on. It was then decided to move the undulator to a 9.5 mm gap at which point the undulator radiation re-appeared. The undulator was closed to a 9 mm gap for several minutes and then withdrawn to the maximum gap position. Figures 4.12 to 4.16 illustrate the above sequence.

From figure 4.15, which displays the simulated CMCF spectrum, the images obtained at a 10 mm gap resemble the spatial distribution of SR observed on the even harmonics.

If the fixed mask to which the XBPM is attached had not been pulled out of alignment due to the photon shutter, refer to section 4.2, it would have been possible to corroborate the YAG images to the signals measured on the XBPM. For instance, from the lower image of figure 4.12 the undulator spot is present in the left portion of the visible aperture. A corresponding increase in signal on the outboard blades of the XBPM would have been an indication that the XBPM module works as designed – provided that the fixed mask was not out of alignment and that the synchrotron radiation was nominal for the CMCF beamline. Another beam detecting or imaging system further downstream would be needed to determine if the synchrotron radiation beam is following the optimal trajectory and angle.

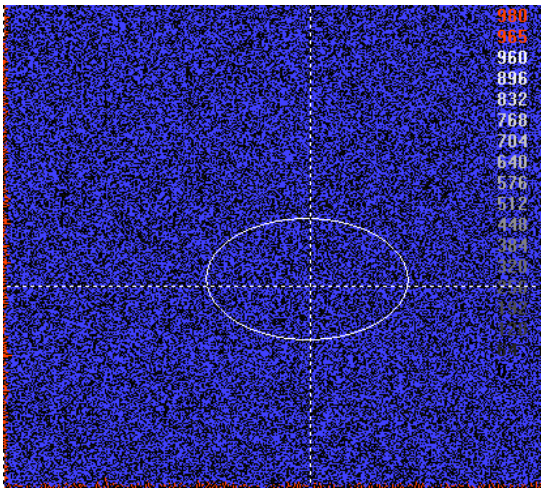

Figure 4.12 Dark current image of the YAG crystal. Image was acquired with the user controlled photon shutter on CMCF closed.

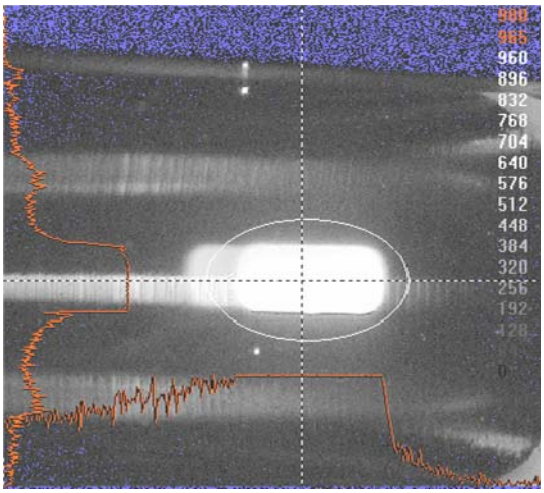

Figure 4.13 Bend magnet radiation imaged on the YAG crystal.

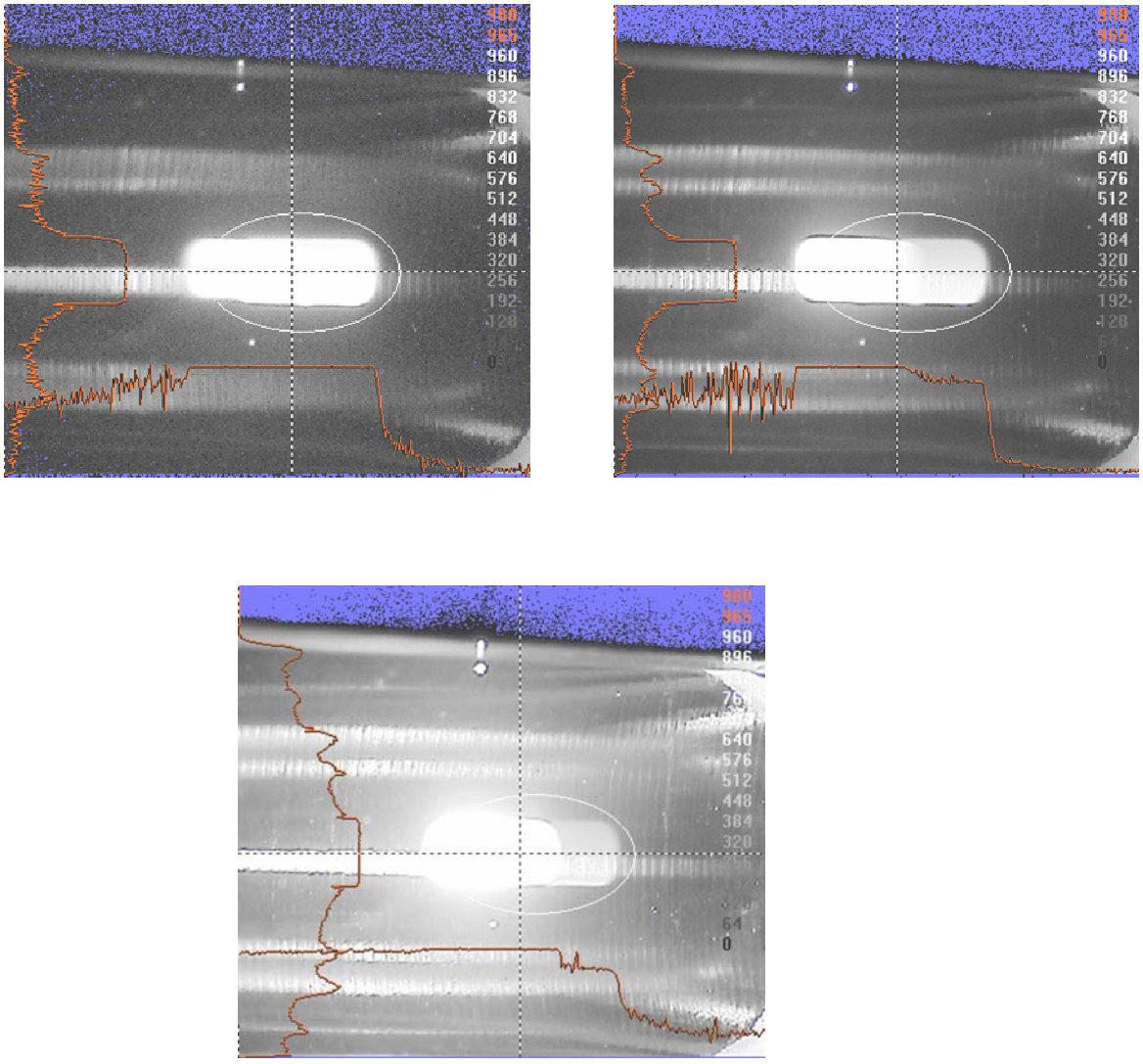

Figure 4.14 Image sequence of the CMCF undulator closing from 35 mm to 12 mm. Top left image indicates undulator radiation as evident by near equal intensities. As the undulator moves closer to 12 mm a definite "spot" is starting to appear, top right image. Lower image displays the undulator radiation spot for a 12 mm gap. Unfortunately there is significant intensity blooming on the YAG crystal to prevent clearly defining the spot shape.

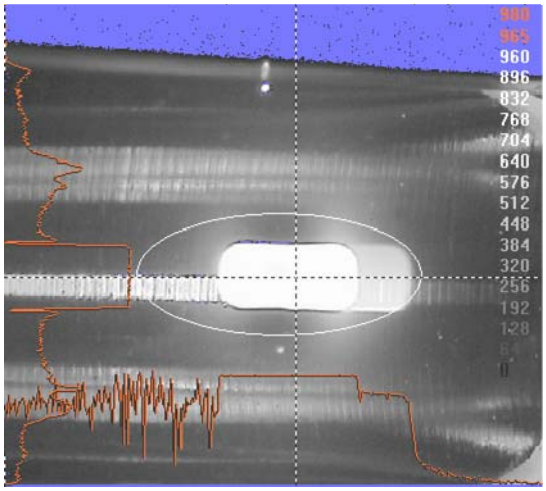

Figure 4.15 Undulator moved to 10 mm gap thus changing the harmonic energy imaged by the YAG crystal.

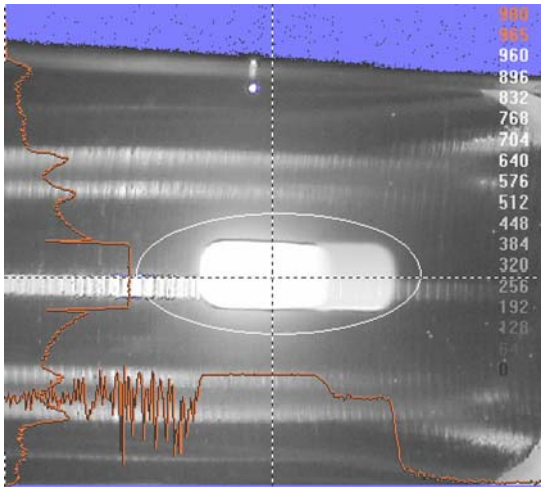

Figure 4.16 Image of the undulator radiation for a gap size of 9 mm.

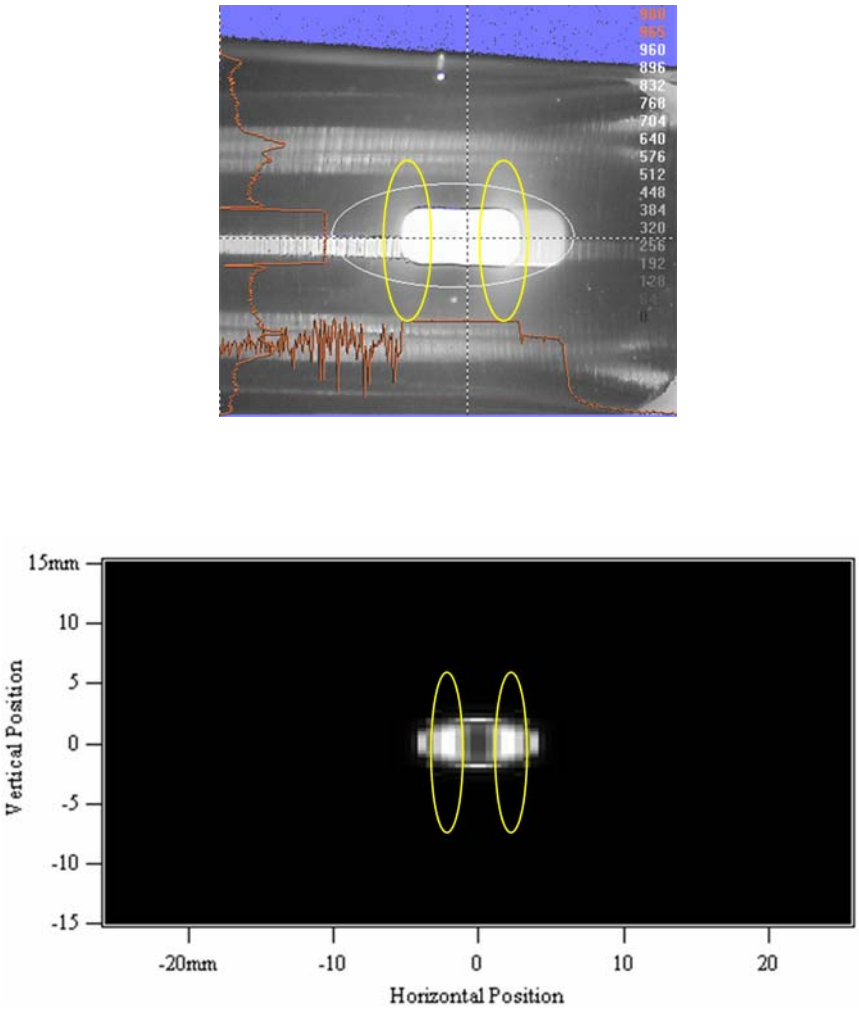

Figure 4.17 Comparison of the spot characteristics of the 10 mm undulator spot to simulations computed by SRW. The "wisps", highlighted by the yellow ovals, are similar to spatial distributions of photon energy 4.1 keV. Other possible photon energies for the distribution are 6.1, 8.1, 10.1 and 12.1 keV.

5 CONCLUDING REMARKS

5.1 Summary and Discussion

The primary purpose of this thesis was to determine the spatial resolution of the three front end XBPMs installed on separate beamlines within the CLS facility (HXMA, CMCF and XSR), and is estimated at 1 μm. In terms of the accuracy of the beam position determination over an extended period of time, the possible uncertainty is +/- 16 μm due to the temperature drifting factors considered section 4.3.3. Prior to determining the spatial resolution of the XBPMs two tasks needed to be accomplished: 1) the calibration of the translational stages, i.e. the resolution of stage motion, and 2) establishment of a reference point for incoming synchrotron radiation.

The latter task, while not necessary for determining the spatial resolution of the XBPM, is needed to establish the fiducial reference (origin) from which measurements will be acquired. This origin provides the basis of determining if the synchrotron radiation is in the correct vertical and horizontal position to be utilized by the scientific end station. Multiple engineering surveys using a laser interferometric theodolite ensured that the vacuum chamber or fixed masks that house the XBPMs were centered on the nominal synchrotron beam trajectory. Potentiometers attached to the translational stages, which are mounted the fixed masks (or vacuum chamber), provide a unique value for the reference point (refer to table 4.1).

Once the fiducial reference was established the resolution of the translational stages was determined. Two linear encoders of resolution 0.5 μm were orthogonally mounted to record vertical and horizontal displacements. This enabled the amount of horizontal wobble to be measured as the stage moved vertically and vice versa. Resolution of the translational stages was determined by moving the stage from one limit of motion to the opposite limit and then over a small range centered on the origin. Due to the high facility demand for the encoders the only limit-to-limit scan was performed for

the HXMA beamline: the smaller scan range was completed on all three beamlines. For each beamline the relation between encoder value, step position and potentiometer (ADC value) were obtained in order to determine the resolution of the stage motion. From the relations it was calculated that the resolution of the translational stage is approximately 0.25 μm, with the resolution of the potentiometers approximately 5 μm. During the calibration tests indications of problems with the CMCF translational stages became evident but the full problem was not diagnosed until prior to XBPM spatial resolution measurements.

As explained in section 4.1 and Appendix B the CMCF translational stage was repeatedly pulled out of alignment due to the opening and closing of the downstream photon shutter – both pieces of equipment are joined by a connecting bellows. The result was significant internal structural loosening of the translational stage. As a consequence no XBPM scans were possible on the CMCF beamline.

Also, due to software control issues, no in depth systematic scans of the XBPM were taken on the HXMA beamline. While the operation of the XBPM does not interfere with the workings of the HXMA beamline it was advised to temporarily halt proceedings until control issues were resolved. Fortunately no mechanical or software problems affected the XSR beamline. A quick set of preliminary scans were performed once the control problems were resolved but a detailed study of the HXMA XBPM still needs to be performed.

To perform the spatial resolution measurements two quantities had to be determined: the sampling rate of the Keithley picoammeters and the number of power line cycles of the meter. Initially the picoammeters were limited to a sampling rate of only 1 Hz with a power line cycle range between 1 – 6 (the number of power line cycles effects the integration time of the meter). With software upgrades implemented by the Controls and Instrumentation group of the CLS the sampling rate of the picoammeter was increased up to and including 10 Hz, with a power line cycle range of 1 – 60. Currently at the CLS the range of experimental times is from a few seconds to several minutes, depending on the experiment, thus indicating that a sampling rate of 5 or 10 Hz is more than adequate. To determine the number of power line cycles to be used, and thus set the integration time of the meter, combinations of sampling rate and power line cycle were

tested, i.e. 5 Hz and 3 cycles or 10 Hz and 1 cycle, etc. For each of the combinations the variance was calculated with the smaller variance value being chosen for the picoammeter settings provided that the XBPM measurement was recorded by the CLS data archive. If the measurement was null, indicated by "N/A" in the archive, then the next combination of sampling rate and power line cycle was set. For the spatial resolution measurements the sampling rate was set at 10 Hz with the number of power line cycles set at 5. Subsequent software upgrades to the picoammeters would necessitate revisiting the above procedure for future use.

To determine the spatial resolution of the XBPM on the XSR beamline a number of scans were performed. Using a MatLab script that recorded the storage ring current, potentiometer reading (ADC value) and XBPM blade currents, the script controlled the motion of the translational stages connected to the XBPMs. The script would move the motorized linear stage through a pre-set number of motor steps using a step size of 1, 0.5 or 0.25 μm. From the 25 data sets collected 16 were used to determine that the XBPM is able to distinguish motion on the sub-micron level. The data sets were also used to calculate the calibration coefficient of the XBPM so that a quantitative value could be assigned to changes in beam position.

The secondary purpose of this thesis project was the construction of an imaging system. Comprised of a YAG crystal to convert the x-rays into visible fluorescence, the visible light is captured by a commercially available image acquisition program for two purposes: to qualitatively measure the amount of ID and background radiation propagating down a beamline, and to corroborate the positional measurements made by the XBPM. Due to concerns about possible crystal failure and contamination of beamline equipment the imaging system was installed only in the CMCF beamline which has several tens of meters of equipment free beam pipe. Unfortunately due to problems with the CMCF photon shutter, which affected the XBPM, it was not possible to corroborate visible synchrotron images to photon beam position determined by the XBPM. Fortunately several thousand images were acquired of the CMCF undulator in operation at a storage ring current of 7 mA from maximum gap, ~ 35 mm, down to a gap of 9 mm (minimum gap is 5.6 mm). The captured images indicate that a significant amount of background synchrotron radiation coming from the bending magnets is propagating down

the CMCF beamline; beamline scientists are working to understand and remedy the situation.

5.2 Recommendations

During the course of the project a number of problems were encountered that prevented experimental investigation on certain beamlines. While some of the problems are beamline specific others potentially apply to all the XBPMs and need to be addressed. The following list of recommendations outlines work that could aid in improving the performance of the XBPMS and in understanding the basic physical operation of the XBPM:

- Mechanical vibration and temperature fluxtuation tests for all the XBPMs Need to determine how much of the signal is due to mechanical or thermal noise.
- Problems with the translational stages need to be resolved (Appendix B). Either replace with better stages or use stop-gap measures for now.
- Develop a control interface that will move the XBPM stages and record the storage ring current, XBPM blade currents, time stamp, and ADC or encoder position. This avoids the discontinuities that arise between MatLab and the CLS archive.
- Put encoders on the translational stages or increase the number of vertical potentiometers to 2, one on each side. Encoders would be better in that an actual change in position could be measured.
- Map out the complete vertical (and horizontal) distribution of the SR beam on each beamline. This will enable the response transfer function (the linear range between max and min XBPM photocurrent values), sensitivity, spatial resolution and beam profile to be determined at the same time (as well as the calibration coefficients).
- Develop a look up table of BM background for the HXMA and CMCF beamlines. One needs these values to correct for position offset of the incoming synchrotron radiation beam.

- Determine if the calibration coefficients are the same for different operating currents…may need a look up table if different.
- Perform frequency analysis of signal measured off the XBPM blades. This may indicate spatial instabilities within the beam.
- Tie in the measurements from the XBPMs to existing BPMs in the beamlines. This way visiting scientists will be able to determine the position and angle of the SR beam.
- Begin study of duplex ID lines and how to determine SR beam position with an XBPM (i.e. is a modification required or completely new design).
- For future ultra-fast experiments may need to increase the sampling speed of XBPM electronics equipment. This may require a completely new set of meters and cables to measure and read the data.
- Possible automated compendium that includes date, time of year, current weather conditions, and any beam steering to accompany data acquired from the XBPMs.
- Determine how much of the XBPM blade is actually used in the detection of the synchrotron radiation. Is it the whole blade, leading edge, top of the blade or some combination? How much current generation is produced by the blade sides? Could lead to different designs depending on where the photoelectrons are generated on the blade.
- It was proposed that the photoelectrons were generated by both the photoelectric effect and the Auger effect. In what proportions does each of the effects contribute to the whole of the photocurrent measured? Would a systematic study of individual frequencies from VUV to soft x-ray provide a qualitative measure of each effects proportion to the whole current? Further, could this lead to an equation to estimate the signal generated on a XBPM for any given beamline?
- For bending magnet beamlines is it necessary to have the XBPM blades in the center of the vacuum chamber. Could the blades be offset to one side? What affect would this have on photocurrent generation and on vertical beam positioning?

List of References

1. Billing, M. G., Beam Position Monitors for Storage Rings. Nucl. Instrum. and Meth. A, 266 (1988), pp. 144-154.
2. Fajardo, P. and Ferrer, S., Ultrahigh-vacuum-compatible position and shape monitor for high brilliance synchrotron radiation beams. Rev. Sci. Instrum. 66 (1995), pp. 1882-1884.
3. Alkire, R. W. et al., The X8C dual wire beam position monitor. Nucl. Instrum. and Meth. A 350 (1994), pp. 13-16.
4. Heald, S. M., A simple Photoelectron X-ray Beam Position Monitor for Synchrotron Radiation. Nucl. Instru. and Meth. A 246 (1986), pp. 411-412.
5. Lankosz, M. and Sieber, J., A simple microbeam profiling technique for x-ray optics. Rev. Sci. Instrum. 71 (2000), pp. 2640-2643.
6. Koyama, A., Sasaki, S. and Ishikawa T., Closed feedback system on the vertical beam position. Rev. Sci. Instrum. 60 (1989), pp. 1953-1956.
7. Schildkamp W. and Pradervand, C., Position monitor and readout electronics for undulator and focused bending magnet beamlines. Rev. Sci. Instrum. 66 (1995), pp. 1956-1959.
8. Bergonzo, P. et al., Diamond-based semi-transparent beam-position monitor for synchrotron radiation applications. J. Synchrotron Rad. 6 (1999), pp. 1-5.
9. Sakae, H. et al., Diamond Beam-Position Monitor for Undulator Radiation and Tests at the Tristan Super Light Facility. J. Synchrotron Rad. 4 (1997), pp. 204-209.
10. Shu, D., Barraza, J. and Kuzay, T. M., Tests of the APS X-ray Transmitting Beam Position Monitors at ESRF. Proceedings of the 1997 Particle Accelerator Conference, 2 (1997), pp. 2210 - 2212

11. Shu, D. et al., Synthetic diamond-based position-sensitive photoconductive detector for the Advanced Photon Source. J. Synchrotron Rad. 5 (1998), pp. 636-638.

12. Shu, D. et al., Smart X-ray beam position monitor system using artificial-intelligence for the Advanced Photon Source insertion-device beamlines. J. Synchrotron Rad. 5 (1998), pp. 632-635.

13. Galimberti, A. et al., A new detector for photon beam position monitoring designed for synchrotron radiation beamlines. Nucl. Instrum. and Meth. A 477 (2002), pp. 317-322.

14. Shu, D. et al., The APS X-ray undulator photon beam position monitor and tests at CHESS and NSLS. Nucl. Instrum. and Meth. A 319 (1992), pp 56-62.

15. Cerino, J. A., Rabedeau, T. and Bowen, W., Photon beam position monitor for SSRL Beamline 9. Rev. Sci. Instrum. 66 (1995), pp. 1646-1647.

16. Stefan, P. M., Siddons, D.P. and Hastings, J. B., A New Beam Position Monitor for X-ray Synchrotron Radiation Facilities. Nucl. Instrum. and Meth A 255 (1987), pp. 598-602.

17. Gauthier, C. et al., Modulated detection of multibeam dichroism using photodiodes. Physica B 208-209 (1995), pp. 232-234.

18. Alkire, R. W. and Rotella, F. J., An Incident-Beam Monitor for Use in Protein Crystallography at a Synchrotron Source. J. Appl. Cryst. 30 (1997), pp. 327-332.

19. Galimberti, A. et al., First results of the novel photon beam position monitor for undulator beamlines of Elettra. Nucl. Instrum. and Meth. A 467-468 (2001), pp. 221-225.

20. Mortazavi, P. et al., High Flux Photon Beam Monitor. Nucl. Instrum. and Meth. A 246 (1986), pp. 389-393.

21. Johnson, E. D. and Oversluizen, T., Compact high flux photon beam position monitor. Rev. Sci. Instrum. 60 (1989), pp. 1947-1950.

22. Warwick, T. et al., Prototype photon position monitors for undulator beams at the Advanced Light Source. Rev. Sci. Instrum. 63 (1992), pp. 550-553.

23. Warwick, T. et al., Performance of photon position monitors and stability of undulator beams at the advanced light source. Rev. Sci. Instrum. 68 (1995), pp. 1984-1986.

24. Shu, D. et al., The Advanced Photon Source X-ray transmitting beam-position-monitor tests at the national synchrotron light source X-25 beamline. Nucl. Instrum. and Meth A 347 (1994), pp. 577-580.

25. Decker, G. and Singh, O., Method for reducing x-ray background signals from insertion device x-ray beam position monitors. Physical Review Special Topics – Accelerators and Beams, 2 (1999), pp. 112801-1 – 112801-10.

26. Shu, D. et al., Design of an undulator white beam profiler and test results on the Advanced Photon Source beamline (abstract). Rev. Sci. Instrum. 73 (2002), pp. 1587.

27. Aoyagi, H., Kudo, T. and Kitamura, H., Blade-type X-ray beam position monitors for Spring-8 undulator beamlines. Nucl. Instrum. and Meth. A 467-468, (2001), pp. 252-255.

28. Sharma, S. and Woodle, M., Thermal Deformations in a High Flux Beam Position Monitor. Nucl. Instrum. and Meth. A 266 (1988), pp. 513-516.

29. Dallin, L.O., Synchrotron Light Source Magnets. CLS Design Note 5.2.31.2 Rev. 0, 2001-February-11.

30. Lowe, D., CLS Storage Ring Dipole Specification. CLS Magnet Specification CLS31-002 Rev.0, 1999-December-1.

31. Grochulski, P., CMCF 08ID-1 Preliminary Design Report. CLS Design Note 6.2.77.2 Rev. 0, 2002-April-3.

32. Jiang, D.T. and Sheng, W., CLS 06-ID-1 XAFS Beamline Preliminary Design Report. CLS Design Note 6.2.78.2 rev. 0, 2003-February-28.

33. Blomqvist, I., Magnetic Design of a 20 mm hybrid Undulator for CLS. CLS Design Note 6.2.25.4 Rev.0, 2003a-January-16.

34. Blomqvist, I., Magnetic Design of a Super Conducting Wiggler for CLS. CLS Design Note 6.2.25.5 Rev. 0, 2003b-July-18.

35. SRCalc v.1.3.5, Reininger, R., 2001-2002, and SRW v 3.5, Chubar, O. and Elleaume, P., 1997-2001.

36. Dejus, R.J. et al., Undulator A characteristics and Specifications: Enhanced Capabilities. ANL/APS/TB-17, 1994.

37. Chen, J. R. et al., A synchrotron radiation beam-position monitor at the Taiwan Light Source. J. Synchrotron Rad. 5 (1998), pp. 621-623.

38. Hahn, U. et al., Beam-position monitors in the X-ray undulator beamline at PETRA. J. Synchrotron Rad. 5 (1998), pp. 627-629.

39. Schulze-Briese, C. et al., A CVD-diamond based beam profile monitor for undulator radiation. Nucl. Instrum. and Meth. A 467-468 (2001), pp. 230-234.

40. Shu, D., Panakkal, K.J. and Kuzay, T.M., CVD-Diamond-Based position-Sensitive Detector Test with Electron Beam from a Rhodotron Accelerator. Proceedings of the 2001 Particle Accelerator Conference, 2 (2001), pp. 2435 - 37

41. Galbiati, A. et al., Characterisation of a coplanar CVD diamond radiation detector. Nucl. Instrum. and Meth. A 466 (2001), pp. 52-57.

42. Franklin, M. et al., Development of diamond radiation detectors for SSC and LHC. Nucl. Instrum. and Meth. A 315 (1992), pp. 39-42.

43. Kania, D.R. et al., Diamond radiation detectors. Diamond and related Materials, 2 (1993), pp. 1012-1019.

44. Manfredotti, C. et al., CVD diamond tips as X-ray detectors. Diamond and Related Materials 7 (1998), pp. 523-527.

45. Shu, D., 2004 private communication.

46. Hecht, E., Optics, 2nd ed., (Addison Wesley, Massachusetts, 1987), p. 541.

47. Earle, G.D. et al., A novel empirical study of the photoelectric effect in thin gold films. Am. J. Phys. 71 (2003), pp. 766-769.

48. Powell, R. A., Photoelectric effect: Back to basics. Am. J. Phys. 46 (1978), p. 1046 – 1051.

49. Farkas, Gy. et al., Linear surface photoelectric effect of gold in intense laser field as a possible high-current electron source. J. Appl. Phys. 62 (1987), p. 4545 – 4547.

50. Carlson, T. A., Photoelectron and Auger Spectroscopy. New York: Plenum Press, 1975. Chapter 6.

51. Ebril, A., et al., Total-electron-yield current measurements for near-surface extended x-ray-absorption fine structure. Phys. Rev. B, 37 (1988), p. 2450 – 2464.

52. Nian, H. L. T., et al., Thermal buckling parametric analysis for a diamond disk for a x-ray beamline at the Advanced Photon Source. Rev. Sci. Instrum. 67, (1996), (on CD).

53. Nian, H. L. T., Kuzay, T. M., Closed-form solutions for a disk, a filter, and a window for an x-ray beamline at the Advanced Photon Source. Rev. Sci. Instrum. 67, (1996), (on CD).

54. Phillips camera manual, model number: LTC0335/60

55. Edmund catalogue and "Imaging case study" on the Edmund Optics website, www.edmundoptics.com/techSupport/DisplayArticle.cfm?articleid=301.

56. Bergstrom, J., Facility Diagnostic Beamline Preliminary Design Report. CLS Design Note 6.2.79.1 Rev. 1 2002-Aug-01.

57. Spiricon Operator's Manual, version 4.xx, Laser Beam Analyzer. Doc. No. 10654-001, Rev. 4.00.

58. Jopson et al., M-shell Fluorescence Yields of Bismuth, Lead, Gold and Osmium, Phys. Rev. 137 (1965), 1353-1357.

59. Handbook of Mathematical Functions, Abramowitz, M., Stegun, I.A. ed., 1965.

APPENDIX A: CALCULATIONS

Photocurrent Calculations

Calculation of the secondary electron current follows the work of Ebril et al., Ref. 51. The contribution to the secondary-electron-yield current per Auger electron created at depth x_0 with range R for a homogeneous planar sample is based on five key assumptions:

1. The total-electron-yield current for photon energies $E > E_0$ consists mainly of secondary electrons excited by Auger electrons.
2. Through inelastic scattering and collision cascade processes, Auger electrons of range R create secondary electrons uniformly throughout the volume of a sphere of radius r centered on the source of the Auger electrons, figure 2.3
3. The velocity distribution for secondary electrons is isotropic, and the escape probability for secondary electrons created a distance x away from the free surface is given by

$$P(x) = \frac{1}{2}\left[e^{-\beta x} - \alpha x E_1(\beta x)\right], \tag{A.1}$$

where $E_1(x)$ is the exponential integral

$$E_1(x) = \int_x^\infty \frac{e^{-\nu}}{\nu} d\nu \ , \tag{A.2}$$

With exp (-βr) giving the probability of escape for an electron which travels a distance r to reach the surface, P(x) for the isotropic velocity distribution can be approximated for $x\beta \leq 1$ as

$$P(x) = \frac{1}{2} e^{-\alpha x} \ , \tag{A.3}$$

with $\alpha = 2\beta$, and β in units of 1 over distance.

4. The secondary electron escape length α^{-1} is much less than the Auger electron range R, so $\alpha R >> 1$. Range R is given by the empirical relation

$$R \approx 1000 * \frac{E^{1.4}}{\rho}, \tag{A.4}$$

where R is in angstroms, E in keV and ρ is the material density in g/cm3.

5. Each Auger electron of initial energy E which remains within the solid eventually results in excitation of N secondary electrons of average energy $\varepsilon =$ whose escape probability is described by P(x) and $N = E / \varepsilon$.

In figure 2.2 a) let the (0, y, z) plane be the surface of the sample, which occupies the $x > 0$ half-space. Consider Auger electrons of energy E created at position r_0 by an x-ray absorption event. The number of secondary electrons produced in volume element dr located at r by inelastic scattering per Auger electron originating from r_0 is given by $n(r, r_0, E)\, dr$. The probability that a secondary electron produced at r arrives at the sample surface (0, y, z) and escapes into the vacuum is represented by P(r) = P(x).

The number of secondary electrons which escape per Auger electron created at r_0 with energy E is given by

$$i(r_0) = i(x_0) = \int_{x>0} n(r, r_0, E) P(r) dr \quad , \tag{A.5}$$

To evaluate $n(r, r_0, E)$, assume that Auger electrons of range R create secondary electrons uniformly throughout the volume of a sphere of radius R centered on the source of the Auger electrons,

$$n(r, r_0, E) = \begin{cases} n(E) & \text{for } x \geq 0 \text{ and } |r - r_0| \leq R(E) \\ 0 & \text{for } x < 0 \text{ or } |r - r_0| > R(E) \end{cases} \quad , \tag{A.6}$$

For the case of $x_0 > R$, the total number of secondary electrons created per Auger electron is given by

$$N(E) = \int n(|r - r_0|, E) dr = n(E) \frac{4}{3} \pi R^3 = \frac{E}{\varepsilon} \quad , \tag{A.7}$$

where ε is on the order of secondary electron energies.

For P(r), the escape probability for secondary electrons created at depth x from the surface,

$$P(r) = P(x) = \frac{1}{2}\exp(-\alpha x) \quad , \tag{A.8}$$

is used where α^{-1} is the secondary electron escape length, which is much smaller than the Auger electron range R for the cases of interest.

To evaluate $i(x_0)$, consider figure 2.2 b) and first calculate $n(x,x_0)$, the number of secondary electrons produced in the volume defined by the planes perpendicular to the x axis at x and x + dx per Auger electron created at (x_0, 0,0),

$$n(x, x_0) = \begin{cases} \frac{3}{4}\frac{N}{R}\left[1 - \left[\frac{x - x_0}{R}\right]^2\right]dx & \text{for } \left|x - x_0\right| \le R \\ 0 \quad \text{for } \left|x - x_0\right| > R \end{cases} , \tag{A.9}$$

and their contribution to the secondary electron yield,

$$i(x, x_0) = n(x, x_0)P(x)dx = \frac{3}{4}\frac{N}{R}\left[1 - \left[\frac{x - x_0}{R}\right]^2\right]\exp(-\alpha x)dx \quad , \tag{A.10}$$

for $\left|x_0 - x\right| \le R$

The total contribution to the secondary electron current per Auger electron created at (x_0, 0, 0) is

$$i(x_0) = \int_{\max\{0, x_0 - R\}}^{x_0 + R} n(x, x_0)P(x)dx \quad ,$$

For $x_0 < R$, this gives

$$i(x_o) = \frac{3}{8}\frac{N}{\alpha R}\left[1 - \left[\frac{x_0}{R}\right]^2 + 2\frac{x_0}{R}\frac{1}{\alpha R} - \frac{2}{(\alpha R)^2}\right] + \frac{3}{4}\frac{N}{\alpha R}\exp\left[-\alpha(R + x_0)\right]\left[\frac{1}{\alpha R} + \frac{1}{(\alpha R)^2}\right] \quad , \tag{A.11}$$

and for $x_0 > R$,

$$i(x_0) = \frac{3}{8}\frac{N}{\alpha R}\left[\frac{2}{\alpha R} - \frac{2}{(\alpha R)^2}\right]\exp\left[-\alpha(x_0 - R)\right] + \frac{3}{4}\frac{N}{\alpha R}\exp\left[-\alpha(R + x_0)\right]\left[\frac{1}{\alpha R} + \frac{1}{(\alpha R)^2}\right] , \tag{A.12}$$

In both equations the second term containing exp $[-\alpha(R+x_0)]$, can be neglected, since $\alpha R >> 1$.

Examining figure A.1, the XBPM blades sit within the spatial distribution of low energy photons as calculated by SRW. The figure displays an energy cross-section of the spatial distribution of the HXMA wiggler spectrum. It is apparent that generally as the energy increases the synchrotron radiation distribution occupies more of the central region of the aperture and not the borders. With this in mind an estimation of the secondary electron current induced by Auger electrons, detailed above, will be obtained for the gold coating used on the CVD diamond blades. For gold use Auger energy of 2016 eV (MNN lines), a secondary electron energy of 5 eV, a gold density of 19.3 g/cm3, and a escape length α^{-1} of 5 angstroms. Substituting into equation A7, the number of secondary electrons created is

$$N = \frac{E}{\varepsilon} = \frac{2016\,\text{eV}}{5\,\text{eV}} = 403.2 \quad ,$$

while the range R of the Auger electron is estimated from equation A.4

$$R = 1000 * \frac{E^{1.4}}{\rho} = 1000 * \frac{(2016\text{eV})^{1.4}}{19.3\ \text{g/cm}^3} = 138.27\,\overset{0}{\text{A}},$$

Finally, substituting N, R and α into equation A.11 and A.12 it is possible to obtain the contribution to the secondary electron current. Calculating the sum of equations A.11 and A.12, which is proportional to the total electron yield (TEY) current, multiplying by the electron charge, photon flux, normal incidence cross-sectional ratio, Auger electron quantum yield and number of absorption events this should in principle equal the TEY signal generated by the Auger process.

The equation for the TEY current then has the form

$$I = e \cdot I_0 \cdot (\alpha_{Au} \cdot area\ \ ratio\ ) \left\{ \left[i_{A.11} \cdot 50 \cdot \left(1 - e^{-\mu \cdot x}\right) \right] + \left[i_{A.12} \cdot 50 \cdot \left(1 - e^{-\mu \cdot x}\right) \right] \right\}, \qquad \text{(A.13)}$$

where

e = 1.602 x 10^{-19} C,

$i_{A.11}$, $i_{A.12}$ = number of secondary electrons calculated from A.11 and A.12,

I_0 = incoming photon flux (determined from SRW),

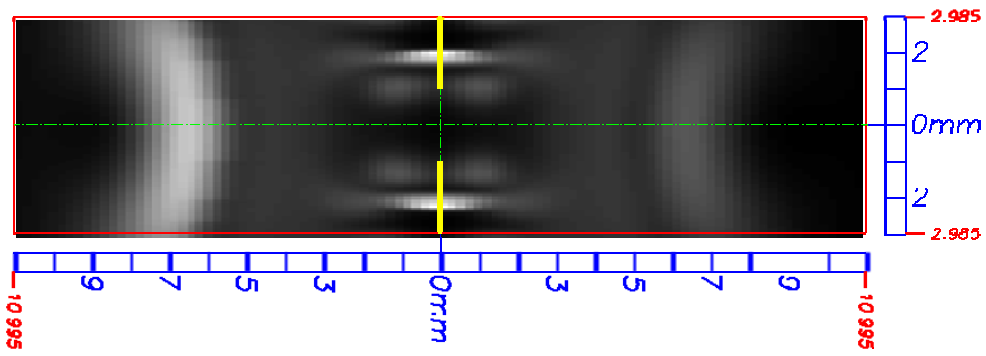

Figure A.1 Synchrotron radiation spatial distribution (simulated) for the HXMA wiggler at 2 keV. Visible are the XBPM blades (yellow) and XBPM aperture (blue scale) for visual reference. From the SRW simulation it is clear that the 2 keV slice of the wiggler spectrum intercepts the blades.

μ = photoelectric cross-section (tabulated on the NIST website),

α Au = Auger yield of gold.

Note that the auger yield a is by,

$\alpha = 1 - \varpi = 1 - 0.03 = 0.97$,

where ω is the fluorescence yield of Au, respectively [58]. The factor of 50 is a simplification where all the M absorption edges of Au are excited with equal probability. The normal incidence cross-sectional ratio of the XBPM blade is given by

$$\frac{Area\ of\ blade}{Area\ of\ FM\ aperture} = \frac{2\,\text{mm} * 0.127\,\text{mm}}{5.97\,\text{mm} * 21.99\,\text{mm}} = 1.935x10^{-3} = 2x10^{-3} ,$$

Substituting values of R, N and alpha into equations A.11 the number of secondary electrons contributing to the current is,

$$i(x) = \frac{3}{8}\frac{403.2}{2x10^{9}\cdot \frac{1}{m} * 138.27\,\overset{0}{A}}\left[1 - \left[\frac{x}{138.27\,\overset{0}{A}}\right]^{2} + 2\frac{x}{138.27\,\overset{0}{A}}\frac{1}{2x10^{9}\cdot \frac{1}{m} * 138.27\,\overset{0}{A}} - \frac{2}{\left(2x10^{9}\cdot \frac{1}{m} * 138.27\,\overset{0}{A}\right)^{2}}\right] = 532.176$$

with the summation range x = 0 to 138 Å.

Similarly for equation A.12,

$$i(x) = \frac{3}{8}\frac{403.2}{2x10^{9}\cdot \frac{1}{m} * 138.27\,\overset{0}{A}}\left[\frac{2}{2x10^{9}\cdot \frac{1}{m} * 138.27\,\overset{0}{A}} - \frac{2}{\left(2x10^{9}\cdot \frac{1}{m} * 138.27\,\overset{0}{A}\right)^{2}}\right]\exp\left[-2x10^{9}\cdot \frac{1}{m}\left(x - 138.27\,\overset{0}{A}\right)\right] = 2.219$$

with the summation range x = 138 Å to 500 Å.

Substituting values into equation A.13 yields

$$I = \left(1.602x10^{-19}\ \mathrm{C}\right)\left(3.2525x10^{13}\ \frac{1}{\mathrm{s}}\right)(0.97\cdot 0.002)\left\{\begin{array}{l}\left[\left[532.176\cdot 50\cdot\left(1-e^{-\frac{1.926*10^{6}}{\mathrm{m}}*x}\right)\right]\right]\\ +\left[\left[2.219\cdot 50\cdot\left(1-e^{-\frac{1.926*10^{6}}{\mathrm{m}}*x}\right)\right]\right]\end{array}\right\}*\frac{2}{5}$$

$$= 1.1x10^{-6}\ \mathrm{A}$$

$$\approx 1\,\mu\mathrm{A}$$

The factor 2/5 is to scale the result from the SRW simulated flux calculated at 500 mA to measured by the XBPMs at 200 mA. As can be seen the measured current signal is predominately from the lower energy VUV photons.

YAG Temperature Calculation

The following thermal analysis follows the works by Nian and Kuzay et al. [52, 53]. Starting from the heat conduction equation with steady state and an axisymmetrical Gaussian heat flux, the governing equation 2.12 is [52]

$$\frac{1}{r}\frac{\partial}{\partial r}\left(r\frac{\partial T}{\partial r}\right)+\frac{q_0}{kt}\exp\left(-\frac{r^2}{2\sigma_0^2}\right)=0 \quad , \tag{A.14}$$

where

T = maximum temperature increase,

q_0 = maximum heat flux [W/m^2],

k = thermal conductivity [W/ (m ·K)],

t = thickness [m],

and σ_0 = Gaussian standard deviation (for distributed heat flux).

The boundary conditions are T = 0 (could be other fixed values, this is for convenience) when r = a, the radius of the YAG disk, and T = finite when r = 0, i.e. the center of the disk.

Integrating twice,

$$T=-\frac{q_0\sigma_0^2}{2kt}E_1\left(\frac{r^2}{2\sigma_0^2}\right)+\frac{c_1}{2}\ln\left(\frac{r^2}{2\sigma_0^2}\right)+c_2,$$

and applying the boundary conditions results in

$$T = -\frac{q_0\sigma_0^2}{2kt}\left[E_1\left(\frac{r^2}{2\sigma_0^2}\right) + \ln\left(\frac{r^2}{2\sigma_0^2}\right) - E_1\left(\frac{a^2}{2\sigma_0^2}\right) - \ln\left(\frac{a^2}{2\sigma_0^2}\right)\right] \ ,$$

where E_1 is the exponential integral (the exponential function of the first kind) defined in Abramowitz and Stegun [59]. The negative sign in the above equation (outside the square bracket) has been derived in our solution of the Poisson equation A.13, which was missed in the original formulas of Ref. 52.

Maximum temperature is located at the center of the disk, r = 0, and letting

$E_1(0) + \ln(0) = -\gamma$ (Euler's constant), results in equation 2.13

$$T_{\max} = \frac{q_0\sigma_0^2}{2kt}\left[E_1\left(\frac{a^2}{2\sigma_0^2}\right) + \ln\left(\frac{a^2}{2\sigma_0^2}\right) + \gamma \right], \qquad \text{(A.15)}$$

where

Tmax = maximum temperature increase relative to that at the disk edge,

q_0 = maximum heat flux [W/m^2],

σ_0 = Gaussian standard deviation (for distributed heat flux) [m],

k = thermal conductivity [W/ (m ·K)],

t = disk thickness [m],

a = radius of the thin disk [m],

E_1 = exponential function the first kind,

γ = Euler's constant = 0.57721…

As an example consider the HXMA beamline with the YAG imaging system located 15 meters from the source at 10 mA storage ring current. Using SRCalc it is possible to estimate the heat flux and total absorbed power, which is used to determine the standard deviation.

q_0 = 0.8290 W/m^2,

Total Power = Tp = 56.4645 W,

$$\sigma_0 = \sqrt{\frac{T_p}{2\pi q_0}} = \sqrt{\frac{56.4645\ \text{W}}{2\pi \cdot 0.8290\ {}^{\text{W}}\!/_{\text{m}^2}}} = 3.292\,x10^{-3}\,\text{m} \ ,$$

Recall that 4 graphite filters, 250 microns thick, where used in the SRCalc program to reduce the power delivered by the HXMA beamline. Using the parameters for the YAG disk,

k = 14 W/ (m ·K),

t = 200 mm,

a = 0.0254 m,

and substituting everything into equation A14, the maximum increase of YAG disk temperature is calculated to be

Tmax = 4519 K = 4246 ^{0}C,

which is above the YAG melting point of 1972 ^{0}C.

For CMCF, at 17 m from the source and 10 mA, using the above parameters for the YAG disk, and the following values from SRCalc,

q_0 = 0.6514 W/m^2,

Total Power = Tp = 2.7849 W,

$$\sigma_0 = \sqrt{\frac{T_p}{2\pi q_0}} = \sqrt{\frac{2.7849\,\mathrm{W}}{2\pi \cdot 0.6514\,{}^{\mathrm{W}}\!/_{\mathrm{m}^2}}} = 8.249x10^{-4}\,\mathrm{m}\ ,$$

the maximum temperature increase is calculated to be

Tmax = 442 K = 169 ^{0}C.

APPENDIX B: TRANSLATIONAL STAGES

Problems Encountered with the CMCF Translational Stages

In section 4.1 reasons are stated as to why experiments could not be performed on the CMCF XBPM due to problems with the translational stage. To recap, the downstream photon shutter is connected to the FM (to which the XBPM is attached) via a bellows is displayed in figure B.1. Ideally any forces of motion caused by the opening and closing of the photon shutter should be damped by the connecting bellows minimizing any alignment perturbations of the FM.

Unfortunately the connecting bellows are under too much tension so that when the photon shutter is opened or closed translational forces are transmitted through the bellows and FM to the translational stage. The end result is that the stage is pulled out of its proper aligned position so that the FM and XBPM are no longer in the correct fiducial locations. Engineers at the CLS are working to rectify the problem. However, when another stage further downstream was removed from the beamline FE a number of other problems came to light, refer to figure B.2.

It was discovered that the holes in the base plate of the translational stage were slightly larger than the diameter of the supporting posts. With the repeated jarring of being pulled out of position by the shutter the posts became loose resulting in a structurally unsteady motion, i.e. ‘wobble’. The bearings that move along the posts where also discovered to be loose thus contributing to the ‘wobble’ of the structure.

Engineers at the CLS performed cantilever displacement measurements in order to diagnose the extent of the problem. (A 300 mm bar was attached to the top of the stage and weights incrementally added to the free end). The displacement of the structure was measured at points (c) and (d) of figure B.2. When the bearings were replaced and the supporting posts tightened the wobble was significantly reduced but there was still a factor of 2 difference between displacement measurements of points (c) and (d). Engineers are working to rectify the problems.

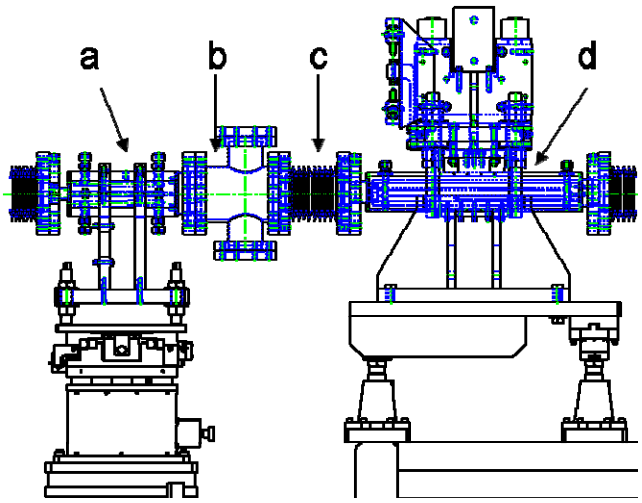

Figure B.1 Elevation plan drawing of the CMCF front end showing the fixed mask (a), vacuum cross housing the XBPM (b), bellows (c), and block type photon shutter (d).

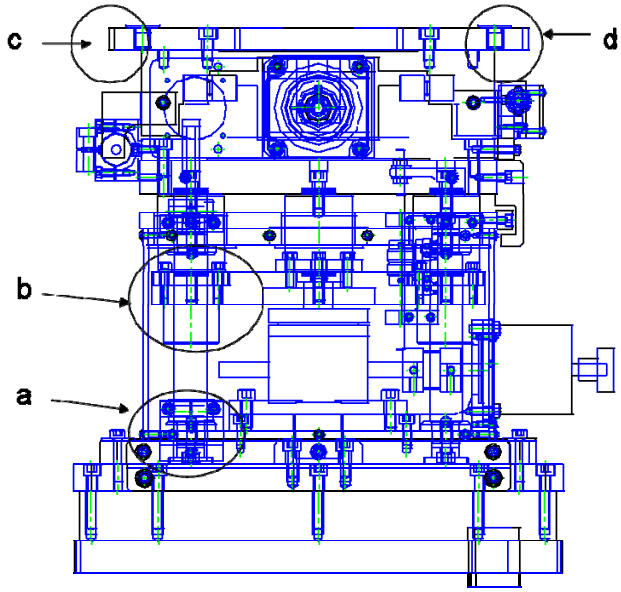

Figure B.2 Schematic of a translational stage used within a beamline front end. Indicated on the drawing are the post connections to the base (a), bearing (b), and locations of displacement measurements (c & d).

APPENDIX C: EXPERIMENTAL DATA

Translational Stage Resolution

The following figures demonstrate the relationship between the translational stage motor step size, encoder reading and ADC value for the HXMA, CMCF and XSR beamlines. A numerical fit, performed by Excel, is displayed on the encoder vs. step size graphs to determine the resolution of the stage. Refer to section 4.2 for commentary of figures.

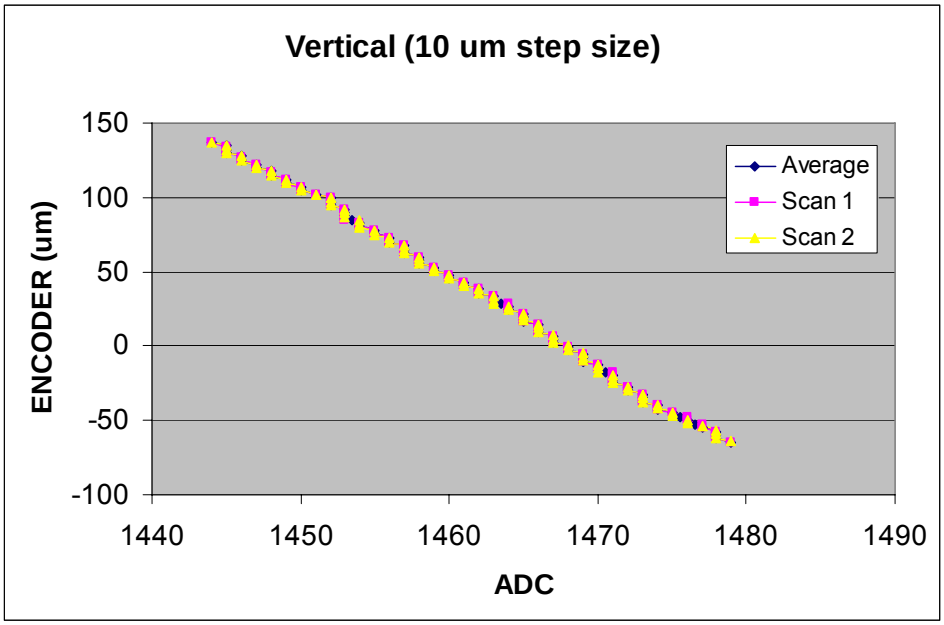

Figure C.1 Encoder versus ADC for the HXMA XBPM over a small, 200 micron, scan range. The resolution of the ADC is ~ 5 microns.

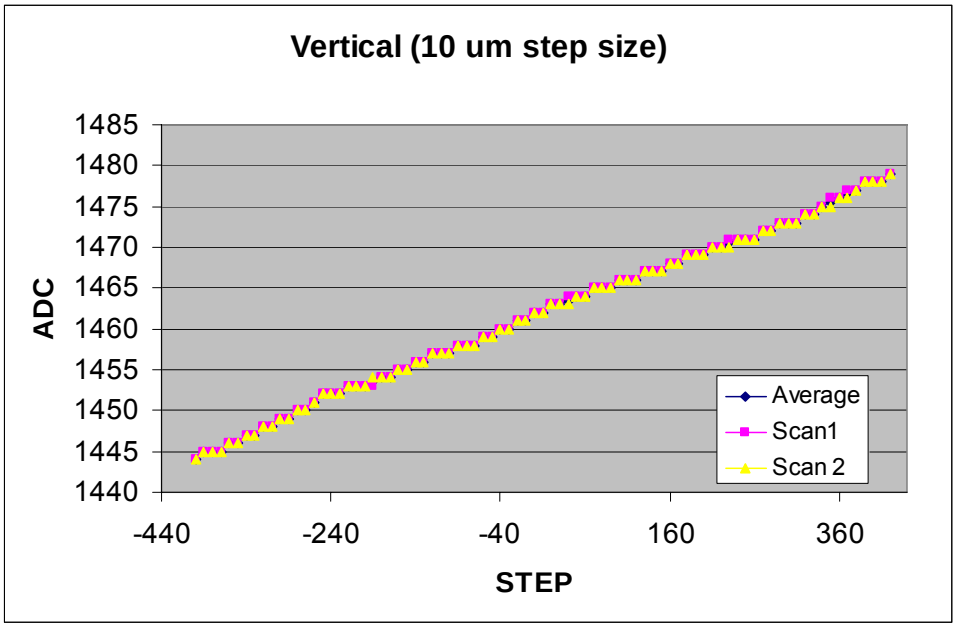

Figure C.2 ADC versus step size for the HXMA XBPM.

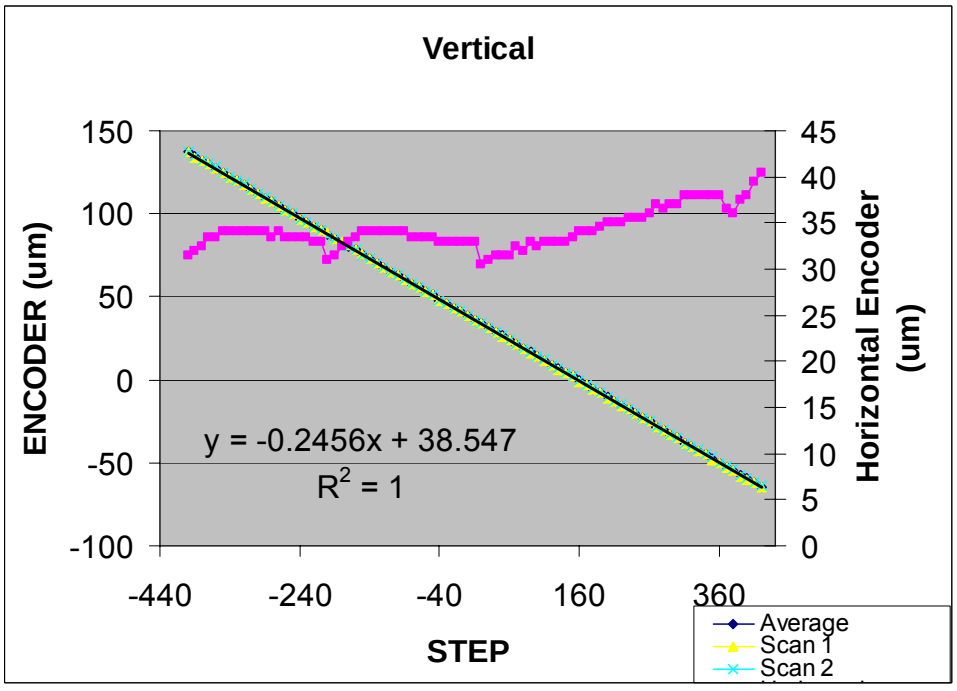

Figure C.3 Encoder versus step size for the HXMA XBPM translational stage. The slope of the fit indicates the calibration of the stage.

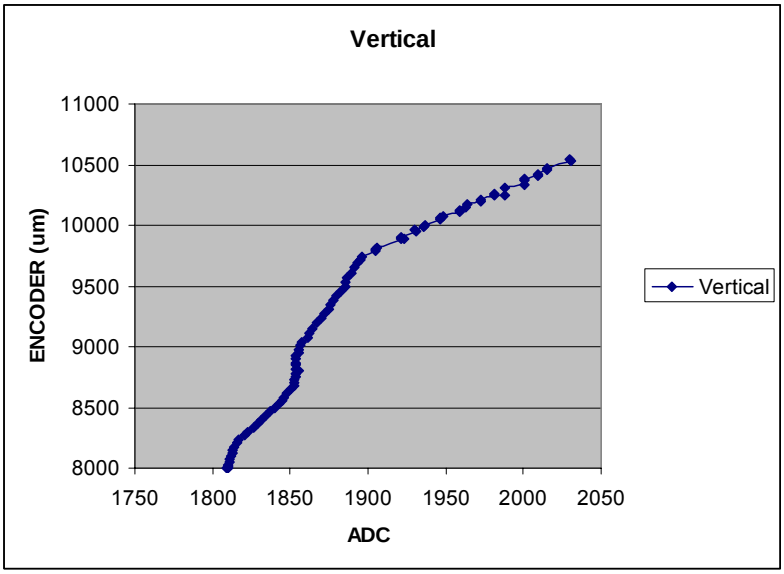

Figure C.4 CMCF vertical stages scan. The decidedly non-linear relation between the encoder and the ADC indicates a problem with either the electronics or the stage itself.

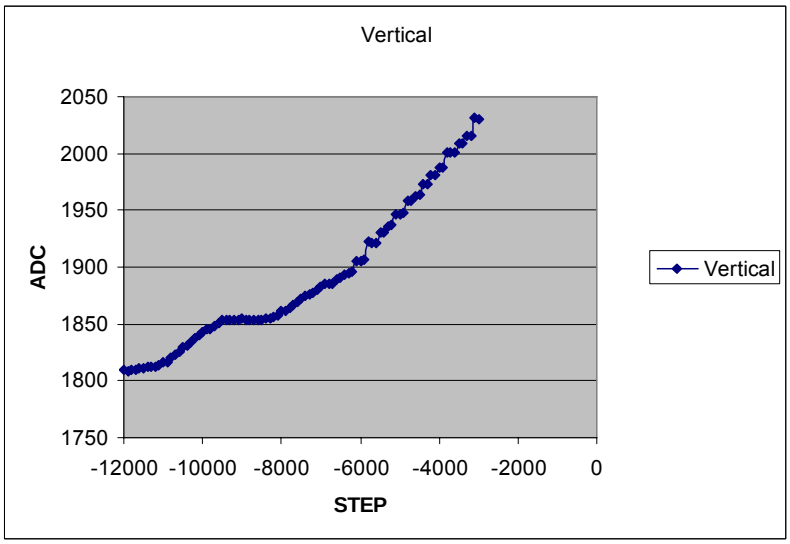

Figure C.5 Large vertical scan of the CMCF XBPM translation stage. Non-linear relation indicates a problem either with the electronics or the stage.

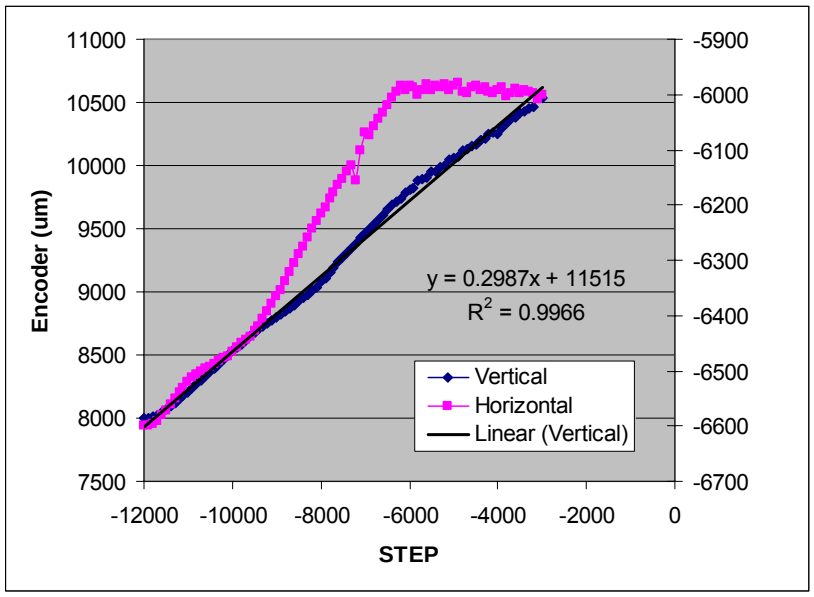

Figure C.6 Determination of the resolution of the CMCF vertical translational stage. While the encoder versus step follows a fairly linear trend the horizontal motion does not. Horizontal motion (right vertical axis) is over a range of ~600 microns.

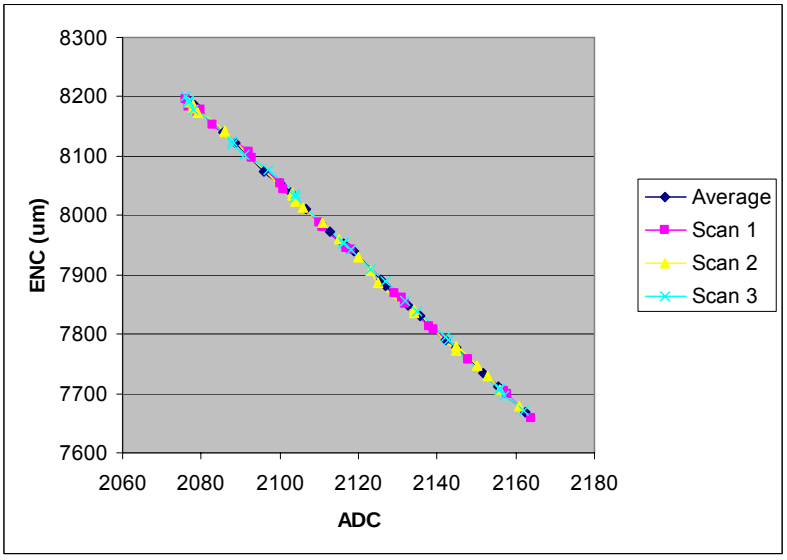

Figure C.7 Smaller range scans of the CMCF vertical stage. Over the smaller scan the relationship between encoder and ADC is decidedly more linear.

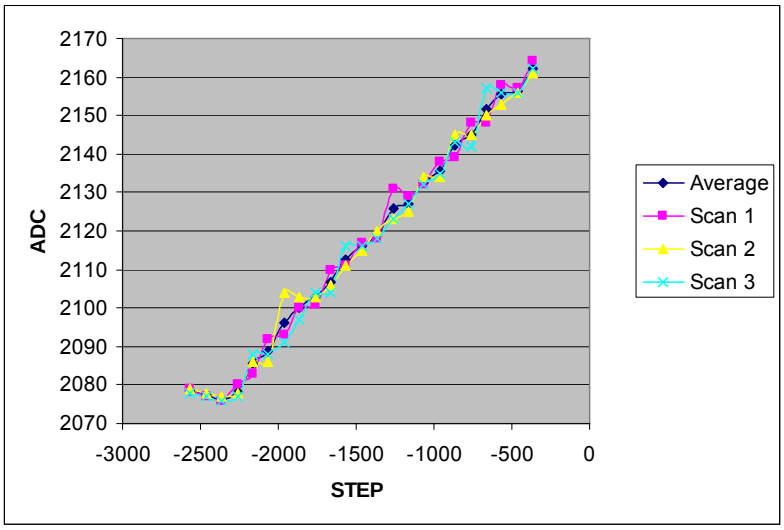

Figure C.8 While the average of the scans follows an approximately linear trend, each individual scan for the CMCF stage has a definite 'undulation'.

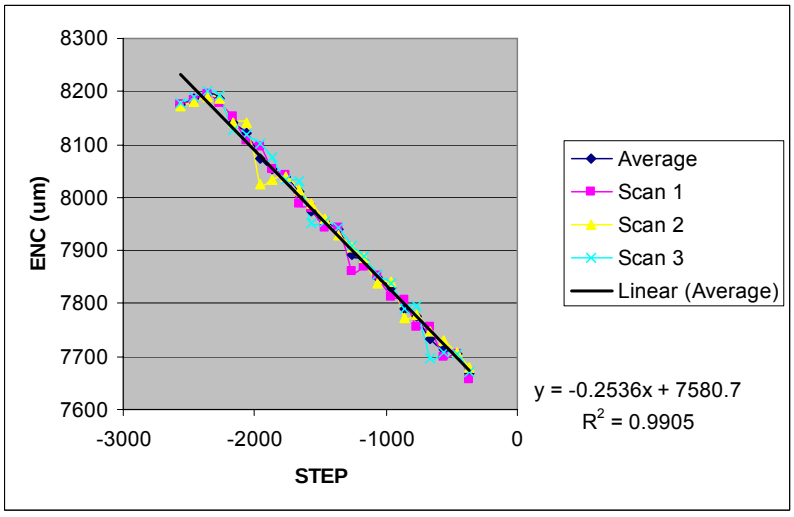

Figure C.9 Calibration of the CMCF vertical stage. Slope of the Excel fit indicates a calibration of ~0.25 micron/step.

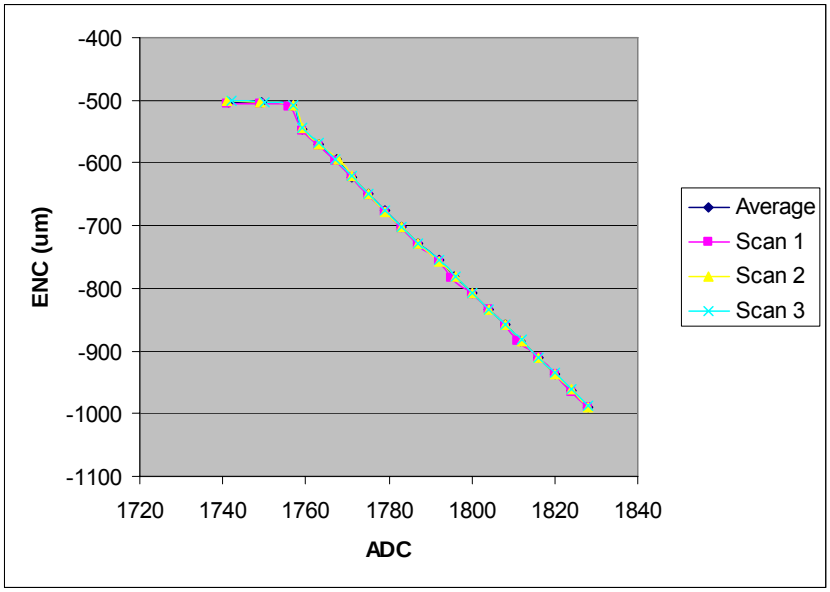

Figure C.10 Small scan of the XSR vertical translational stage. Due to intermittent use the translational stage displays a significant amount of 'stickiness' at the beginning of the scan. Subsequent scans were unaffected.

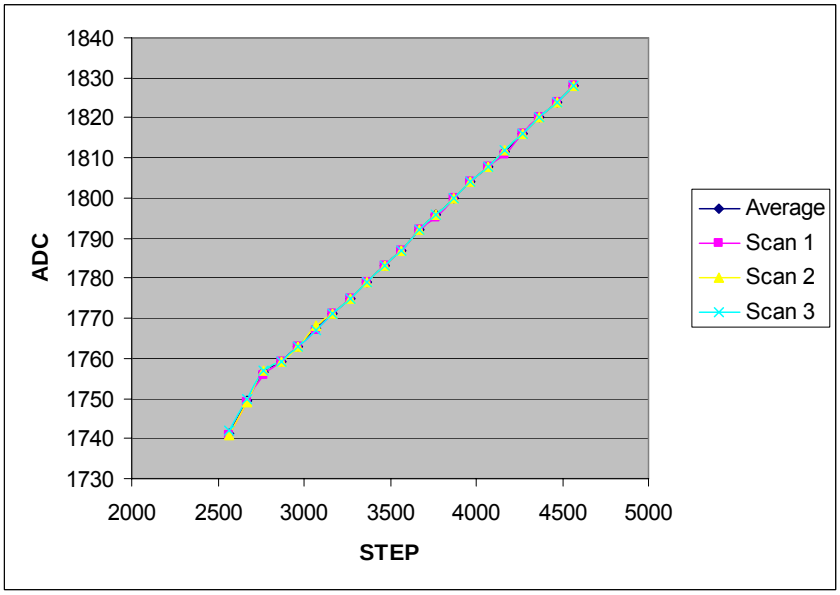

Figure C.11 Relation between ADC and step for the XSR vertical stage.

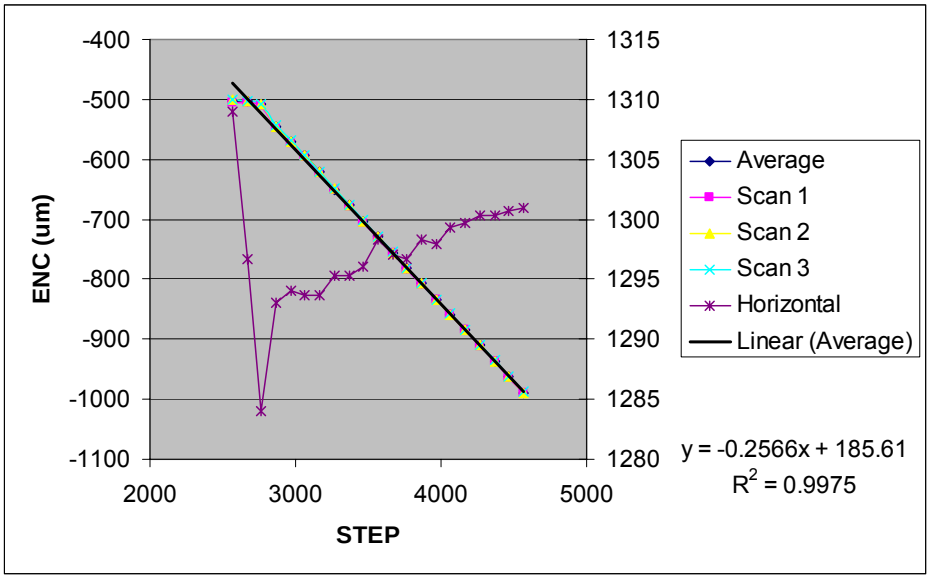

Figure C.12 Calibration of the XSR vertical translational stage determined from the linear Excel fit. The drastic change in horizontal position is due to overcoming the translational stages 'stickiness'.

XSR XBPM Resolution

The following figures are the averages of the scan data used to determine the spatial resolution of the XSR XBPM. Two figures for each data collection scheme will be presented. The first figure of each set was obtained to ensure that a 1 micron (or smaller) displacement of the translational stage corresponds to an equal displacement in current measured by the XBPM blades. The second figures in each set were used to determine the calibration coefficient of the XBPM through a polynomial fit.

Group 1:

The data acquisition MatLab script, refer to Appendix D, was set to a motor step size of 4, a pause time of 1 second and the number of stage movements to 200. Eight scans were obtained with four scans used for the average.

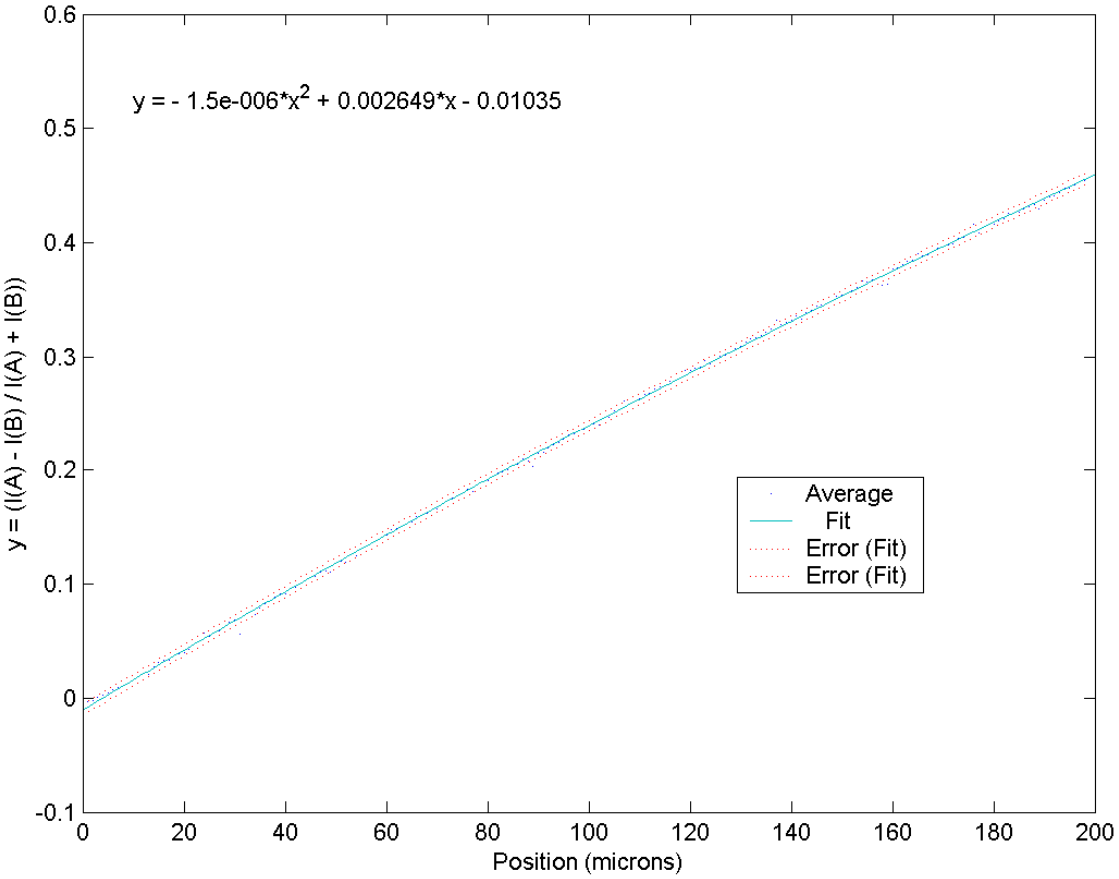

Figure C.13 MatLab polynomial fit to the average of scans 5, 6, 7, and 8. A second order polynomial was fitted to the data with the reciprocal of the linear term providing the calibration coefficient. Two sigma error bars are plotted with the fit.

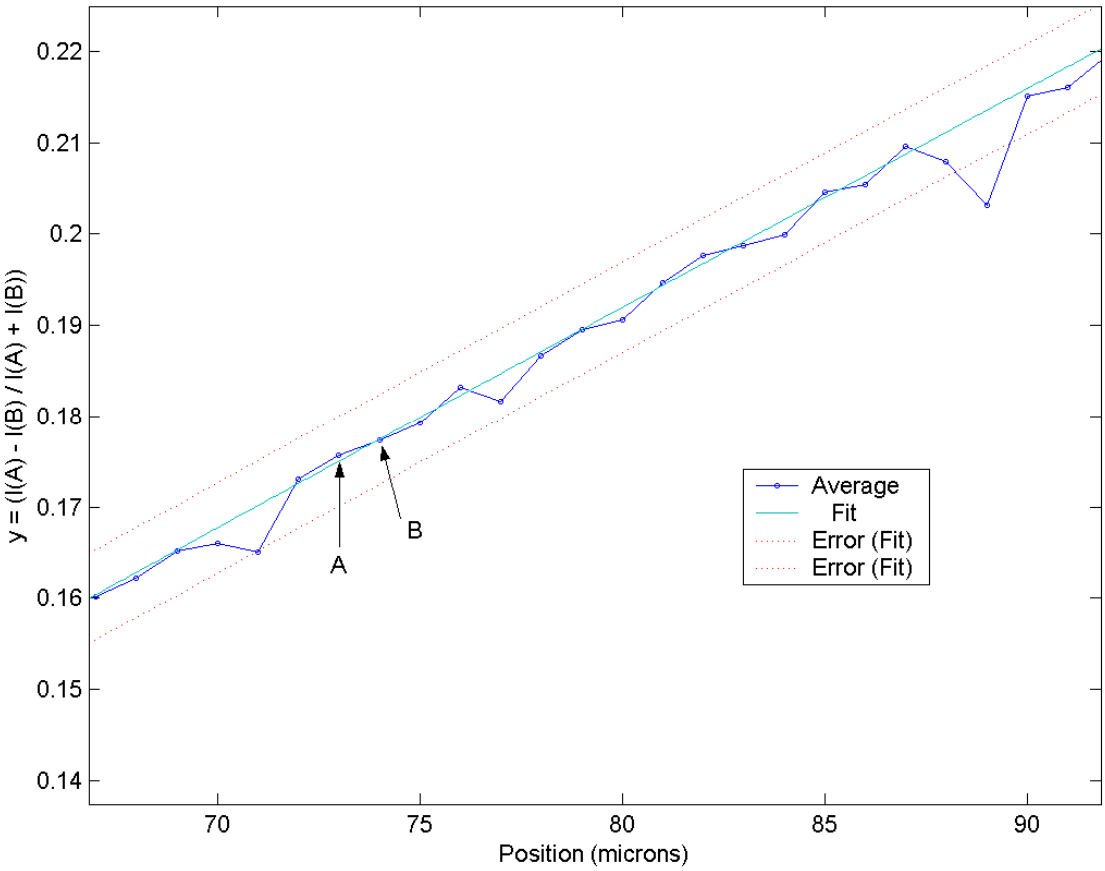

Figure C.14 Close in zoom of figure C.13. Points A and B were selected to confirm motor step size. Estimated step size is 1 micron. Calculated step size is 0.7364 micron. Two sigma error bars are plotted with the fit.

Group 2:

For the acquisition script the motor step size and pause time were held at 4 and 1, respectively, while the number of times the stage was moved was decreased to 50. Three scans were obtained and used in the following figures.

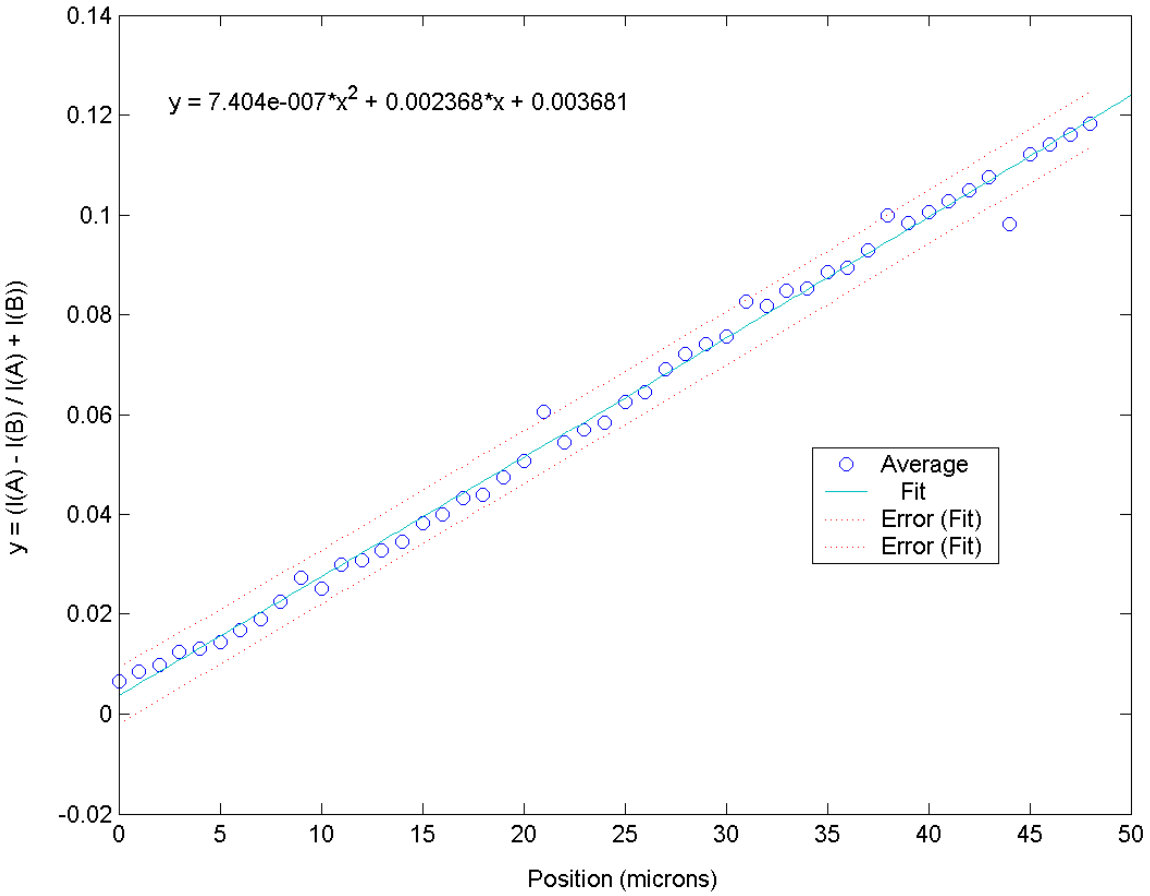

Figure C.15 Polynomial fit to average of scans 9, 10 and 11. A second order polynomial was fitted to the data with the reciprocal of the linear term providing the calibration coefficient for the XBPM. Two sigma error bars are plotted with the fit.

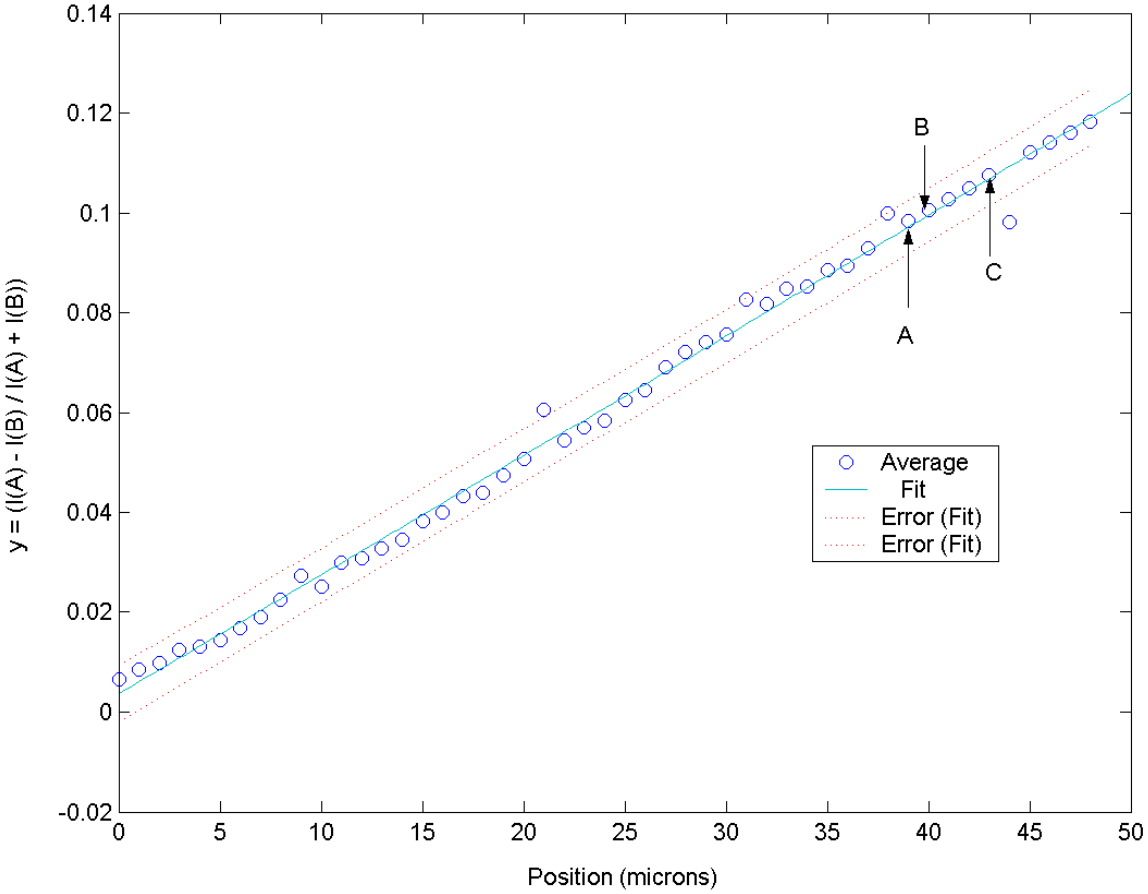

Figure C.16 Points A and B were selected to confirm motor step size. Estimated step size is 1 micron. Calculated step size is 0.9874 micron. Spacing between points A and C is estimated at 4 microns and calculated to be 3.985 microns. Two sigma error bars are plotted with the fit.

Group 3:

For this group of scans the motor step size was decreased to 2, the pause time decreased to 0.5 seconds, and the number of stage movements to 100. Four scans were obtained with three used in the analysis.

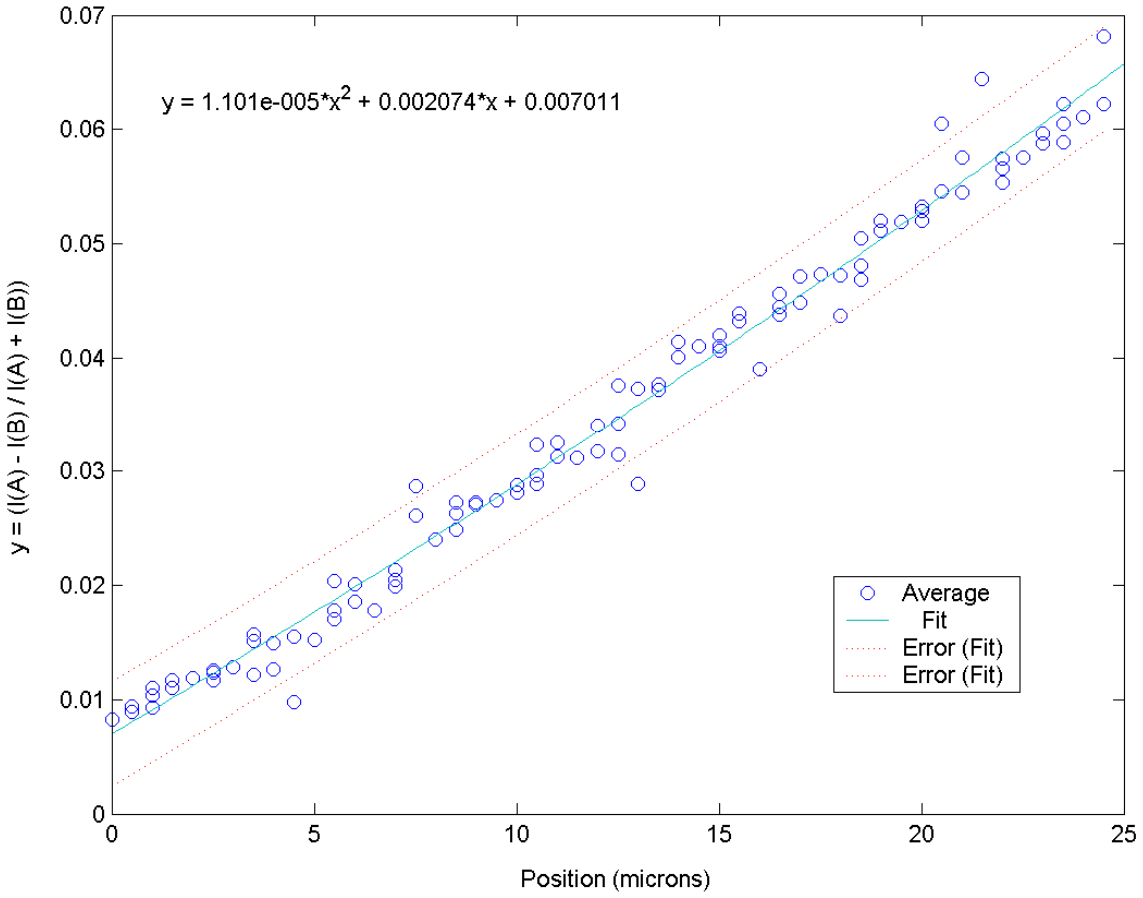

Figure C.17 Polynomial fit to average of scans 13, 14 and 15. A second order polynomial was fitted to the data with the reciprocal of the linear term providing the calibration coefficient for the XBPM. Two sigma error bars are plotted with the fit.

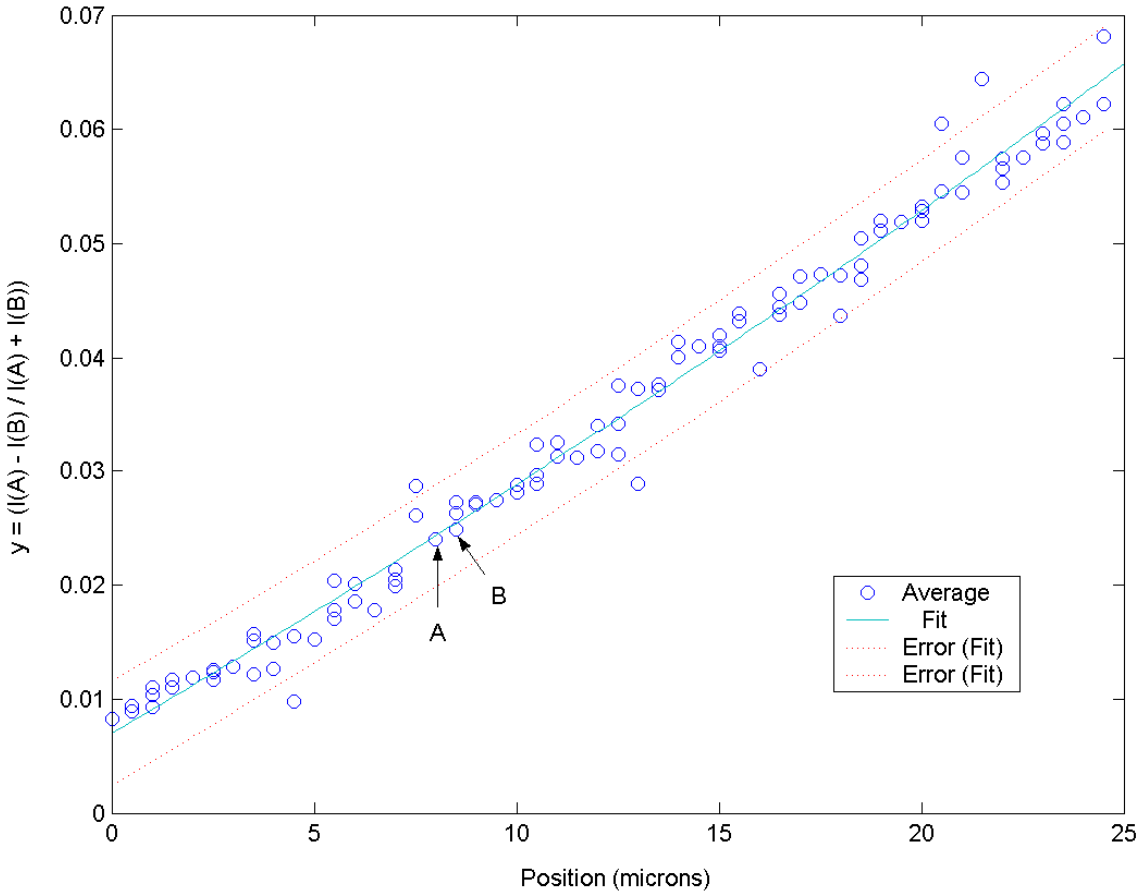

Figure C.18 Points A and B were selected to confirm motor step size. Estimated step size between three points is 1 micron. Calculated step size is 0.9978 micron. Two sigma error bars are plotted with the fit.

Group 4:

Group 4 consists of 5 scans, three of which are used in the analysis. The motor step size was set to 1, with a pause time of 0.25 seconds and moving the stage 200 times. MatLab was unable to perform a polynomial fit on the acquired data.

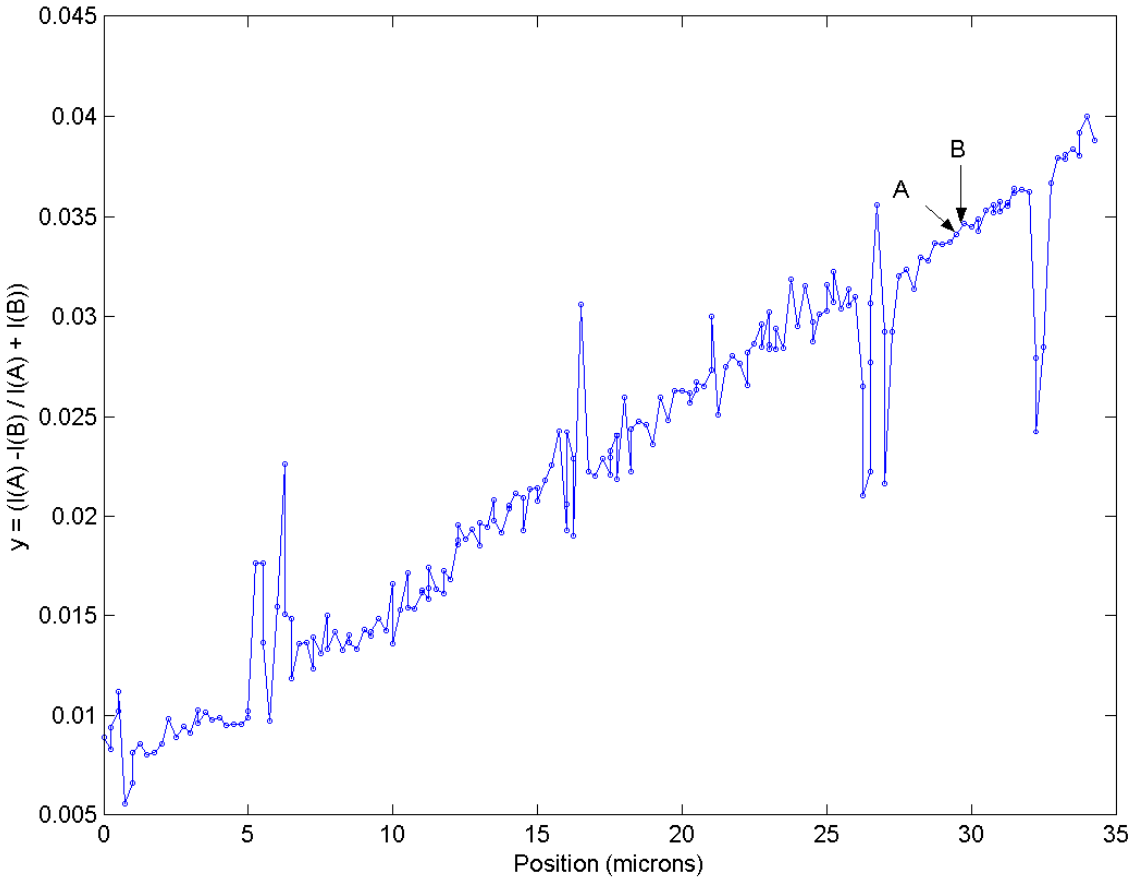

Figure C.19 Average of scans 16, 17 and 20. Spacing between consecutive data points should equal 0.25 microns. Calculated to be 0.2214 microns. Two sigma error bars are plotted with the fit.

Group 5:

The MatLab script was set with a motor step size of 1, a pause time of 1 second and the number of times moved at 200. Five scans were attempted with three being used in the analysis.

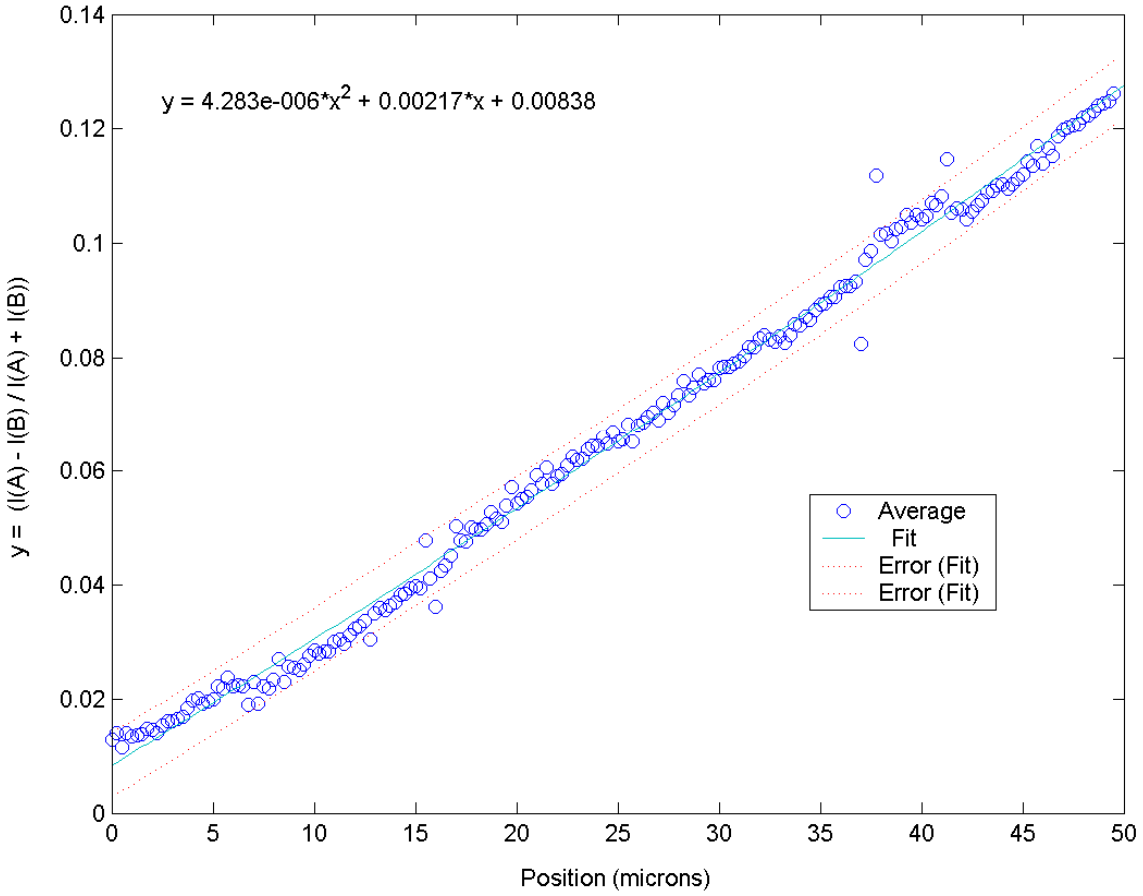

Figure C.20 Second order polynomial fit to the average of scans 21, 22 and 23. The reciprocal of the linear term provides the calibration coefficient for the XBPM. Two sigma error bars are plotted with the fit.

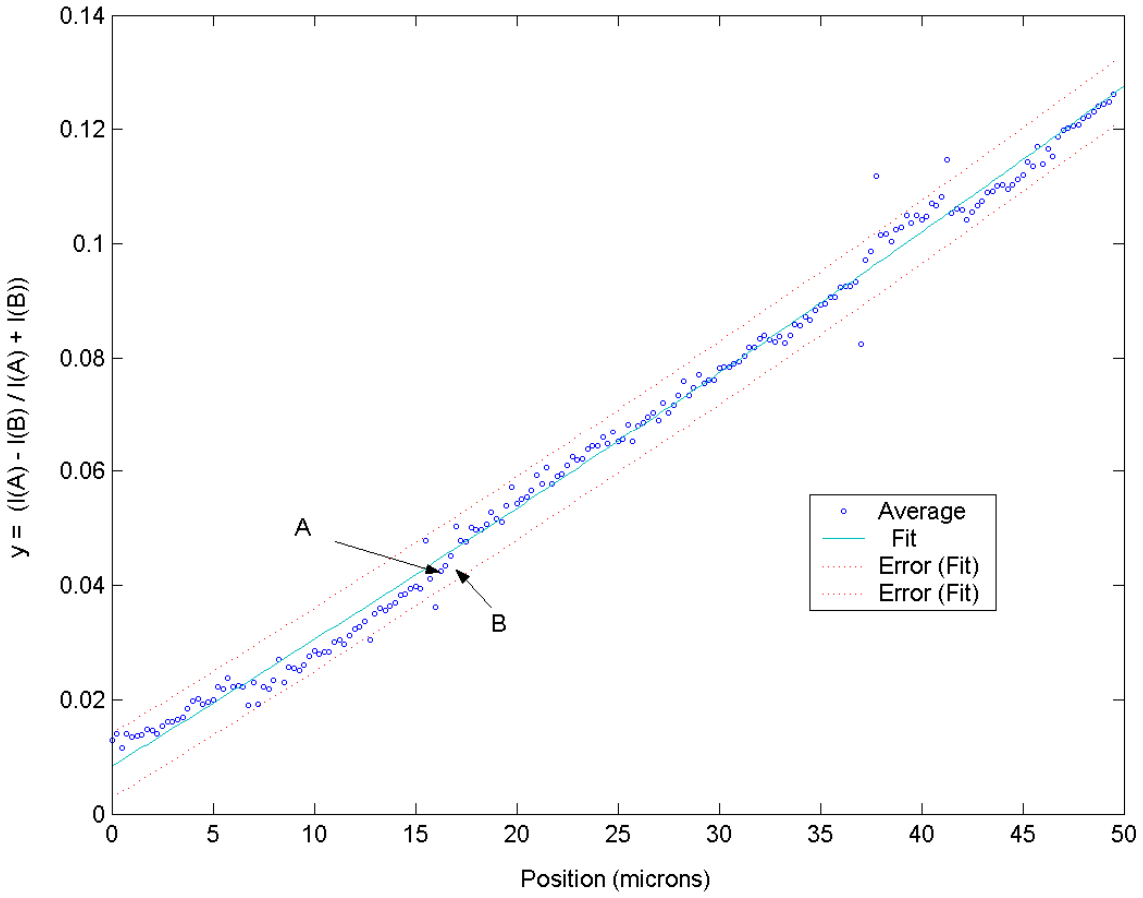

Figure C.21 Points A and B selected to confirm motor step size. Estimated step size between three points is 0.5 microns. Calculated step size is 0.4562 microns. Two sigma error bars are plotted with the fit.

APPENDIX D: PROCEDURES

Translational Stage Calibration Procedure

For each of the three translational stages the following procedure was used:

- The stage was moved vertically up (or down) until one of the limit switches tripped the motor
- The step size was set on the motor control panel
- Record the step value, ADC value, and both vertical and horizontal encoder values
- In incremental steps, the stage was, moved towards the other limit switch; the step value, ADC, and encoder values were recorded at each step
- After the scan was finished, the following plots were made: encoder vs. ADC, encoder vs. step, and ADC vs. step. If linear trends did not result this could indicate problems with the encoders, ADC, or motor control drivers that needed to be fixed before continuing
- Based on the number of steps from limit-to-limit, the stage was moved so that it was roughly within the middle of its range.
- The stage was moved, vertically up or down, in increments recording the step value, ADC value, and encoder values until the stage had moved a total of 500 microns (obtained from the change in initial and final encoder values). Repeat process three times. (Note: the 500 microns was chosen so that if an experiment was being performed on the beamline at the time of the scan there would be a roughly 400 micron safety clearance so that no blade shadow would propagate down the line).
- Obtain an average of the results and plot encoder vs. ADC, encoder vs. step and ADC vs. step. The identifiable slope obtained from the encoder vs. step plot is the resolution of the translational stage motion.

MatLab Script

The MatLab script below was used to acquire the data needed to determine the spatial resolution of the XSR XBPM. The first part of the script deals with calling the necessary process variables from the network in order to obtain a measurement. For instance the handle "SR_mA" is used to call the value of the measured storage ring current which is then stored in the vector "data_SR." Similar calls are made in order to obtain the measured currents off of the XBPM blades, ADC values, and if necessary the NPLC setting for the Keithley picoammeter. The motor step size and number of times to move the translational stage is also set in the first part of the script.

The second part of the script consists of a basic "while" loop in which values for the process values are measured and stored in vectors; then the stage is moved by an incremental amount as determined by the step size. Duration of the "while" loop is determined by the number of times to move the translational stage. Pause time is set within the body of the "while" loop.

Finally the script calls the "plot" function to graph the data obtained from each blade and to also provide a graph of the ratio of blade A to blade B (for the XSR XBPM).

Comments are prefaced by the percentage symbol, "%." The symbol is also used to turn off sections of code that are not to be used at this time. For example, after the "while" loop there are a couple of lines that would attempt to return the stage to its origin position. This operation only meet with limited success so the lines were turned off and the stage moved back to the origin as described in section 4.3

```
%This script will move the XBPM motors and acquire the current signal
%from the Storage ring and XBPM blades.

%Set the number of times want the motor to move
TimesMove = 200;

%Set the step size
StepSize = 1;
```

```
%Getting the storage ring XBPM blade currents
%For HXMA: Blade A = A1406-02:uA:fbk, Blade B = A1406-01:uA:fbk
%For CMCF: Blade A = A1408-04:uA:fbk, Blade B = A1408-03:uA:fbk
%          Blade C = A1408-02:uA:fbk, Blade D = A1408-01:uA:fbk
%For XSR:  Blade A = A1402-02:uA:fbk, Blade B = A1402-01:uA:fbk
SR_mA = mcaopen('PCT1402-01:mA:fbk');
Blade_A = mcaopen('A1402-02:uA:fbk');
Blade_B = mcaopen('A1402-01:uA:fbk');
%Need to add handles for Blade C and D of CMCF

%Record current ADC value, "origin" position
%For HXMA:  Vertical = SMTR1406-I00-02:
%For CMCF:  Vertical = SMTR1408-I00-02:
%          Horizontal = SMTR1408-I00-01:
%For XSR:   Vertical = SMTR1402-B20-02:
h_ADC_fbk = mcaopen('SMTR1402-B20-02:adc:fbk');
currentADC_fbk = mcaget(h_ADC_fbk);
h_ADC_sp = mcaopen('SMTR1402-B20-02:adc');
ADC_sp = mcaget(h_ADC_sp);

%Get the current position of the stepper motor
h_Position = mcaopen('SMTR1402-B20-02:step:fbk');
SetPt = mcaopen('SMTR1402-B20-02:step');

%Get the NPLC and change to a value
%h_NPLC_A = mcaopen('A1402-02:nplc');
%h_NPLC_B = mcaopen('A1402-01:nplc');
%NPLC_A_sp = mcaget(h_NPLC_A);
%NPLC_B_sp = mcaget(h_NPLC_B);
%mcaput(h_NPLC_A, 1);
%mcaput(h_NPLC_B, 1);
```

```
pause(3);

%Starting the stopwatch
tic;

%Move the motor and acquire current data
i = 1;
m = 1;
while (i < TimesMove)
   data_SR(m) = mcaget(SR_mA);
   data_A(m) = mcaget(Blade_A);
   data_B(m) = mcaget(Blade_B);
   data_time(m) = toc;
   Position(m) = mcaget(h_Position);
   data = [toc data_SR(m) data_A(m) data_B(m) Position(m)];
   data
   currentPosition = mcaget(h_Position);
   mcaput(SetPt, currentPosition + StepSize);
   i = i + 1;
   m = m + 1;
   pause(1);
end

%Move stepper motor back to ADC "origin" position, reset NPLC
mcaput(h_ADC_sp, ADC_sp);
%mcaput(h_NPLC_A, NPLC_A_sp);
%mcaput(h_NPLC_B, NPLC_B_sp);

subplot(2,1,1)
plotyy(Position, data_A, Position, data_B)
subplot(2,1,2)
```

```
y = data_A ./ data_B;
plot(Position, y)
```

Spiricon Image Acquisition Procedure

Simply stated the steps used to acquire the visible fluorescence of SR from the CMCF undulator on the YAG crystal were:

- Do not use YAG crystal for storage ring currents greater than 10 mA
- Confirm that undulator is at maximum gap
- Set data, result and image logging features to "on" within the Spiricon exports menu
- Set the image capture to acquire a pre-determined number of frames or to acquire images within a set time period. (Using the set time period is easiest but both methods are limited by the frame size and available space on the hard drive).
- Press the "START" button on the Spiricon tool bar to start acquiring images. Button will automatically change to "STOP".
- With photon shutter closed obtain dark image so that Spiricon can calibrate the background using the UltraCal^{TM} feature.
- Open photon shutter and image the BM radiation that comes down the beamline
- Slowly move the undulator from maximum gap (~35 mm) down to a gap size of 10 mm. (Temperature calculations in section 2.5 and Appendix A were based on minimum or closed gap, ~ 7 mm, including a safety margin due to less than ideal cooling conditions around perimeter of YAG crystal, figure 3.6).
- Slowly open the undulator till maximum gap achieved
- Press "STOP" if time limit not exceeded.